Breaking wave impacts on the front deck of a ship

An experimental and numerical study about green water on ships in focused breaking waves

F. L. Beöthy

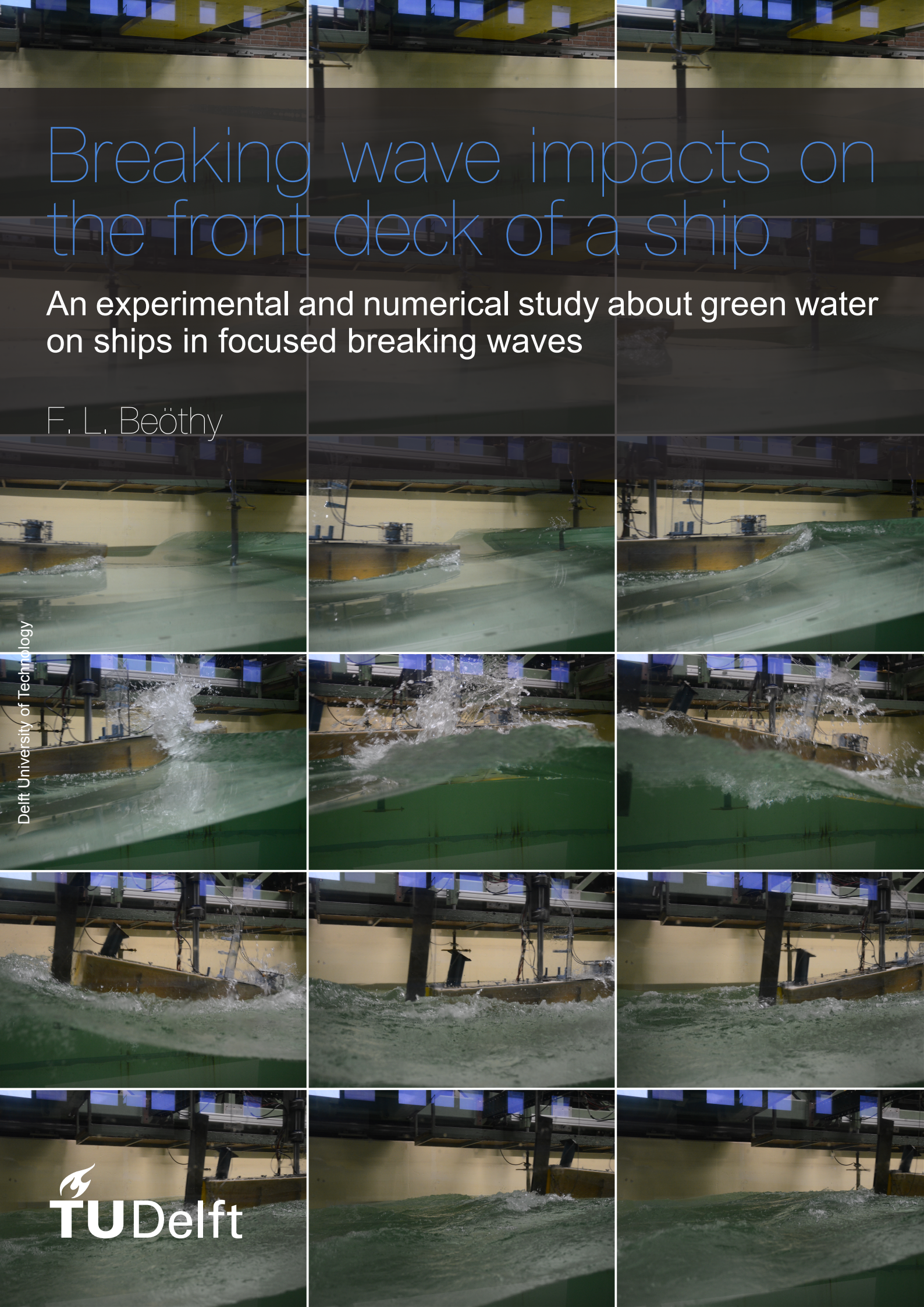

Delft University of Technology

TU Delft

Breaking wave impacts on the front deck of a ship

An experimental and numerical study about green water on ships in focused breaking waves

by

F. L. Beöthy

to obtain the degree of Master of Science in Marine Technology in the specialization of Ship Hydromechanics at the Delft University of Technology, to be defended publicly on Tuesday December 21th, 2021 at 15:00.

Student number:	5130441
Thesis number:	MT.21/22.013.M
Project duration:	March, 2021 — December, 2021
Supervisor:	Dr.ir. P.R. Wellens

Thesis committee:	Dr.Ir. P.R. Wellens	Chair, TU Delft
	Ir. A.D. Boon	TU Delft
	Dr.ir. G.H. Keetels	TU Delft
	Dr.ing. M. Brühl	TU Delft

An electronic version of this thesis is available at https://repository.tudelft.nl/.
Cover Image: Snapshot series of a model experiment of a ship sailing through a breaking wave.

TU Delft

Preface

In my thesis, I focus on determining the loads on a ship and its superstructure caused by extreme and rare wave events. The present thesis is part of my Master's program in Marine Technology which I have completed at the Delft University of Technology. I performed the research under the supervision of Dr. Ir. P. R. Wellens.

When I was looking for my thesis topic, I considered many options. I contemplated doing geometry optimization of none reflecting walls, modeling a propeller in the wake of a ship, and discovering the emerging field of PINNs. A common factor in these topics is fluid hydromechanics, one of my specializations next to ship design during my masters. I know I wanted to work with fluid flows, and I finally settled on the topic of green water. The topic is current and applicable in the industry to prevent structural failure and provide personnel and operational safety onboard a ship. By researching green water, I could explore fields I was interested in, numerical simulations of fluids and fluid-structure interaction. In retrospect, I would not choose otherwise. Besides exploring everything I expected, I got much more out of it. I conducted experiments, I was the project leader, and I could be part of a great team at the university for the past nine months.

First of all, I would like to thank my supervisor, Peter, for his help throughout my research process. I am glad you gave me a lot of space to explore and define my research in my way. Such freedom in a project was a challenging but rewarding new experience. I always enjoyed our meetings, which sometimes resulted in talks about other research, ideas, politics, etc. Thanks again, you have been a great supervisor!

I also want to thank Anna Boon, who helped me with the experiments and throughout my thesis process. She always offered her help with the thesis or dealing with the process itself.

I want to thank all the hard work, expertise, and technical support that the staff of the Ship Hydromechanics gave to me. Many thanks to J. G. den Ouden, who helped me design the experiments and did the majority of work in setting up my experiments. To P. Poot for helping during the experiments, P. T. Chabot and F. Sterk created vital equipment for the experiments, and J. R. Monteiro for being there, enlightening the mood and giving a hand wherever it was needed.

I thank my roommates, Bet, Cico, Geo, Patricia, Rosa, and Joel, for giving me support. They helped in hard times by going for a beer or a walk, talking with me to get my mind off the thesis, joking about my pronunciation of 'vave'. Thanks for being around, making me feel at home.

Finally, I thank my family in Hungary for showing interest in my work, supporting me during my time in the Netherlands. Enduring me when my head was spinning on the thesis even during my vacation at home. Thank you all for

Dear reader, I hope you will find at least as much pleasure in reading this thesis as I did throughout the past months preparing and writing it.

F. L. Beöthy
Delft, December 2021

Summary

Green water events on ships in extreme waves pose a considerable risk to personal, operational, and structural safety. Considering these issues, novel experiments were done to investigate the interaction between focused breaking waves and a ship at forward speed. The investigated interactions are global motion, global loads, and forces on a deck structure.

For the experiments focused, breaking waves were created, which served as loads of the green water events. First, wave focusing with prescribed characteristics was investigated in numerical settings. It was shown that focusing the waves with iterative methods does not lead to a converging solution. Three breaking waves were created in a wave basin. The characteristics of the waves were retrieved from 2D numerical simulations. The parameters of the spectrum of each wave were calculated from the simulation results.

The experiments were conducted systematically, where the position of the longitudinal center of gravity (LCG) of the ship was varied with respect to the focus point of the breaking wave at the focusing time. Using the same wave input resulted in green water events and loads on deck structure with different characteristics caused by different breaking stages of the focused wave. The effects of different ship velocities and different focused breaking waves were also explored throughout the experiments. It was shown that using the same focused wave, i.e., the same energy input, the breaking stage of the wave during the impact has a large influence on both the magnitude and time development of the loads on the deck structure. Force and pressure peaks were the largest and had an initial spike-like development when the wave during impact was in an unbroken stage. Impacts with the wave in its broken stage resulted in significantly lower loads and longer-duration load development. Such changes in the loads show that the ship's position with respect to the breaking wave is essential to consider even for the same input energy, posing additional challenges for establishing the maximum load in a sea state.

Table of contents

List of Figures

List of Tables

Nomenclature

Roman symbols

$\mathbf{F} = (F_x, F_y, F_z)$	External force vector in x, y, and z direction [N]
$\mathbf{u} = (u, v, w)$	Velocity vector in x, y, and z direction [m/s]
A	Total wave amplitude [m]
a	Regular wave amplitude [m]
a_{bow}	Vertical acceleration measured at bow of the ship [m/s^2]
A_{err}	Defocusing error of amplitude
a_{LCG}	Vertical acceleration measured at LCG of the ship [m/s^2]
c	Wave phase velocity [m/s]
c_g	Wave group velocity [m/s]
f	Wave frequency [Hz]
F_{box}	Axial force on superstructure of the ship [m]
f_{eig}	Resonance frequency [Hz]
F_{tot}	Total axial force on the ship [m]
Fr	Froude number [-]
G	Gain factor [-]
h	Water depth [m]
H_{m_0}	Significant wave height [m]
k	Wave number [1/m]
$k_y y$	Pitch radii of gyration [m]
L	Ship length [m]
N	Number of elements of simulation domain [-]
n	Number of wave components [-]
p	Pressure [Pa]
T	Wave period [s]
t	Time [s]
T_{err}	Defocusing error in time
t_{focus}	Focusing time [s]
T_{peak}	Peak period [s]
X_{err}	Defocusing error in space
x_{focus}	Focusing location [m]
B	Breadth moulded [m]
D	Depth moulded [m]

Greek symbols

Δx	Distance between ship's LCG and the focusing location of the breaking wave [m]
Δ	Vessel mass [kg]
λ	Wave length [m]
λ_{enc}	Encountered wave length [m]
μ	Dynamic viscosity [Ns/m^2]
∇	Three dimensional partial differential operator
∇_s	Vessel displacement [m^3]
ω	Angular wave frequency [rad/s]
∂	Partial differential operator
ϕ	Phase angle of wave [-]
ρ	Density of water [kg/m^3]
ξ_3	Heave motion of ship [m]
ξ_5	Pitch motion of ship [m]
ξ_{bow}	Vertical motion of bow [m]
ζ	Free surface elevation [m]
ζ_{frt}	Free surface elevation measured in front of the ship [m]
ζ_{LCG}	Free surface elevation measured at the LCG of the ship [m]
ζ_{rel}	Relative wave height [m]

Abbreviations

BEM	Boundary element method
BIV	Bubble Image Velocities
CFD	Computational Fluid Dynamics
CFL	CourantFriedrichsLewy
CV	Coefficient of Variation [-]
DB	Dam break
DSDS	Delft Systematic Deadrise Series
FPSO	Floating Production Storage and Offloading
FV	Finite Volume
FVM	Finite volume method
GABC	Generating Absorbing Boundary Condition
HF	Hammer fist
IRF	Impulse Response Function
KRISO	Korea Research Institute of Ships and Ocean Engineering
LCG	Longitudinal center of gravity [m]
NLS	Nonlinear Schrödinger equation
NS	Navier Stokes
PDB	Plunging dam break
PIV	Particle Image Velocities
PSD	Power spectral density
PW	Plunging wave
R^2	Coefficient of determination [-]
RANS	Reynolds Averaged Navier Stokes
RAO	Response Amplitude Operator
SPH	Smoothed Particle Hydrodynamic
VCG	Vertical center of gravity [m]
VOF	Volume of Fluid
WCMPS	Weakly compressible moving-particle semi-implicit
WW	White water

1

Introduction

In the past decades, more and more attention has been given in maritime and ocean engineering to non-common events such as breaking wave impacts, extreme wave formation, water on deck, and green water. Extreme events are rare but pose considerable risk to personnel, structural and operational safety. Extreme waves can formulate in calmer seas without warning, while steep, breaking wave impacts lead to high loads on a structure. Green water events caused by steep, extreme waves can result in structural and equipment damage. The ship's stability is affected by the high volume of water on deck after a wave impact. The impact of an extreme wave endangers the safety of crew and ship alike. From both personnel and structural point of view, it is essential to understand all the events that might have a potential threat to operational safety at sea.

Investigation of green water has increased since the end of the last century. Green water events are described by Kleefsman et al. [33] as a large volume of water flow on the deck of a ship in rough seas. Morris et al. [38] reported 17 green water incidents on three moored FPSOs over five years. Although green water phenomena might be scarce looking at the findings of Morris et al. [38] these incidents have harsh effects on the structure.

Significant effort in literature is put into determining the green water loads on FPSOs. However, not only FPSOs but ocean-going vessels can also suffer from green water events. The list of research is shorter when discussing green water events on ships at forward speed. At the same time, from operational, structural, and personal safety aspects, it is vital to address such scenarios.

Naval vessels, such as frigates, have to be ready to be deployed on short notice, transit to locations and operate worldwide. Weather conditions should not pose a barrier to reaching the destination. Therefore, naval vessels must be designed for more rough seas than commercial vessels. In general, weight reduction of vessels is an important factor, especially for military purposes where ship's speed is a significant factor in operations. These two requirements, to design for severe conditions and reduce weight, contradict each other. A more in-depth understanding of the possible loads is needed to resolve this contradiction. The insight can be used to design a safe structure for severe conditions while maintaining a lightweight design, for example, using composite structure or minimizing the used material. Analyzing green water loads on the front deck of a vessel will lead to a better prediction of the caused loads, which will lead to a better and lighter structural design for naval ships.

Studying green water events also improves the operations of existing vessels. Cargo carried by a container vessel should be delivered in a short time and good conditions to a destination port. Cargoes can suffer damage on the front deck of the ship from green water events. Moreover, minimizing the voyage time of container vessels is essential for logistics. In order to shorten delivery time, ships can risk crossing more severe sea states. The higher waves in severe sea states increase the chances of green water events, therefore posing additional risk to the safety of the cargo and crew alike. At the same time, search and rescue (SAR) operations should be conducted as soon as possible in time of need. The operational limits of a SAR vessel should be known in order to execute rescue procedures in a safe manner. Knowing the possible forces on the ship during a green water event helps decide on avoiding, making response time longer, or crossing a sea state, shortening the voyage time. Therefore, studying green water loads will improve the operations of existing ships and the design of newly built container, military, and SAR vessels.

For the analysis of green water events, most frequently, the maritime industry uses detailed model tests. Experiments can reproduce such strongly nonlinear events in model scale. However, more and more computational methods have been developed to model nonlinear events in the past decades. The numerical studies on green water are done next to experimental research. Significant progress has been made to address the wave impacts on fixed platforms, moored FPSO vessels, and a few even on ships with nonzero Froude numbers using experimental and numerical methods. More detailed and complex analyses are done to understand the event with the increased attention to green water events. Using detailed models can provide more in-depth knowledge of the phenomena. The consequences to personnel and structural safety and stability can be understood. Research on green water phenomena is helping to improve operational, structural, and personal safety.

1.1. Critical review of literature on green water and related research

Water on the deck is referred to in literature most commonly as green water, deck wetness, or water shipping. Green water events can occur during the interaction between a large wave and a floating structure. The types and phases of a green water event were investigated and described by previous literature. According to Greco et al. [23], based on experiments on a fixed 2D structure with a vertical side, there are five types of green water events:

- *Dam-break (DB):* The mass of water above the deck level flows along the deck and resembles the flow field after a dam-breaking
- *Plunging dam-break (PDB):* An initial plunging phase precedes the dam-break water
- *Plunging wave (PW):* A large scale, plunging jet-like impact on the deck
- *Hammer fist (HF):* A fluid arm reaches the deck, and the water block impacts the ship deck bluntly
- *White water (WW):* Initial flip through before impact, which develops into an upward-lifting jet

They concluded that the most common events are the DB and PDB type, while the PDB, PW, and HF have the largest potential to cause severe loads. Greco et al. [23] made these observations on a 2D fixed structure. In 3D experiments and numerical simulations on a container vessel Bandringa et al. [4] describe two distinct green water events which fit in the categorization of Greco et al. [23]. These are the *hammer fist* and *dam-break* type events. The dam-break type event is deconstructed into phases as

- The run-up of the water at the bow,
- The water shipping onto the deck,
- The subsequent green water developing along the deck,
- The impact with ship equipment or deckhouse [25].

Looking at these descriptions, it is evident that the green water event is a highly complex and nonlinear violent process. It starts with a violent wave impact which results in a jet-like flow on deck [9]. After the initial impact, a plunging wave can also form an air cavity which further complicates the analysis [25]. When the jet-like flow reaches the structures on deck, an impact occurs with high pressures and forces, and the flow is directed upwards by the structure. Usually, the most severe green water events happen in high and steep waves [23]. Due to their nature, steep waves can break. The flow of breaking waves and their impact on the structure will become aerated. The presence of the air phase will become important, which further complicates the analysis of such an event.

Green water events can occur during the interaction between a large wave and a floating structure. As discussed above, the process involves wave structure interaction, extreme waves, and violent flows on the deck. In the following chapters, an overview is presented of previous research on green water studies and related research topics which are important to address when discussing green water. Studies on waves that can lead to green water impacts include wave formation, and extreme breaking waves are presented. Papers describing green water loads are covered, structural loads caused by water on deck, and their relation with the motions of the floating structure are investigated. The overview includes both experimental and numerical studies in the covered topics.

1.1.1. Types of waves for green water impacts

As discussed before in section 1.1 and presented in the literature, structural loads increase with the steepness of the incoming waves [9, 23]. The wave can break when the wave steepness reaches the breaking limit, and the wave overturns. Waves are vital to discuss, as they are the cause of green water events. Knowing how waves can be formulated is the first step in analyzing green water events. Here an overview of the literature is presented, which focuses on steep, extreme waves and wave creation methods.

An early, widely publicized extreme wave record is shown in figure 1.1. The New Years' wave or Draupner wave was recorded in 1995 on the Draupner oil platform in the North Sea. It was documented, and can also be seen in the figure, that the Draupner wave is significantly higher and steeper than any other waves in the record. Vessels encountering such waves might be subject to severe green water events. Thus it is essential to understand how these waves are formed and how they can be modeled.

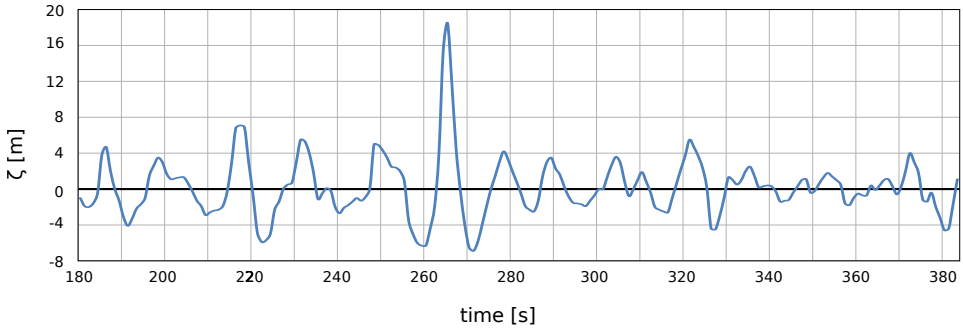

Figure 1.1: Draupner wave recorded in 1995. An example of an extreme wave that is significantly higher and steeper than other waves in the record. (Based on [15])

Extreme waves can formulate on the open sea in many ways. Dysthe et al. [19] describes three theories on how rogue waves can appear and can be reproduced. Extreme waves can formulate near shore, where the waves propagate towards shallow water. As the waves get refracted, their crests align with the bathymetry of the sea bottom surfaces and create steep waves where the wave energy can be focused on particular places. Dispersive focusing can occur within linear waves as well. Due to the dispersive nature of surface gravity waves, waves with different frequencies can focus and create a large wave in a particular place. Dispersive focusing, in theory, can happen in a linear Gaussian sea as well [19].

In figure 1.2 the applicability of different wave theories can be seen. It is evident from this figure that waves based on linear theory cannot represent waves that are near breaking. The highest impact happens when green water occurs after the ship encounters a steep wave; therefore, higher-order models are needed [23].

As the wave's steepness, λ H/λ, the ratio between the wave height H and wavelength, increases the wave overturns, resulting in a breaking wave. From figure 1.2 it can be seen that these waves are far beyond the validity region of linear waves. One of the main difficulties when analyzing breaking waves is the creation of the breaking wave itself. In irregular wave fields, breaking waves can be observed. Creating irregular waves relies on the probabilistic occurrence of a breaking wave. When a focused study is done on breaking waves, the waves should be generated deterministically, so they are reproducible.

Extreme, breaking waves are created with different methods in the literature. One research area of the formation of extreme waves is nonlinear focusing. A regular periodic wave train is unstable to modulation under certain circumstances and can develop into wave groups which, by further focusing, leads to extreme waves to the expanse of other waves [19]. Another method is to create an extreme wave through the superposition of several linear waves. Approaches such as the NewWave [50] or the Optimized wave [16] are based on linear wave theory. These methods are based on linear theory and cannot represent breaking waves because breaking waves are not in the validity region of linear theory (see figure 1.2). The methods based on linear theory can be used to estimate the height and breaking location.

The NewWave is a focused wave group that can create large amplitude waves with a short or almost no previous wave history. The formulation is based on wave spectra of a specific sea state. Using NewWave creates the most probable extreme crest height in a sea state. The original formulation uses linear waves [50]. However, the NewWave theory can be extended to second or higher-order Stokes waves to create a large steep

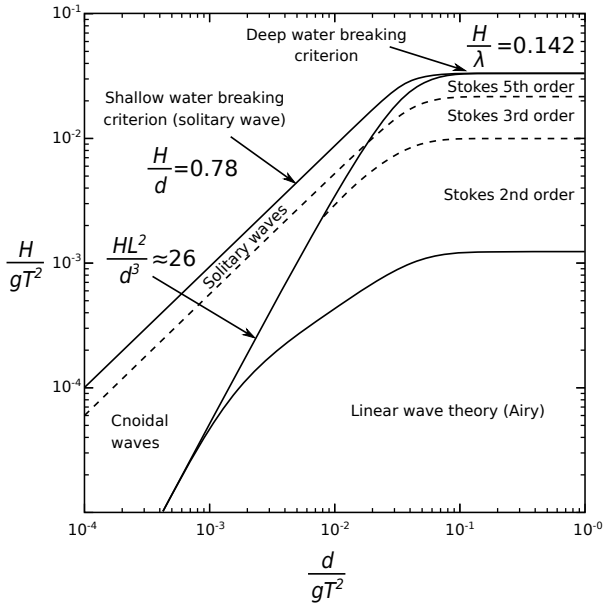

Figure 1.2: Region of applicability for different wave theories (based on [27]).

wave. According to the authors, the method is repeatable and requires minimal computational cost due to its deterministic nature. This method was used to investigate different types of breaking waves on offshore structures by changing the focusing location [28]. The comparison of experimental and numerical results based on NewWave wave formation shows good agreement in the study.

Another method to model extreme waves is to use so-called Optimized seas. This method also uses linear wave superposition. An extreme wave can be embedded in an irregular sea state using the optimized see. With the optimization, the wave's height, steepness, and position are prescribed. The wavefield keeps the spectra of the irregular sea state before and after the extreme wave [16]. It was shown that the method could not reproduce nonlinear wave propagation. However, it can be a boundary condition for a computational or physical domain where the complete nonlinear wave behavior is reproduced. The method was used alongside the NewWave theory for experimental investigation of a frigate in extreme wave events, including water shipping phenomena [6].

Finally, a nonlinear theoretical description of extreme waves is given by the solution to the nonlinear Schrödinger equation (NLS). The Peregrin-breather, a solution of the NLS, is described by Chabchoub et al. [11] and the theoretical results are compared with experiments. Within this method, a regular wave train is created with modulation, which leads to the development of an extreme wave in the wave train having three times the crest height compared to the regular waves before and after. Based on the report by DNV-GL [7] on rogue waves, this method is not able to create waves with high steepness. It is, therefore, not applicable for modeling near breaking and breaking waves.

There are several aspects to consider when determining the wave type as the load for green water analysis. Green water events happen most often with nonbreaking and not too steep waves. To determine the highest loads on deck due to wave impacts, steep, near breaking, or breaking waves are needed. In the case of a numerical investigation, these conditions require higher-order methods with the associated high fidelity codes and increased computational costs.

1.1.2. Dam-break like green water models

As discussed in chapter 1.1.1, green water loads can be caused by interaction with different kinds of waves. In the present chapter, impacts with nonbreaking waves are explored. Based on the categorization of Greco et al., presented in chapter 1.1, these are the dam-break (DB) and plunging dam-break (PDB) events. Literature is presented, which models the interaction between structure and nonbreaking waves.

Dam-break events are looked at to study the flow and loads on deck and deck structure. In the case of DB or PDB type green water, the flow and impact on a deck structure is very similar to a dam-break event [9].

Some studies describe scooping type green water events with dam-breaking and predict the loads using dam-break theories [9, 35]. Buchner [9] uses the theoretical dam-break event where he takes the initial relative wave elevation at the deck as $h(t=0) = (4/9)h'$, where h' is the dam-break height and derives the wave impact load based on this. In figure 1.3 the comparison of the flow on the deck of an FPSO and the theoretical instantaneous free surface of a dam-break flow is illustrated. The figure shows that the wave height over the deck at the bow changes with time instead of the dam-break flow, where the water height is constant at $x = 0m$.

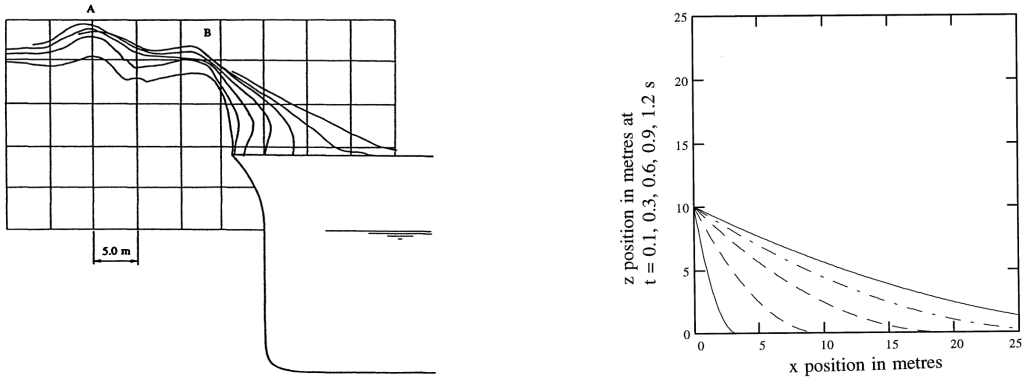

(a) Flow on the deck of an FPSO

(b) Theoretical evolution of dam-break flow

Figure 1.3: Comparison of the time development of the free surface contours between the flow on the deck of a green water event and the theoretical dam-break model (figures retrieved from [9]).

A more recent study Lee et al. [35] proposed a new method to account for the difference in fixed and changing water height at the deck. The authors suggest taking the instantaneous freeboard exceedance $h(t=\tau) = 4/9h'$ as the dam height instead of the initial wave elevation. Using $h(t=\tau) = 4/9h'$ will even better approximation for the flow velocities and impact loads on the structure than using $h(t=0) = (4/9)h'$. While both studies show similarity in the development of flow on deck to the dam-break flow, they fail to capture the forces resulting from the ship's motion response. The wave's initial kinematics, which impacts the deck, is also absent in these studies. The wave velocity distribution becomes important when a steep wave reaches the deck [9].

The dam-break estimation gives a good prediction on the velocity of the flow on deck for a DB (or PDB) event. The magnitude of the loads is proportional to the square of the velocity of the flow on deck [9]. Hence, the velocity prediction is vital to address the impact loads on the deck structure. However, the dam-break theory is only valid for a 2D case. 3D effects also play a role in flow and velocity development. As the water propagates from all sides inwards, a jet-like flow develops in the centerline of the bow, which then hits the structure [9].

The jet-like flow in the centerline of the deck just before the impact, which is created due to the 3D effects of the bow shape, can be described as a propagating triangular water wedge [9]. The loads on a wall, due to the similarity of the flow on deck to the water wedge, are studied analytically by Cumberbatch [18] based on similarity flow assumptions. They determined the pressure distribution on the wall after the impact. Buchner [9] discussed the similarity between the recorded green water flow on deck and their impact pressure to the analytical solutions of an impacting water wedge with 45 degree angle shown in [18]. They conclude that using such an approximation is only valid in the lower regions of the deck structure. Above the initial water height, the distribution of the pressures caused by the jet-like flow cannot be described with the water wedge impact.

The jet-like flow created due to the 3D effects of the bow makes the problem more complex, which the 2D dam-break model cannot capture well, nor can it be described with a water wedge impact. In order to assess, such impacts higher-order analysis is needed. Numerical simulations have been done which use a dam-break flow on a 3D bow section [32, 43]. These simulations use fixed waves around the bow. At the start of the simulation, the wave collapses as a dam-break-like flow would. With this method, the 3D effects of the flow on deck are captured well. The approach is an improvement from a 2D dam-break simulation, but the green water problem is still oversimplified. The kinematics of the wave and the vessel's motion are not included. Using a collapsing wave on a fixed structure cannot accurately predict the loads on deck in a more dynamic

situation like a ship with forward speed or extreme waves. Moreover, this approach is only applicable when looking at dam-break-like green water events. Still, this model fails to capture plunging waves (PW), hammer-fist (HF), and white water (WW) events.

The kinematics of the wave needs to be incorporated in the analysis to study the loads caused by plunging waves (PW), hammer-fist (HF), and white water (WW) events. Wet dam-break models incorporate the kinematics of the wave which hits the studied structure [2, 26, 48]. In a wet dam-break simulation, the bottom of the tank is filled with water as opposed to a dam-break event where the tank is initially dry. When the dam is released, it generates a wave that propagates towards the structure, causing a wave impact. Hernández-Fontes et al. [26] studied a 2D wet dam-break event experimentally where the structure was. They studied the loads on the vertical side, the horizontal deck of the box, and on a vertical wall built on the deck. They found that steeper waves result in a plunging type wave that formulates a cavity on deck, whereas less steep waves result in a dam-break-like flow on deck. A numerical study on wet dam-break was done by weakly compressible moving-particle semi-implicit (WCMPS) method [48]. The authors found that the Lagrangian particle-based numerical approach (WCMPS) can reproduce the experimental wet dam-break events and capture the flow's breaking features. Areu-Rangel et al. [2] validated a Smoothed Particle Hydrodynamic (SPH) code with the experimental results of Hernández-Fontes et al. [26] and investigated the effects of deck edge protection. Using the wet dam-break model, the control over the wave is very small. However, studying this phenomenon gives an understanding of the important physical flow developments when a wave reaches the ship. However, just as the dam-break simulation, it is a 2D study that simplifies a real green water event.

Dam-break-like green water models can approximate dam-break-like green water events. These models are good for assessing loads caused by the majority of the wave impacts on fixed structures or structures with little motion, such as moored FPSOs. Wet dam-break models can give a basic understanding of the flow by a steep or breaking wave. However, they cannot be used on a ship at forward speed, nor can they include the effects of the motions of a floating structure on the loads. The wet dam-break event also fails to give absolute control over the generated wave. In the following chapters, steep and breaking wave impacts and the effects of motions on green water will be addressed.

1.1.3. Extreme wave impacts

A green water event is caused by interaction between a wave and a ship. In chapter 1.1.1, different kinds of waves were explored, which could lead to green water events. In chapter 1.1.2, literature was presented, which deals with nonbreaking impacts through modeling green water events as a dam-break-like flow. However, interaction with extreme, breaking waves can also result in a green water event. The present chapter gives an overview of the literature on the impacts of steep and breaking waves.

Buchner [9] conducted experiments on a moored FPSO in irregular waves. They reported the impact pressures on the superstructure caused by a green water event as shown in figure 1.4. They recorded significantly higher impact pressures for the same freeboard exceedance. These incidents were associated with steep, breaking waves. The findings of Buchner [9] suggest that steep breaking waves cause more significant loads on a deck structure than nonbreaking waves, and shows the importance of dealing with such extreme wave impacts.

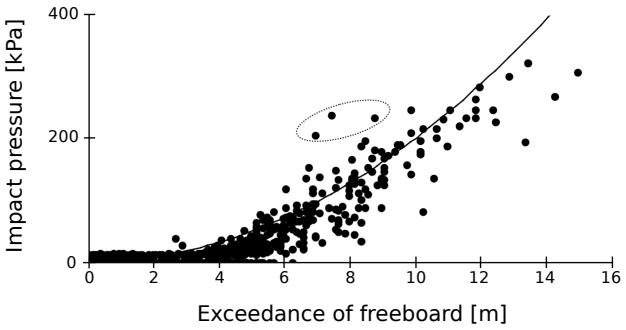

Figure 1.4: Impact pressure on superstructure against the freeboard exceedance. The results are shown in full scale based on [9]. The circled values are from steep or breaking waves.

The steepness of the incoming wave has a significant effect on the resulting green water event. The effects

of wave steepness have been investigated by experimental and numerical means. In experiments on a patrol vessel in regular waves Greco et al. [24] showed that the amount of water on deck increase with the steepness of the wave. They found that amount of shipped water is increasing with the increase of wave steepness. The effects of steepness on green water loads was investigated by Babu et al. [3] and Ravindra Babu et al. [46] numerically. They concluded that the pressure both on deck and superstructure increases with wave steepness, which is in agreement with previous findings [24, 36]. Bandringa et al. [4] presents two impact scenarios of a wave on a container vessel. The two experimental events were recreated numerically. The steepness of the incoming wave differed between the two events. It resulted in two green water events with different characteristics (hammer-fist and dambreak). The loads caused by waves with different steepness were dissimilar both in magnitude and in time. The agreement in the literature that increasing steepness leads to higher loads shows the importance of being able to recreate and study waves with high steepness.

Greco et al. [22] studied the impact of a wave on a fixed structure in 2D. They identified the different stages of a green water flow. The authors reported the plunging wave hitting the side of a square-like structure, which led to a generation of an entrapped air cavity on deck. The initial deck-wetting leads to high pressure on the deck. After the initial stage, the dam-break-like flow is developed, which impacts the structure. Greco et al. [22] also presented that 2D boundary element method (BEM) simulation can capture the same flow stages but not the whole green water event. In the continuation of the study [23] they categorized the wave impacts as shown in section 1.1. In the study, wave pockets were used to impact the fixed 2D structure. They showed that the most common impact is the dam-break (DB) type while the most severe are the hammer fist (HF) and the plunging dam-break (PDB) type events which occur less frequently. They concluded that the severity of the cases happens with increasing wavefront steepness. When the run-up on the side of the structure is slower than the velocity of the wave crest, a plunging wave (PW) or hammer fist (HF) type event will occur, which leads to the highest loads.

Bullock et al. [10], in their research on breaking wave impacts on a fixed vertical wall, identified four types of impact events. The four events were caused by different waves and are categorized as inclined, vertical front, plunging, and broken waves. According to their findings, all impacts of breaking waves are extremely variable. They concluded that more than one order of magnitude difference could be found between the highest and lowest peak pressure using nominally identical waves. They concluded that both high and low aerated waves could lead to equally high impact loads.

In a more recent study, Hu et al. [28] investigated the same four types of wave impact on offshore structures. The authors compared experimental and FV-CFD numerical results using OpenFOAM. They created extreme wave impact using NewWave formulation with second-order Stokes waves to recreate nonlinear, breaking wave impact. They could recreate the impact pressures numerically for all four types of wave impact with a maximum of 8% difference in the numerical results. The shape of the breaking wave is also captured accurately using OpenFOAM. They found that the air phase is important when air is entrapped as a bubble or when the wave is already broken, causing bubbly flow. Oscillations were recorded in the pressure characteristic of the hydroelastic response. The air compressibility effects were not simulated in the CFD setup. The authors conclude that the large entrapped air bubble distributes the high pressure over a larger surface, creating larger forces on the structure. Air inclusion can also lead to extended loading duration due to cushioning effects.

In a study by Ryu et al. [47], the run-up and green water velocities caused by breaking waves were analyzed. They used focused waves to create breaking waves in front of a fixed vertical structure and Particle- and Bubble Image Velocities (PIV, BIV) to capture the flow field. The study focused on recreating the velocity and vorticity fields and the turbulence in the flow. Based on dimensional analysis, they determined empirical equations for run-up velocity and the flow velocity on deck. The latter is important to predict the impact loads on deck structure as there is a quadratic relation between the flow velocity and the load [9].

In a numerical study of breaking wave impacts on a monopile, Alagan Chella et al. [1] varied the position of the breaking wave compared to the structure. With the change in position, they explored three breaking scenarios. The wave broke at monopile, before monopile, and far before monopile in the three different scenarios. The three cases resulted in three different breaking stages of the wave during impact. The authors found that the total wave force is changing significantly with the change of the breaking stage.

The motion response and forces of a pendulum with one degree of freedom were studied under breaking waves, changing the distance of the breaker compared to the pendulum by Bos and Wellens [8]. They created

a reduced-order model to predict the motion of the pendulum in breaking waves. The authors found that the pendulum's motion correlates with the surface elevation rather than with the wavefront speed and angle, which the reduced-order model confirmed. They also showed significant variance in both motion response and forces on the pendulum due to air entrainment. They found that there is variability in the global response (impulse) throughout the repeated experiments as opposed to breaking wave impacts on fixed structures such as presented by Bullock et al. [10].

As discussed before in chapter 1.1.1, focused waves are often used to study extreme waves. Using a focused wave gives control over a specific wave event during a sea state in the studied environment. Focused waves can be used as a means to model extreme wave events such as steep waves or breaking waves [5, 16, 19, 50]. Interaction between a fixed FPSO and focused waves were simulated by different numerical methods and compared by Ransley et al. [44] where the waves were non-breaking. Comparison of numerical methods simulating the interaction between a focused wave and a moored floating structure was made by Ransley et al. [45]. In these studies, the focused waves were nonbreaking waves. Bennett et al. [6] in their experiments sailed a frigate through focused waves, none of which were breaking.

Fundamental studies of breaking wave and structure interaction are important to understand the wave impact scenario. Wave impacts on an inclined bow section, like the bow of a frigate, rescue, or container vessel, the impacts will be different due to 3D effects and the inclination of the structure.

Looking at the literature, it is evident that violent flows pose considerable loads on structures. Breaking wave impacts are highly variable but lead to severe impacts. It was shown that the breaking stage of the wave during impact influences the magnitude and the load development on the structure. In previous chapters, the wave types the literature on wave impacts were discussed. However, floating structures have a motion response to the waves, which also influences the loads. In the following chapters, the connection between green water loads and motions will be discovered.

1.1.4. Vessel motion and green water

Green water loads occur during the interaction between a floating structure and waves. In previous chapters, modeling of impacts and their loads was discussed. The present chapter will discuss the relationship between the motions of a floating structure and the incoming waves.

The relation between motion and green water is investigated by Buchner [9]. The authors stated that the water height on deck correlates with the ship's motion. The initial water height on the deck is defined as

$$\zeta_{rel} = \zeta - \xi_{bow} \tag{1.1}$$

where ζ is the wave elevation and ξ_{bow} is the vessel's vertical motion at the deck. ξ_{bow} is influenced by all motions of the vessel but mainly by the heave and pitch motion. With increasing water height on deck ζ_{rel}, height in the dam-break-like event will be large as well. High initial water height on deck results in generous water volume with rapid velocities on deck, resulting in high loads on the structure. The connection between the ship's motions and water volume on deck shows the importance of considering the motion response of the ship when looking at green water events. However, the relation is not only one way. The amount of shipped water also influences the motion response of the ship as it introduces additional forces and moments in the ship's motion equation [9].

Zhao et al. [52] performed 2D experiments on the effects of heave and pitch motion of a box-shaped floating structure on green water loads. They concluded that the peak pressure and the motion magnitudes reduce with the increase of degrees of freedom as the motions absorb energy. It must be noted that the wavelength associated with the peak frequency was approximately four times larger than the length of the structure ($\lambda \approx 4 \cdot L$). However, their experiment still confirms that the influence of water on deck is not negligible on the motions of a floater.

The ship's motion, therefore the relative motion and the amount of shipped water, depends on the encountered waves. In a parameter study done by Greco et al. [24] with regular waves, the wavelength to ship length ratio λ/L was analyzed among other parameters. They concluded that the highest amount of water on the deck is found when the ratio is close to one, $\lambda/L \approx 1$. The largest amount of water on the deck is the most dangerous situation of water shipping. They concluded that it is less probable for water shipping to occur with longer waves. In long waves, the ship follows the waves more and more, and the relative motion will be small. In its experimental and numerical study Babu et al. [3] recorded highest pressure on deck at $\lambda/L = 1.2$

whereas the pressure reached its maximum on the superstructure at $\lambda/L = 1$. These results correspond to previous findings [9, 24, 38]. They suggest that, as the pitch Response Amplitude Operator (RAO) has a peak at the corresponding frequency, the relative motion is the largest at this wavelength, resulting in high pressures. These findings suggest that green water events are dangerous when there is a resonance between the ship motion and the waves.

Bennett et al. [6] in their experiments sailed a frigate through focused waves, none of which were breaking. They documented a so-called tunneling effect where the ship sailed through the extreme wave without significant motion response. The authors observed that with higher ship velocity, the volume of water on the deck is increasing. They concluded that the motion history of the vessel affects the response to the abnormal wave, which in turn affects the loads on deck due to vertical accelerations.

During a green water event, the shipped volume of water introduces additional forces and moments on the floating structure. The additional loads affect the motions of the structure. In experiments on a stationary FPSO, Buchner [9] determined that the green water loads have a large influence on the pitch motion response of the vessel. In a dedicated research Ravindra Babu et al. [46] validated a CFD code to study the effects of green water loads on the motions of a floating body. They found that the influence of motions due to green water is significant.

In literature, different approaches are seen to study the effects of motions in green water. Some numerical research on green water events are done by coupled methods that calculate the motion response with lower order codes, such as panel or strip methods. The green water event around the bow is captured by high fidelity CFD code. Most of these researches use one-way coupling. However, this neglects the green water load influence on the ship motion [42]. Some studies include the green water loads based solely on the freeboard exceedance, which is calculated in the low fidelity model [3]. The majority of these studies use linear theories for the motion of the ship. In a green water event, the validity of these assumptions is questionable [9].

Furthermore, not only the motion response of the ship is important to consider, but the effects of the ship's speed also need to be understood. Studies were investigating the effects of ship speed on green water loads [3, 24, 37]. In an experimental study of a tumblehome ship in regular waves, the increase in ship speed led to an increased green water occurrence [37]. Greco et al. [24] experimented on a patrol ship at zero and nonzero Froude number. They found that the amount of shipped water is larger and develops faster on the forward speed case, which leads to more severe superstructure loads. Similar conclusions were drawn from an experimental and numerical study by Babu et al. [3]. They investigated a KRISO container ship with four forward speeds and found that the loads first increase moderately from $Fr = 0.05$ to 0.13 but rapidly from 0.13 to 0.16. The literature agrees that increasing ship speed leads to higher loads.

Findings in the literature suggest that the effects of motions on the green water loads are important to consider. The motion of the ship can increase water volume on the deck, which leads to higher loads. The change in the ship's speed also influences the loads. Therefore, the ship's motion and speed are important factors to consider while analyzing green water events.

1.1.5. Green water events with forward speed

Flow on deck and loads on moored FPSOs were extensively studied numerically and experimentally with regular as well as irregular waves [9, 21, 32, 33, 35, 36, 41]. Less research is done on green water events on vessels with nonzero speed. Experiments with nonzero Froude number are usually more focused on seakeeping, motion response, and global bending moments, including green water effects [36, 37]. Only a few focus on green water loads as well.

A collection of numerical and experimental studies on vessels at forward speed can be seen in table 1.1.

Pham and Varyani [43] analyzed the green water event on the front deck using a dam-break model with a fixed deck structure. They prescribed a forward velocity to the water simulating the speed of the vessel. Due to the lack of structural movement, particularly vertical accelerations, the pressures on the deck could not be represented well. The kinematics of the wave is also lacking in this simulation. Kim and Lee [31] modeled a container ship in steep waves using CFD. However, the focus was on the global bending moment, not on the green water loads. Greco et al. [24] analyzed a container vessel in regular waves, focusing on seakeeping and slamming. They addressed the green water phenomenon and concluded that ship speed and wavelength greatly influence green water loads. Bennett et al. [6] did experiments on a frigate with nonzero speed fo-

Table 1.1: Some numerical and experimental works on ships with forward speed

Reference	Vessel	Fr	Analysis type	DoF	Struct.	Wave type
Pham and Varyani [43]	Container	0.30	CFD	Fixed	Yes	dam-break with forward speed
Kim and Lee [31]	Patrol	0.37	CFD	Free	Yes	5th order Stokes
Greco et al. [24]	Container	0.0 & 0.19	Exp./CFD	Free	Yes	Regular steep waves
Bennett et al. [6]	Frigate	0.0 & 0.28	Exp./ Strip/BEM	Free	Yes	Extreme waves
Li et al. [37]	Tumblehome	0-0.37	Exp.	Free	Yes	Regular waves
Bandringa et al. [4]	Container	nk.	CFD	Free	Yes	Specific events
Chen et al. [13]	Wigly hull	0.20	CFD	Free	No	Regular waves
Babu et al. [3]	Container	0.05-0.13	Exp./ IRF-CFD	Free	Yes	Regular steep waves

cusing on motion response in abnormal waves. They used regular and two kinds of abnormal sea states to analyze the motion response. They concluded that the motion history of the vessel is important in response to the abnormal wave, which in turn affects the loads on deck due to vertical accelerations. Bandringa et al. [4] recreated two green water events from an experiment for a KRISO container ship with forwarding speed. They found that the numerical tool they used (ComFLOW) is adequate to match the experiments. However, in the simulation, the six-degree motion of the vessel was imposed from the measurement in the basin. The waves from the experiments were recreated using deterministic methods. Chen et al. [13] used OpenFoam to simulate the full motion of a Wigley hull in regular waves. The results captured the green water effects well. In the research, there was no superstructure on the deck. Babu et al. [3] investigated the influence of wave steepness, ship speed, and wavelength on green water events of a KRISO container vessel. They used experimental results and compared them with a fully coupled impulse response function-computational fluid dynamic (IRF-CFD) based numerical calculations. Results indicated that the IRF-CFD method is robust enough to predict water loads' shipping on deck and deck structures efficiently.

This list of previous research discussed above shows that the interaction between green water and ship motions can be captured with high-fidelity CFD. Using numerical simulation has the potential for studying such a highly nonlinear and violent event.

1.2. Gap study

In chapter 1.1, the characteristics of green water events were described through previous research done in corresponding and related fields of studies. Looking at the findings, the most important factors on which the green water phenomena are dependent can be highlighted. These are the wave loads, i.e., sea state, wave steepness, the stage of the breaking wave, motion response, and the forward speed of the vessel. These are the most vital parts of the studied environmental and operational setting which can influence the green water event on a given ship geometry.

Looking at the highlighted factors which influence the green water characteristics and the previous research done on water shipping, it can be seen that only a handful of these incorporates breaking waves while breaking waves cause significant loads on deck [9].

A research gap is identified from the above overview of the literature on green water impacts and breaking wave interaction with structures. Table 1.2 highlights previous research done on focused and breaking wave interaction with structures. The fundamental study of Greco et al. [22] presented loads on a fixed structure caused by waves, including breaking waves. In their study, they used a fixed 2D structure without forward speed. Bos and Wellens [8] reported on the effects of systematically changing the focusing location of the breaking wave with respect to the position of the pendulum. In their experiments, no forces were recorded. The pendulum they used in their research has small inertia, not comparable with a ship. In their research, Bennett et al. [6] sailed a frigate through focused waves. The focused waves were not breaking, nor did they

record forces on the structure. There was no research done on focused, breaking wave interaction with a ship at forward speed. Nor were the effects of the breaking wave studied systematically on the global loads and forces on the superstructure.

Table 1.2: List of previous research on focused and/or breaking wave and structure interaction.

Research	Wave type	Structure	DoF	Loads	Speed
Greco et al. [22]	Regular, including breaking	Box	0 - fixed	✓	✗
Bos and Wellens [8]	Focused, breaking	Pendulum	1 - rotational	✗	✗
Bennett et al. [6]	Focused, non breaking	Ship	2 - pitch, heave	✗	✓
Present	Focused, breaking	Ship	2 - pitch, heave	✓	✓

1.3. Research goal

For operational, structural, and personal safety, the maximum loads caused by a green water event on a ship at forward speed are important to know, as discussed in chapter 1. However, based on the discovered gap in the literature in chapter 1.2, no systematic study investigates breaking wave impacts on a ship's front deck. The behavior of breaking wave impact on a ship at forward speed is expected to differ from the breaking waves studied on vertical walls and FPSO like structures. Investigating the effects of the breaking wave regarding the ship position at the time of breaking is a step toward determining the maximum possible loads on the deck of a ship at forward speed in a specific sea state. The stage of the wave breaking and the ship motions during impact are expected to influence both the development and magnitude of the load as well as the spread of the flow. Therefore the goal of the study is to

> *systematically study the effects of a focused breaking waves on the load over the front deck and superstructure of a ship with forward speed*

through answering the questions of

1. *How can the fully nonlinear problem be modeled in experimental and numerical settings?*
2. *How do the loads on the ship react to*
   (a) *changing the distance of the ship with respect to the breaking wave,*
   (b) *varying the speed of the vessel, and*
   (c) *using different waves.*

Other important aspects of the green water event are identified from the overview of the literature on green water and related fields. During green water impact, the ship's motion has to be considered. Due to the interaction between the wave and the ship, the motion influences the green water loads. As the green water loads of a breaking wave are investigated, the significance of the air phase is important to analyse during the impacts. Impacts of breaking waves was found to be highly variable in literature. The variability of the impacts should also be considered in the study.

To fulfill the goal of the study first, the load conditions are investigated by creating focused and breaking waves in numerical and experimental settings to investigate the research questions. Experiments are conducted where a ship is sailing through breaking waves under different conditions. The distance between the focusing location and the ship's position varies, the ship's speed is changed, and different focused breaking waves are investigated. Then, a numerical investigation is done to evaluate the capability of CFD code to capture such an event and confirm the experiments' results.

The investigation focuses on ships that are different from the extensively studied FPSOs due to their hull shape, especially at the bow and stern. Significant variations in parameters such as waterplane area and wetted surface with the change in free surface elevation will lead to nonlinear effects. The nonlinear effects are expected to be significant in the motion response. The breaking wave and its impact are both also a nonlinear process. Therefore the complexity of the problem is even more pronounced than in the case of moored FPSOs. Experiments are conducted, and high fidelity CFD code is used to evaluate the scenario.

1.4. Outline

In chapter 2, focused wave creation methods are investigated to create a focused wave with desired parameters, such as the time of focusing and its location at focusing. The experimental setup is presented in chapter 3, with the description of the ship model, used facility, and the measurement setup is described in detail. The conducted experiments and preparations are discussed for the experiments. Chapter 4 discusses the results of the conducted experiments. In chapter 5, the conclusions are drawn, and in chapter 6, recommendations are given for further research.

2

Focused, breaking wave creation methods for green water impacts

As it was discussed in the literature gap study in chapter 1.2, the aim of the present research is to *systematically study the effects of a focused breaking waves on the load over the front deck and superstructure of a ship with forward speed.* To investigate breaking waves causing green water on the front deck, first breaking waves must be created. The characteristic of the created breaking wave needs to be understood in order to create interaction between the wave and the ship. Breaking waves are nonlinear waves, and therefore creating and analyzing them is not straightforward. In the present chapter, part of the first research question *"How can the fully nonlinear problem be modeled in a numerical and experimental setting?"* is aimed to be answered as the first step in reaching the goal of the study.

The characteristics of the wave should be known in advance to study the interaction between a ship and a focused, breaking wave. The location of the wave at the breaking time of the wave must be known. Moreover, the parameters of the sea state, significant wave height H_{m_0}, and peak period T_{peak}, represented by the focused wave, should also be known to model a realistic scenario. In the present study, two methods were explored to know the characteristics of the wave. The first method aims to create focused waves with prescribed characteristics. Prescribing the characteristics gives control over the whole wave event as well as the global characteristics of the sea state. The first method is described in section 2.2. The second method is to create breaking waves and retrieve their characteristics in retrospect. This method only gives control over the global characteristics, and the properties of the focused wave have to be retrieved posteriorly. The second method is presented in section 2.3. In both methods, the waves are created using focused waves. An overview of wave focusing is described in section 2.1

2.1. Wave focusing

Focused waves are used in literature to create a large wave event [5, 6, 8, 12, 28, 50]. Focused waves are the superposition of several linear wave components. The waves are designed to focus at a prescribed location x_{focus} and time t_{focus}. All waves have zero phases at the prescribed location and time, creating the largest wave possible with the used components. Focused waves are created using linear (Airy) wave theory. The phases of the wave components to be focused are calculated based on their wave number and frequency as

$$\phi_n = -\omega_n \cdot t_{focus} + k_n \cdot x_{focus} \tag{2.1}$$

where ω_n is the angular frequency, k_n is the wavenumber of the wave component. The wavenumber is calculated with the first-order dispersion relation:

$$\omega^2 = g \cdot k \cdot \tanh(k \cdot h) \tag{2.2}$$

with h being the mean water depth and g the gravity constant. The instantaneous wave elevation $\zeta(t,x)$ can be calculated at any given time and position. $\zeta(t,x)$ is calculated superimposing all wave components, resulting in a wave that has its maximum surface elevation at the prescribed focusing time and location:

$$\zeta(t,x) = \sum_{n=1}^{N} a_n \cdot cos(\omega_n \cdot t - k_n \cdot x + \phi_n) \tag{2.3}$$

where a_n is the amplitude, ω_n is the angular frequency, k_n is the wave number, ϕ_n is the phase of component n with the satisfaction of the relations in equation 2.1 and 2.2.

In literature, many variations of linear focusing are used. Fernández et al. [20] created a self-correcting method to focus waves in numerical settings using potential code. They used first and second-order target functions, which was the desired wave elevation they wanted to reach with the focused waves. Applying Fourier transformation of the signal at the focusing location, they corrected the phases of the different linear wave components through iterations. Iteration was done until the desired correlation with a target wave signal was reached at the focal point. After five iterations, they accomplished a good correlation already using 32 wave components.

Clauss et al. [17] used a Subplex optimization method to change the phases of certain wave components which had the most energy at the time of focusing at the focusing location. They used wavelet transform to determine the wave components with the most energy. The goal of the optimization process was to reach four predefined wave characteristics such as steepness, wave height, location, and time of the focused wave. For this, they needed more than 600 iterations. In an experimental study a slightly different approach was used by Clauss and Klein [14]. Their target function was a scaled real-time signal, the New Years Wave. The wave record was measured at the Drauppner platform in 1995 in the North Sea (see Fig. 1.1), which they also reproduced with optimization.

A more recent experimental study Bos and Wellens [8] created focused waves by using ten wave components, releasing the components as wave groups after each other. The groups of waves were created applying a window function on the wave component. Each component's wavelength and window were tailored, so each wave component is released as a group of waves after the other minimizing the interaction between the components. They used linear theory to calculate the wave phases and the timing of the windows to create the wave groups.

These methods have different advantages and disadvantages. The first two create an irregular wave field with an embedded extreme wave event [17, 20]. With having an irregular wave field around the focused wave leading waves, that is, waves before the focusing event are present. The last example creates only one extreme wave without significant leading waves [8]. On the other hand, using wave groups allows the usage of linear theory, and the focused wave location can be predicted without iterations.

In the following chapters, two methods will be explored as discussed in chapter 2. The above described focusing techniques inspire the used methodologies.

2.2. Wave creation by prescribed characteristics

As described in the preamble of chapter 2, the characteristics of a breaking wave should be known in advance in order to use it for interaction between the ship and the wave. Two methods were explored to know the characteristics of the wave. The first method is presented in this chapter, where the characteristics are prescribed, and waves are created to match them. The goal of the first method is to create focused waves where the wave focuses at the prescribed location at the prescribed time using the superposition of linear wave components. Using prescribed characteristics gives more control over the focused wave itself and the general sea state that it represents.

The investigation is done in 2D in a numerical domain. The CFD solver ComFLOW is used, which is described in appendix A. First, the numerical settings are described, then the nonlinear wave propagation problem is presented. The nonlinear wave propagation introduces defocusing errors. The largest wave is not at the prescribed location at the prescribed time. Corrections based on third-order wave theory and iterative methods are explored to account for nonlinear wave propagation. The correction aims to create the largest focused wave at the desired point in space and time.

2.2.1. Numerical setup

The numerical setup of the simulation has three important aspects. The extents of the domain, the applied boundary conditions, and the discretization. The domain size and discretization changes from case to case, however in all cases, they comply with some basic requirements, which are described below:

- Focusing location is at least two wavelengths from the inlet BC looking at the shortest wave component to give time and space for the development of the nonlinear waves,
- the reflection of the fastest wave should arrive one wave period later to the focusing location at the time of focusing, so the reflected waves do not interfere with the results, and
- the horizontal resolution should be chosen, so one wavelength is resolved in at least 60 cells, and a wave height is resolved in at least six cells [40].

There are criteria on the time of the simulation which are dependent on the simulated wave components:

- The focusing time is at least one wave period after the arrival of the slowest wave component to the focusing location, so all the waves are arriving developed to the focusing location, and
- All transient disturbance from the startup has to pass the focusing location by the focusing time, so the transient effects do not hinder the focused waves.

Care is taken to fulfill these requirements in setting up the simulations. The setup of the domain with coordinate notations is shown in figure 2.1

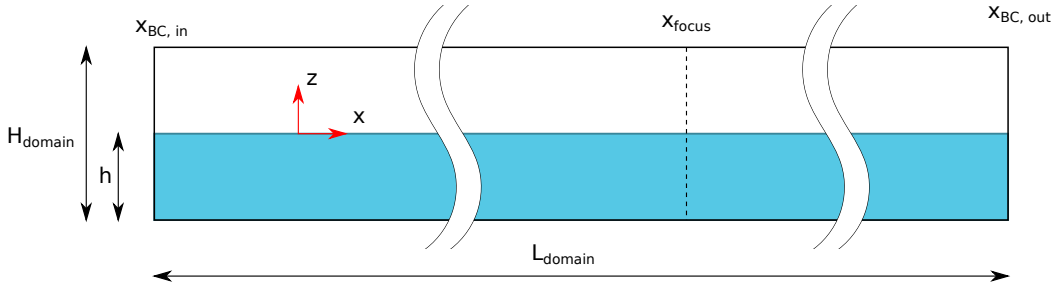

Figure 2.1: The illustration of the simulation domain with it coordinate system and important dimensions - Numerical Wave Tank

Boundary condition

At the inflow boundary $X_{BC,\,in}$ waves are released to the domain based on a velocity profile along the boundary. Waves are created using linear superposition of several wave components described by their amplitude, angular frequency, and phase. The velocity-, pressure field, and free surface elevation are calculated at the inflow boundary condition. Above calm water surface, linear extrapolation is applied to define the velocity profile of the waves [40].

At the outflow boundary $X_{BC,\,out}$ the Generating Absorbing Boundary Condition (GABC) is applied. The GABC is applied to reduce reflection at the end of the domain. The parameters of the GABC (a_0, a_1, b_1) originate from the approximation of the linear dispersion relation:

$$c_a = \sqrt{\frac{a_0 + a_1(kh)^2}{1 + b_1(kh)^2}} \tag{2.4}$$

The reflections can be minimized by tuning the parameters of the GABC to the set of wave components present in the domain (kh).

As GABC absorbs the waves, the reflection at the outflow boundary is minimized. Using GABC relaxes the requirements set for the domain extent, and there is no need to use long domains which account for the reflected waves.

2.2.2. Linear focusing error

The focusing theory, which was described in chapter 2.1 is valid for linear waves. However, breaking waves are outside of the limits of the Airy wave theory. Using linear theory to create nonlinear waves introduces errors in the focusing described below.

The wavelength of the components are chosen to be between $L_{min} = 3.0$ m and $L_{max} = 7.0$ m while the mean water depth is chosen to be $h = 1.0$ m. The characteristic of the waves are calculated using the dispersion relation and which is presented in table 2.1. The focused wave has an amplitude of $a_{focus} = 200$ mm with 32 components where the amplitude of the components are identical. The focusing time was chosen to be $t_{focus} = 11$ s.

Table 2.1: Range of wave components used to create focused waves.

	ω [rad/s]	T [s]	k [1/m]	λ [m]	c [m/s]	c_g [m/s]
long	2.51	2.50	0.90	7.00	2.80	2.26
short	4.46	1.41	2.09	3.00	2.13	1.20

Based on the wave velocities and the criteria listed in chapter 2.2.1 the needed domain is calculated. The parameters of the domain are shown in table 2.2.

Table 2.2: Details of simulation domain for linear focusing error. The notations are in line with the NWT representation in figure 2.1

Inflow boundary	$X_{BC,in}$	[m]	-6.00
Outflow boundary	$X_{BC,out}$	[m]	13.00
Domain length	L_{domain}	[m]	19.00
Domain height	H_{domain}	[m]	2.00
Water depth	h	[m]	1.0
Resolution x	Δx	[m]	0.02
Resolution z	Δz	[m]	0.02
Element number	N	[-]	95k

In figure 2.2 the results of a focused wave can be seen with the linear target function. As was expected, the linear focused wave is symmetric and is at the focusing location at the focusing time. However, the wave simulated in ComFLOW is faster and already left the focusing location at the focusing time. In other words, the nonlinear waves propagate faster than what linear theory suggests, and the focused wave reaches the focusing location earlier than desired. The resulting wave also has a higher amplitude than the focused wave. The need for a correction method is evident as the goal is to have the nonlinear focused wave simulated with CFD at the prescribed location at the prescribed time.

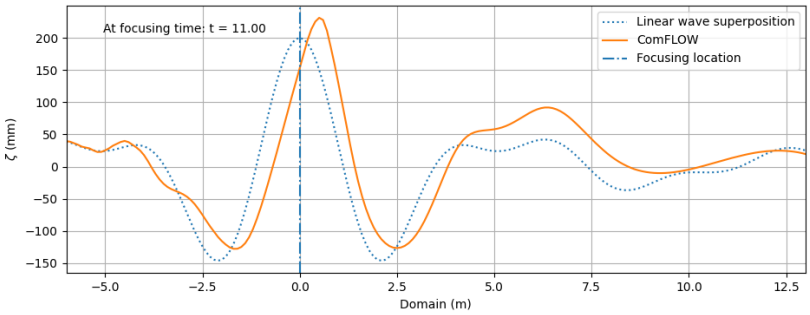

Figure 2.2: Difference between linearly predicted and simulated free surface elevation of a focused wave in the numerical domain at the time of theoretical focusing. The wave is outside the scope of linear wave theory and passes the focusing location at the time of theoretical focusing.

2.2.3. Third-order correction method

In order to correct for the faster nonlinear wave propagation the phases are calculated using 3rd order dispersion relation following the derivation presented by M.W. Dingemans [39]. The stokes expansion to nonlinear waves is based on a perturbation method around the free surface. The third-order dispersion relation therefore is

$$\omega^2 = g \cdot k \cdot \tanh(k \cdot h) \cdot \left(1 + \frac{9 - 10 \cdot \tanh(k \cdot h)^2 + 9 \cdot \tanh(k \cdot h)^4}{8 \cdot \tanh(k \cdot h)^4} \cdot k \cdot a\right) \tag{2.5}$$

The interaction of waves cannot be captured with this method. However, it compensates individual components for the nonlinearity due to high amplitudes. Each wave component is transferred to the inflow BC using the equation 2.1 where the third-order dispersion relation is satisfied. The propagation velocity of the waves, and therefore the calculated focusing time, is also based on the third-order dispersion relation. As the expansion depends on the amplitude of the wave components, few components were used with high amplitudes to test the method.

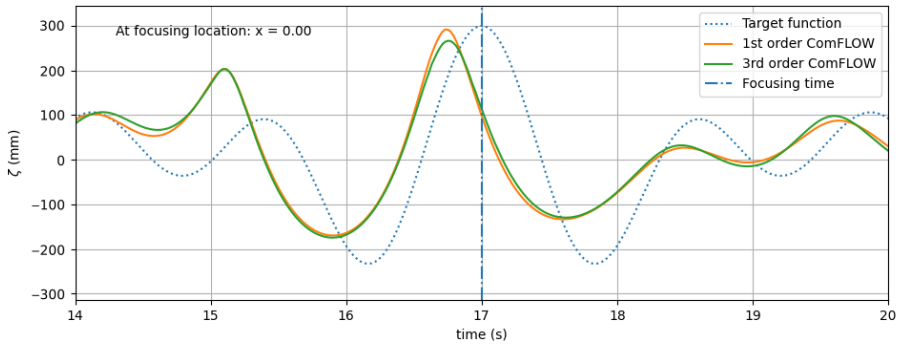

Figure 2.3: Comparison wave simulation results where the wave propagation is based on linear and third-order methods. The target function is the same in both cases, as shown in the figure. The compensation in defocusing is not compensated significantly by calculating the wave propagation based on third-order method.

In figure 2.3 the comparison between a simulation where the components were calculated based on linear theory and where the third-order dispersion relation was used. Three components were used each having an amplitude of $a = 100$ mm. As it can be seen using a higher-order method for the phase calculation, the defocusing error does not change significantly. There is a slight shift of the wave towards the desired focusing time. However, the wave still arrives at the focusing location earlier and focuses after it. Therefore, the goal to have the wave at the prescribed position at the prescribed time was not reached with third-order correction.

This simulation was done with three components with high amplitudes. Increasing the component number will lead to an even smaller correction as the amplitude of the components will decrease, leading to a lower correction. In conclusion, it is not feasible to create focused waves by using third-order expansion to calculate the individual component propagation and superimpose them. Therefore other methods should be explored.

2.2.4. Iterative correction methods using Fourier transform

It was previously discussed in chapter 2.2.2, superimposing prescribed linear waves to create a focused wave leads to the focused wave reaching the focal point prematurely in time. The error is due to the nonlinearity of the waves and the limitation of the Airy wave theory, which cannot be used for steep waves.

As mentioned before in chapter 2.1, there are already existing studies where the correction based on the spectral representation of the generated wave was implemented to create focused waves. Both experimental and numerical studies are done. In an experimental study, 256 wave components were generated by a flap-type wave maker by Clauss et al. [17]. They used wavelet transform to optimize only 90 of those components to create create a wave fulfilling specific criteria such as wave height and steepness. The components were based on JONSWAP spectra with different peek enhancement factors for different simulations. Over 600 iterations were needed using this method until the used Subplex optimization algorithm converged.

Fernández et al. [20] second-order target function. He simulated waves using potential flow in a 2D setting. The waves were generated with a flap-type wavemaker. He an iterative method to reach the target function based on the difference in the spectral domain of the target wave and the simulated wave. For the first iteration, a large step was achieved towards the goal. Six iterations were suitable for the method to converge to the desired degree. They used only 32 wave components where each component had a predefined amplitude such that all wave components had the same steepness, therefore satisfying the condition

$$a_n = \frac{G}{k_n} \tag{2.6}$$

where a_n and k_n are the amplitude and wavenumber of a component, and G is a gain factor (proportional to the wave steepness $G = a_n \cdot k_n \propto a_n/\lambda_n$), which was varied for different simulations.

The common practice in these methods is that the wave generation is done with a wave board. In the present study, the velocity profile of the superimposed wave components is calculated at the inflow boundary, which serves as a velocity inflow BC. For the wave creation, the wave components are prescribed, and the built-in wave generator library of ComFLOW [40] calculates the velocity profile at the inflow boundary. The method uses linear extrapolation to determine the kinematics of the flow above the free surface. The linear extrapolation is an approximation of the flow above free surface level. For large waves, the linear extrapolation overpredicts the velocity of the wave crest. Therefore it could lead to errors in the wave field.

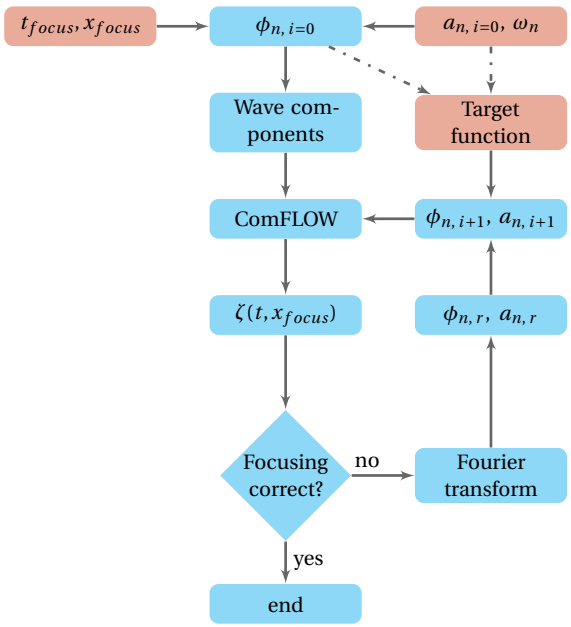

Figure 2.4: Flowchart of correction method which iteratively compensates the superposed wave components phases (and amplitudes) based on the free surface elevation at the focusing location in order to create focused wave at prescribed location x_{focus} and time t_{focus} in numerical domain.

Two methods based on Fourier transform were used and evaluated if suitable for creating focused waves. The methods are different in how the wave components are changed through the iterations. In all cases, the algorithm follows a similar structure shown in figure 2.4. The time history of the wave elevation at the focusing location is transformed into the spectral domain using Fourier transformation. The components in the spectral domain are compared with the spectral representation of the target function. Based on the difference, the components are corrected, and the simulation runs again until the defocusing becomes acceptable.

The defocusing is looked at in space and time, and the amplitude error is checked. The crest of the focused wave is compared with the prescribed focusing time and location as

$$T_{err} = \frac{t_{focus} - t_r}{T_{max}};\ X_{err} = \frac{x_{focus} - x_r}{L_{max}};\ A_{err} = \frac{A_t - A_r}{A_t} \tag{2.7}$$

where T_{max} is the maximum period and L_{max} is the maximum wave length of the used wave components (see: table 2.1), the subscript r refers to the recorded value in the simulation and t to the target value.

A small downstream distance was used from the inflow and the focal point, which is twice the length of the shortest wave component. It was observed that the convergence is slow, and the resulting wavefield is not acceptable. The leading waves became larger than the desired wave at the focusing location with a short downstream distance. Large waves will lead to premature breaking if the amplitudes of the waves are increased. Therefore, using the short domain focused, breaking wave cannot be created at the desired location and time. The wave which was focused started to converge towards the prescribed focusing time and location. However, after 45 iterations, there was still no convergence. There were larger waves before and after the desired focusing location, which cannot be accepted as a focused wave. Such overshoots can result from

the used linear extrapolation of the velocity profile at the inflow boundary, as it overpredicts the velocities of the flow. The overprediction of velocity could introduce extra water flux to the domain and create large waves near the inflow BC. The large wave is present due to numerical setup and does not represent a real physical process. Therefore the short domain is not acceptable.

The simulation domain was extended after establishing that a short downstream distance is not enough. The inflow BC location was set to $x_{BC} = -34$ m from the focusing position. The longer domain increased the computational time. However, several improvements were seen as compared with the short domain. The convergence of the waves happens faster. The focused wave was smaller before and after it reached its maximum in the proximity of the focusing location. The domain parameters can be seen in table 2.3

Table 2.3: Details of simulation domain for iterative correction methods. The notations are in line with the NWT representation in figure 2.1

Inflow boundary	$X_{BC,in}$	[m]	-34.0
Outflow boundary	$X_{BC,out}$	[m]	34.0
Domain length	L_{domain}	[m]	68.0
Domain height	H_{domain}	[m]	2.0
Water depth	h	[m]	1.0
Resolution x	Δx	[m]	0.02
Resolution z	Δz	[m]	0.02
Element number	N	[-]	343k

Two methods using Fourier transform were applied to create the focused wave: one where only the phase of the wave components was changed and one where the amplitudes are corrected as well. The amplitude correction was done with two approaches. In all simulations, the target function (the target wave) is based on the linear superposition of the wave components. The range of the used wave components is the same as used before in all cases, shown in table 2.1. The different simulations are shown in table 2.4

Table 2.4: Summary of different simulations done with three different correction methods and two initial wave amplitude distributions.

	Gain $G = 0.0013$	Spectra $T_p = 2.0$ s
Phase correction only	Nr. 1.1	Nr. 2.1
Phase and amplitude correction - A	Nr. 1.2	Nr. 2.2
Phase and amplitude correction - B	Nr. 1.3	Nr. 2.3

Two different initial spectra were defined for the waves. One used the method presented by Fernández et al. [20] (see eq.: 2.6), which keeps the steepness of the individual components constant. The other uses a JONSWAP spectral distribution for the amplitudes. To make the simulations comparable and to simulate them in the same domain in both cases, the sum of the amplitudes was normalized to $\sum a_n = 0.2$ m. The gain factor with this was $G = 0.0013$ and the JONSWAP spectrum had a peak period of $T_p = 2.0$ s. 79.62% of the total energy of the JONSWAP spectrum is realized in the used wave components that is presented in table 2.1.

The comparison of the results, using the two different initial spectral distributions, for the zeroth iteration can be seen in figure 2.5. As it can be seen using constant steepness for the waves (gain method), the leading waves are smaller when compared to the result using JONSWAP spectra. A smaller leading wave suggests that the gain method might be better in terms of avoiding premature breaking. However, the differences between the two initial amplitude distributions do not considerably affect the results based on which they are evaluated. All simulations were run for ten iterations regardless of the magnitude of the defocusing errors.

Correcting the phases of the wave components iteratively

The phases are corrected using the difference between the linear target function and the recorded surface elevation. The time series is recorded from the start of the simulation, and the Fourier Transform is done on the whole recorded series. In this case, there is no need to calculate phase shift due to time difference as the resulting phases of the components from the Fourier transformation will be given at the initial time, that is at $t = 0$ s.

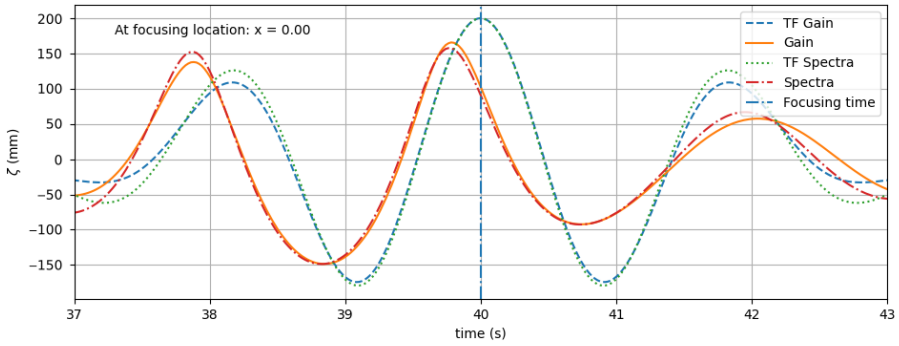

Figure 2.5: Comparison of the free surface elevation at the focusing location using initial gain and spectral amplitude distribution for wave components. The figure shows the target functions using the two initial amplitude distributions (TF Gain and TF Spectra) and the resulting wavefield (Gain and Spectra). The prescribed focusing time is also presented.

However, there is also a spatial shift to consider. The focusing location is chosen to be at $x_{focus} = 0$ m, therefore, the spatial shift is resolved by itself. As the spectral representation of the surface elevation time series is looked at at the focusing location, the spatial shift due to the location of the sampling is zero. The transformation to the inflow boundary is already done with the initialization of the phases in equation 2.1. Therefore, the phases for the next iteration step are calculated at any given iteration as follows:

$$\phi_{n,\,i+1} = \phi_{n,\,i} + (\phi_{n,\,t} - \phi_{n,\,r}) \tag{2.8}$$

where $\phi_{n,\,i}$ is the phase angle of component n for the current iteration, t refers to the phases of the target function, and r to the recorded phase of component n after the Fourier transformation.

The results of Nr. 2.1 for selected iterations are shown in figure 2.6 and the defocusing errors for the phase changing method for both initial amplitude distribution are presented in figure 2.7. It can be seen that correcting only for phases matched the focused wave location and time well with the prescribed values. Already after the first iteration, the defocusing error is significantly lower. The improvement is quite noticeable for the first iteration already using the amplitude distribution with uniform steepness (gain amplitude). On the other hand, for the JONSWAP spectra, the 7th iteration was the best with a temporal error of $T_{err} = 0.01$ and spatial error of $X_{err} = 0.00$. The best results for each method can be found in table 2.5. Using only phase

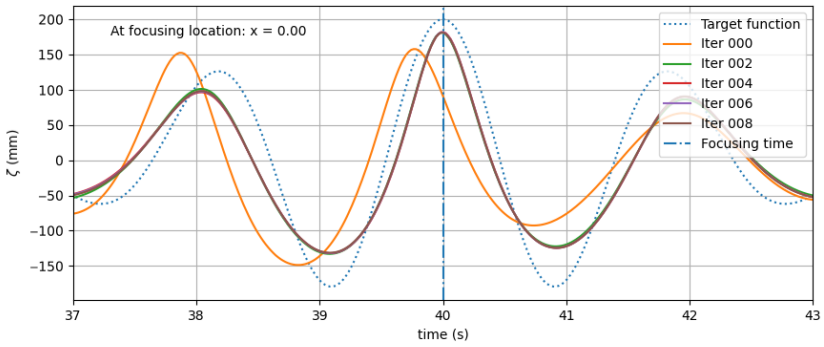

Figure 2.6: Iterations where only the phases are corrected during the iteration process. The initial distribution of the amplitude is based on spectral distribution (simulation Nr. 2.1). The prescribed focusing time is also presented.

correction leads to decreasing wave amplitude at the focusing location. As the signal is transformed to the spectral domain and the frequencies are truncated to match the original frequencies, some information loss is introduced. As a result, not all wave components align at the desired focusing location; therefore, the amplitude of the generated wave is smaller than the prescribed amplitude. The amplitude of the focused wave does not change significantly from the first iteration, and the error in both cases remains below 0.1 after the first iteration.

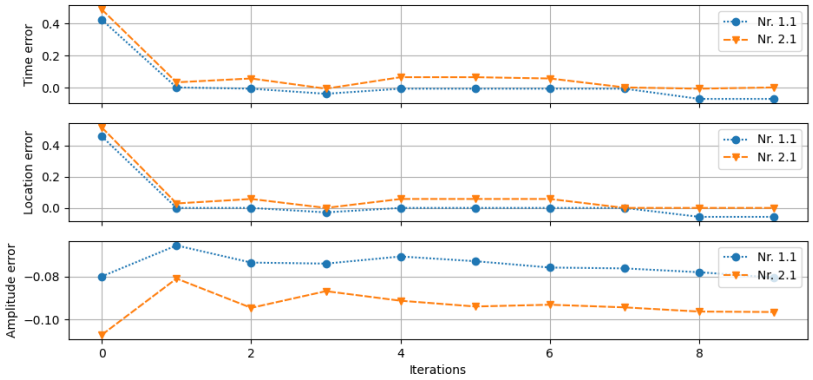

Figure 2.7: Change of defocusing error with iterations where only the phase of the wave components are changed. The errors are shown for an initial gain (Nr. 1.1) and spectral (Nr. 2.1) amplitude distribution.

Correcting the phases and the amplitudes of the wave components iteratively

After seeing that the amplitudes are smaller an amplitude correction method was introduced following the method of Fernández et al. [20]. The amplitude correction is designed to match the amplitudes of the target function after the propagation where the wave wave interaction changes the wave spectra. The amplitudes for the new iteration are calculated as

$$a_{n,\,i+1} = a_{n,\,i} \cdot \frac{a_{n,\,t}}{a_{n,\,r}} \tag{2.9}$$

where a_n is the amplitude of the nth wave component, subscript t stands for the target amplitude, subscript r for the recorded amplitude at the focusing location, and i represents the current iteration step.

Using equation 2.9, the resulting wave amplitude was getting higher and higher with each iteration step failing to converge to the target functions. After taking the Fourier transform of the new iteration, the amplitudes of the wave components were compared. The amplitudes of the wave components of the new iteration step were smaller than the initial amplitude of the individual wave components. The Fourier transform of the wavefield has energy outside the used wave component range. When using only the desired wave components, and the amplitudes are corrected based on equation 2.9, the energy outside the range is transferred to the used range. Having more energy leads to the new wave components having higher amplitudes for each iteration step, and the method fails to converge. Using the method of Fernández et al. [20] does not lead to a converging solution. The growth in amplitude had to be compensated to stabilize the convergence.

Two methods were tried to reach convergence for the amplitude error. One, where a limitation was introduced that is changing the amplitudes according to equation 2.9 but limiting the sum of the amplitudes to the desired focusing level. The used limiter is shown in equation 2.10.

$$a_{n,\,i+1} = a_{n,\,i} \cdot \frac{a_{n,\,t}}{a_{n,\,r}} \cdot \frac{A_t}{A_{new}} \tag{2.10}$$

where $A_{new} = \sum a_{n,\,i} \cdot \frac{a_{n,\,t}}{a_{n,\,r}}$ is the sum of the new amplitudes after changing them based on the Fourier transform and A_t is the desired target amplitude of the focused waves. The other notations are the same as in equation 2.9.

Second limiter was used, where the ratio of the simulated focused wave amplitude and the desired amplitude was used as a multiplication factor to change each components amplitude. The used factor is shown in equation 2.11

$$a_{n,\,i+1} = a_{n,\,i} \cdot \frac{a_{n,\,t}}{a_{n,\,r}} \cdot \frac{A_t}{A_r} \tag{2.11}$$

where A_r is the simulated amplitude of the focused wave. The other notations are the same as in equations 2.9 and 2.11.

The results of phase and amplitude correction using initial gain distribution (Nr. 1.3) for selected iterations are shown in figure 2.8. The defocusing errors for all phase and amplitude correction methods are presented

in figure 2.9. Some degree of convergence can be seen in the initial iteration steps. However, in most cases, oscillation can be observed. The magnitude of the oscillation does not decrease or decrease slowly. The first amplitude correction method based on equation 2.10 (Nr. 1.2 and Nr 2.2) did not improve the amplitude error compared to the method where only the phases were corrected (Nr. 1.1 and Nr. 2.1). The amplitude errors remained in the same range for both gain and spectral amplitude distribution compared to the simulations where only the phases were changed. A fluctuating convergence to a smaller amplitude error can be observed using the second amplitude correction method based on equation 2.11 (Nr. 1.3 and Nr 2.3). However, the spatial and temporal errors were higher than in other simulations. For the wave components with constant steepness the best amplitude error reached was $A_{err} = -0.0030$ however at this iteration the temporal and spatial error were $T_{err} = 0.1048$ and $X_{err} = 0.1143$. The best results for each settings are shown in table 2.5.

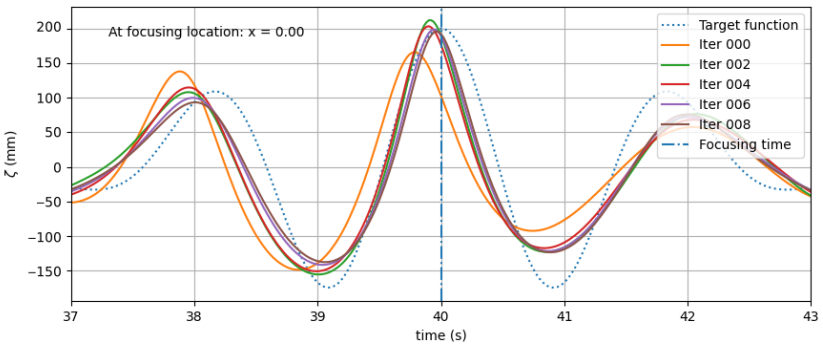

Figure 2.8: Iterations where the phases and the amplitudes are corrected during the iteration process. The initial distribution of the amplitude is based on spectral distribution (simulation Nr. 1.3). The prescribed focusing time is also presented.

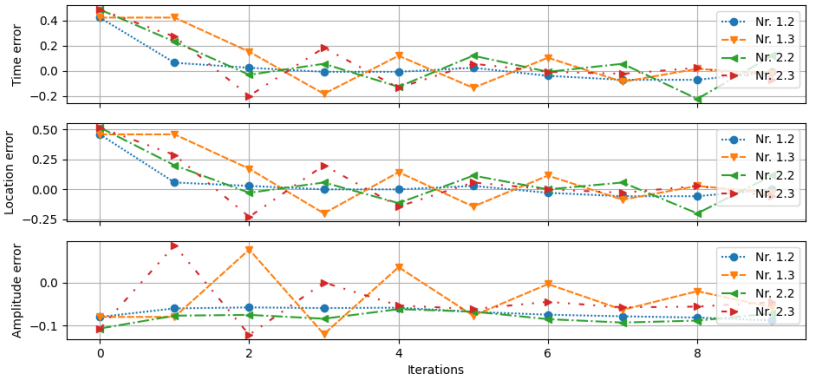

Figure 2.9: Change of defocusing error with iterations where the phase and the amplitude of the wave components are changed. The amplitudes are corrected with two different methods. The errors are shown for an initial gain (Nr. 1.2 and Nr. 1.3) and spectral (Nr. 2.2 and Nr. 2.3) amplitude distribution.

It was observed that after the iterative corrections, some leading waves had higher amplitudes than the focused wave itself in the whole domain. The leading waves are the waves before the focused wave. Similar observations were made with the short domain as discussed in chapter 2.2.4. However, in the long domain, the effects were not as pronounced. Leading waves with higher amplitudes than the focused wave will break prematurely. Waves breaking before the desired location invalidates the results as they cannot be used to create a breaking wave at the prescribed location and time. The leading waves for the last iteration of simulation Nr. 1.4 can be seen in figure 2.10. It is visible that the leading waves have a higher amplitude than the focused wave.

In chapter 2.2.4, it was discussed that the waves are created using velocity inflow boundary condition. The velocity profile at the inflow boundary is calculated with linear extrapolation above the free surface. The linear extrapolation could result in extra fluid flux in the domain, generating higher waves for the leading waves.

Table 2.5: Best iteration results

	Iter	T_{err}	X_{err}	A_{err}
Nr. 1.1	1	0.0010	0.0000	-0.0655
Nr. 1.2	4	-0.0070	0.0000	-0.0593
Nr. 1.3	8	0.0170	0.0286	-0.0196
Nr. 2.1	7	0.0010	0.0000	-0.0944
Nr. 2.2	6	-0.0070	0.0000	-0.0851
Nr. 2.3	6	-0.0070	0.0000	-0.0446

However, here another error plays a role as well. During the iterations, the phases and the amplitudes of the individual wave components are changed. The change in amplitude and phase could lead to the development of a higher wave at a different position than the prescribed focusing location. Having higher leading waves will lead to premature breaking. Therefore, this cannot be used to create focused, breaking waves at a prescribed location and time.

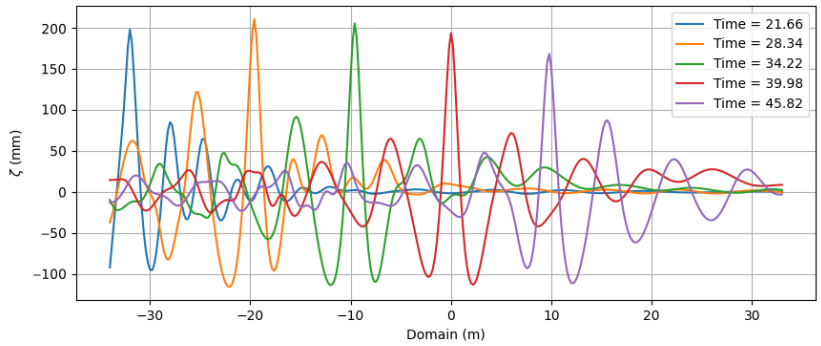

Figure 2.10: Five largest waves in the simulation domain for the last iteration of the simulation where the phases and the amplitudes are changed (Nr. 1.3). The initial amplitudes of the wave components are based on gain distribution. Before the prescribed focused wave, all three waves were larger than the focused wave.

The results show, that using superimposed linear wave components and imposing their potential solution to the inflow boundary as a velocity boundary condition does not lead to a focused wave. Previously reported successes that used similar correction methods, such as Fernández et al. [20] used a wave board to generate the wave components.

2.2.5. Discussion of results

Two methods for creating focused waves are explored as discussed in chapter 2. The first method aims to create focused waves with prescribed characteristics. Prescribing the characteristics gives control over the whole wave event and the global characteristics of the sea state. In the previous chapter, the first method was discussed in detail.

Different approaches were tried to create focused waves at a prescribed time and location to correct the nonlinear wave propagation. Due to nonlinear wave interaction, the focused wave reaches the focusing location sooner. It produces a maximum wave amplitude after the prescribed focusing location. Two different approaches were tried to account for the nonlinear wave propagation. Third-order correction and iterative corrections were implemented. In the iterative method, the initial phase and amplitude of the individual wave components were modified based on the difference in the spectral domain of the wave between the target wave and the resulting wave field.

Using third-order dispersion relation is deemed to have a negligible effect on the results. A slight shift was introduced to the results, and the resulting wave was closer to the desired point. However, the improvement was insignificant as compared to the defocusing error. In this method, only the nonlinear propagation of the individual wave components was considered and did not take into account the nonlinear interaction between the wave components, which appeared to be more significant in causing defocusing.

Using iterative correction methods with Fourier transform was based on the difference of the linear target function and the resulting wave elevation in the spectral domain. After each iteration, the resulting wave elevation was transformed to the spectral domain. The wave components were adjusted for the next iteration step based on the difference of the target and the simulated waves representation in the spectral domain. Several different implementations were tried where only the phase or both the phases and the amplitudes of the individual wave components were modified. Changing only the phases led to a fast decrease in spatial and temporal error. However, the wave amplitude also decreased. Applying amplitude correction led to a better amplitude error. However, the focused wave still did not reach the target amplitude value.

Throughout all the simulations, another issue was present. The leading waves were higher than the focused wave. Having higher leading waves than the focused wave is not acceptable when creating a breaking wave. High leading waves would lead to premature breaking.

It was shown that the used methods are not suitable for creating focused waves with prescribed characteristics. The second approach is described in the following chapter where focused, breaking waves are created, and their characteristics are retrieved posteriorly.

2.3. Created breaking waves

After concluding that the iterative method to create focused waves is not suitable for the creation of breaking waves, a different approach was tried. Breaking waves were created for the experiments based on available data in the literature and by trial and error in the towing tank (See further details on the facility in chapter 3.2). Three different waves were created. Their parameters can be found in table 2.6.

2.3.1. Waves in physical wave tank

The first wave (Wave 1) is based on the wave described by Bos and Wellens [8]. The wave consists of 10 wave components, and their phase was calculated using the linear theory described above. On each wave, a windowing function was applied. The window function consists of a cosine ramp up in one wave period, remains at maximum amplitude for two periods, and ramps down in one. The steepness of the wave components is constant $H/\lambda = 1/50$. The wavelength of the components was chosen, so the overlap between wave groups is minimized [8]. The resulting wavelengths are shown in table 2.6.

The second wave (Wave 2) was created using the same window function used on Wave 1, but 32 wave components were used. The wave components were calculated within a specified frequency band following the wave formulation method of Sriram et al. [49]. The frequency band was defined with a mid-frequency f_{mid} and a frequency bandwidth f_{range} around the mid-frequency. The frequencies of the wave components were equally divided in the frequency band. The steepness of the wave components was kept constant at $\lambda/H = 0.0065$. The resulting wavelength of the components range between $L_{min} = 1.0$ m and $L_{max} = 6.0$ m.

The wave components of the third wave (Wave 3) were formulated similarly to Wave 2 by defining a mid-frequency and a frequency range around it. Similar to the second wave, 32 wave components were used, and the steepness of each component was the same $\lambda/H = 0.0038$. As opposed to the first two waves, no individual groups were applied, but a three-second rump-up and rump-down at the beginning and end of the signal. The resulting wavelength of the components range between $L_{min} = 1.5$ m and $L_{max} = 8.0$ m.

Table 2.6: Created breaking waves. Wave 1 recreated based on literature [8], Wave 2 and Wave 3 designed waves using methods from literature [8] [49].

	Steepness λ/H	Nr. of comp. n	Components	Window
Wave 1	0.02	10	$L = [1.00, 1.10, 1.25, 1.45, 1.70, 2.00, 2.40, 2.90, 3.60, 5.00]$	Groups
Wave 2	0.0065	32	$f_{mid} = 0.85$ Hz, $f_{range} = 0.80$ Hz	Groups
Wave 3	0.0038	32	$f_{mid} = 0.68$ Hz, $f_{range} = 0.68$ Hz	Full

For all three focused waves the focusing location was chosen to be $x_{focus} = 27.00$ m from the wavemaker and the focusing time was chosen to be $t_{focus} = 50$ s. Only the focused wave breaks for Wave 1 and 3, while for Wave 2, the leading wave shows an initial spilling characteristic. In all three cases, the focused wave shows plunging behavior. There are advantages to the different techniques of wave formation. The nonlinear inter-

action between different wave components is presumed to reduce when using windows for individual components. Each regular wave component is released as a group of waves after one another. The method aims to have less nonlinear interaction between the groups, resulting in a focused wave that is more predictable. However, the method is quite dispersive, and the focused wave will be significantly smaller than what linear theory suggests [8]. Applying more components with the group window function leads to a smoother wavemaker signal. Not having separate windows for the groups can lead to higher leading waves, but the dispersion of the waves is smaller [49].

2.3.2. Breaking waves in numerical setting

Breaking waves are created in towing tank where all three waves showed plunging behavior. The waves were recreated in a numerical setting to calculate the characteristics of the wave.

For the numerical analysis, ComFLOW was used. The physical towing tank was recreated in the numerical model, and the waves were generated in two ways. Simulations were carried out mimicking the wavemaker of the physical wave tank. The waves were generated with a body on which the wavemaker motions were imposed. The second wave generation method imposed the free surface elevation and velocity profile at the position of the wavemaker using linear wave superposition as described in section 2.2.1. The superposed wave components were retrieved based on the Fourier transform of the free surface elevation at the wavemaker position.

The dimensions of the numerical setup for both cases can be seen in table 2.7. The setup with piston mode is larger by 0.5 m behind the origin, which is the nominal position of the wavemaker. The extra space is needed for the piston motion of the wavemaker.

Table 2.7: Details of simulation domain to recreate breaking waves. The notations are in line with the NWT representation in figure 2.1

		Unit	Wavemaker motion	Linear superposition
Inflow boundary	$X_{BC,in}$	[m]	-0.50	0.00
Outflow boundary	$X_{BC,out}$	[m]	35.00	35.00
Domain length	L_{domain}	[m]	35.00	35.00
Water depth	h	[m]	1.00	1.00
Domain height	H_{domain}	[m]	2.00	2.00
Resolution x	Δx	[m]	0.02	0.02
Resolution z	Δz	[m]	0.02	0.02
Element number	N	[-]	179k	177k

Interestingly having the same settings for the numerical simulation, described in chapter 2.2.1 the two methods did not result in similar solutions. The waves did not break using the same wavemaker motion for all three waves used in the physical wave tank. However, resulting waves in the numerical setting did not break using the wavemaker motion. Using the linear wave superposition and imposing the velocity profile of the waves at the inflow boundary, the waves resulted in breaking waves for all three waves. The free surface elevation at the focusing location is shown in figure 2.12. The free surface elevation is lagging using the wavemaker approach compared to the waves using linear superposition. The wave heights are also smaller than using the linear superposition method. Such behavior could be explained by having a moving body in the domain, which is the wavemaker. The amplitude of the largest wavemaker motion happens with Wave 3 and is approximately 120mm. In general, the amplitude of the wavemaker motion is much smaller. With the used grid resolution as shown in table 2.7 the wavemaker is moving twelve cells. Twelve cells might be too small for generating waves, hence the lag and the nonbreaking behavior. The created wave field using linear wave superposition is assumed to be more accurate than using a moving body as a wavemaker. Therefore the wave characteristics are determined based on the simulations where the waves are generated by linear superposition.

The free surface elevation at the theoretical focusing location was measured for all three focused waves used in the experiments. Figure 2.11 shows the spectrum of the three waves measured at $x_{focus} = 27.0$ m. Table 2.8 shows the characteristic values of the sea state, such as the significant wave height and the peak period for all three focused waves. The waves have increasing significant wave height and peak periods. However, the peak period of Wave 1 and Wave 2 is close to each other.

Table 2.8: Significant wave height and peak period of the three waves measured at the prescribed focusing location x_{focus} = 27.0 m. The values are based on simulation.

	H_{m_0} [mm]	T_{peak} [s]
Wave 1	69.28	1.90
Wave 2	98.52	2.04
Wave 3	120.01	3.06

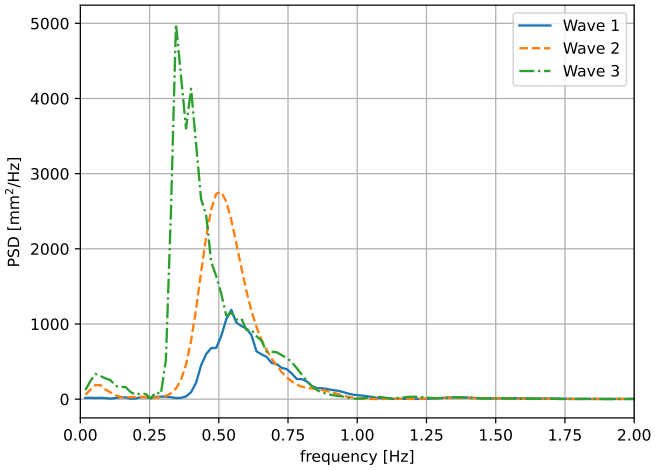

Figure 2.11: Spectrum of the three focused waves. The spectrum is retrieved based on simulation, measured at the prescribed focusing location x_{focus} = 27.0 m.

2.4. Discussion of wave focusing and breaking wave creation

Breaking waves were created as loads for green water impact on a ship. Two methods were explored. The goal of the first method was to create focused waves at a predetermined location and time. The investigation was done in a numerical setting using ComFLOW. The nonlinear interaction between the wave components caused the focused wave to shift both in time and location from the prescribed time and location. Corrections with third-order theory and iterative methods with component phase and amplitude corrections were tried. However, no convergence to the target function was found. In a numerical environment, it was shown that the leading wave reached a higher amplitude than the focused wave. Therefore, making the iterative method not suitable for creating breaking waves in a numerical setting.

After concluding that using the first method will not lead to the creation of breaking waves, another option was implemented. Breaking waves were recreated from literature and created originally with heuristic methods in a physical wave tank. Three waves were created in this manner. The characteristics of the waves, such as their focusing location and time, were investigated with numerical simulations. The spectrum of each wave and its parameters, such as significant wave height and peak period, were retrieved from the simulations as well.

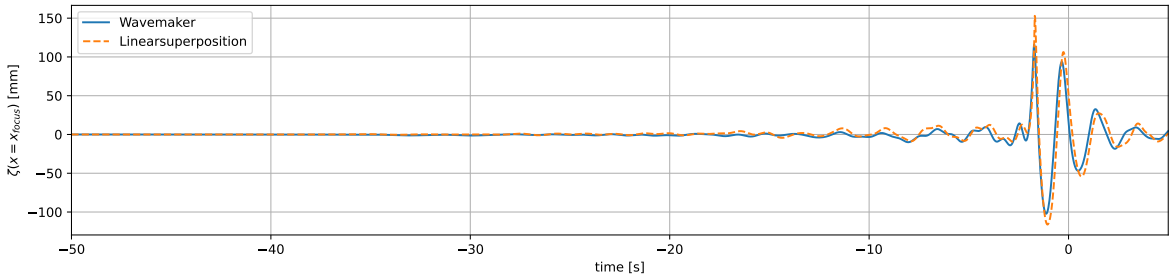

(a) Wave 1

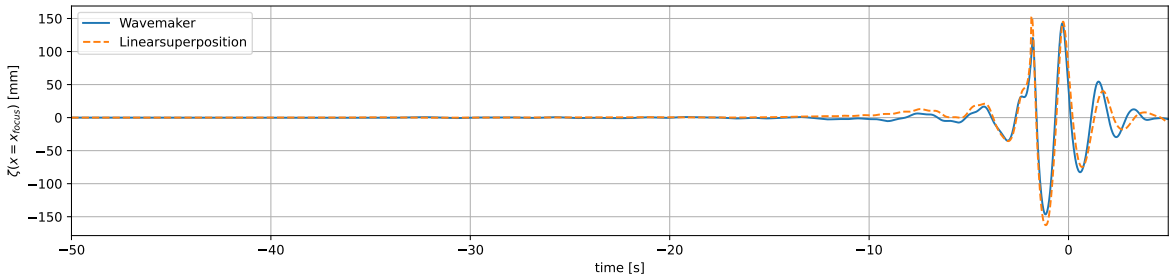

(b) Wave 2

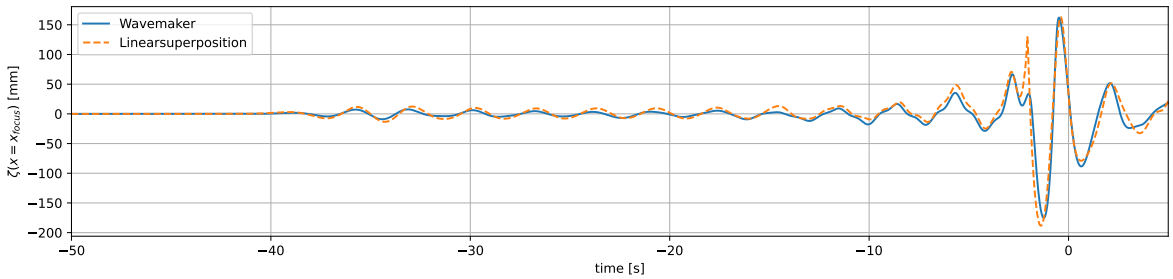

(c) Wave 3

Figure 2.12: Comparison of the free surface elevation for the three waves using two different simulation methods. The solid line shows the surface elevation of the wavemaker while the dashed line the linear wave superposition.

3

Experiments

To investigate green water loads resulting from breaking waves, both numerical and experimental methods are used. First, experiments were conducted to reach the set goals. In this chapter, the conducted experiments will be presented in detail. After the goal of the experiments is presented in chapter 3.1 the experimental setup is discussed in chapter 3.2 then the conducted experiments are described in chapter 3.3.

3.1. The goal of the experiments

The experiments are designed for interaction between a ship at forward speed and a focused, breaking wave. The experimental setup was designed to enable systematic investigation of the effects of changing the ship's LCG with respect to the wave's focusing location at the focusing time, of different ship velocities, and different focused waves. The experimental facility, the model, and the experimental conditions are described below.

3.2. Experimental setup

The experimental setup is discussed in the following. The setup is further broken down into discussion of the experimental facility, the details of the model, and the instrumentation of the model and the facility alike.

3.2.1. Experimental facility

The experiments were conducted in the facilities of the Maritime and Transport Technology department of Delft University of Technology. The small towing tank was used, including its wave generator and motorized carriage. The basin contains freshwater, and the wavemaker was used as a piston-type wavemaker. The details of the tank can be found in table 3.1. The water depth was kept at 1.0 m throughout the experiments. The water level was checked daily. Water loss, in the order of half a millimeter per day due to evaporation, was compensated for to keep the water depth the same.

Table 3.1: Details of the used towing tank [51]

Length	85.00 m
Width	2.75 m
Max water depth	1.25 m
Carriage	Manned, motor driven
Max carriage speed	3.00 m/s
Wave maker type	Flap / piston type, electronic/hydraulic
Wavelength	0.40 - 6.50 m, regular and irregular

3.2.2. Model details

The model was chosen to fit the requirements of the study. The hull had to have an inclined bow shape which is common for ships as opposed to FPSOs. The inclined results in large waterplane area changes with the change in surface elevation. Due to the violent behavior of the process, the model needed to be watertight as

much as possible, not to have water in the model after impacts, and to keep the electrical instruments dry.

The ship model was no. 523 of the Delft Systematic Deadrise Series (DSDS). It is a planing hull with a hard chine and a 25 degrees deadrise angle, a 10 degrees twist angle, and a negative buttock angle of 1.69 degrees [30]. In this experiment, the model was used as a displacement vessel. Details can be found in table 3.2 and the lines plan of the model is shown in appendix B. Due to the violent behavior of the flow during impact, the model deck was made watertight to protect electrical equipment placed in the hull. At the connection of the carriage, a hole is present in the deck for free movement of the model. A breakwater was installed to prevent spraying water from getting into the hull through the hole.

Table 3.2: Parameters of DSDS model no. 523

Name	Symbol	Units	Value
Length between perpendiculars	L_{pp}	m	1.500
Length on waterline	L_{wl}	m	1.517
Breadth moulded	B	m	0.330
Depth moulded	D	m	0.207
Displacement	∇_s	m^3	0.026
Mass	Δ	kg	25.621
Vertical center of gravity	VCG	m	0.165
Longitudinal center of gravity	LCG	m	0.714
Pitch radius of gyration	k_{yy}	m	0.350

3.2.3. Measurement setup

The carriage of the towing tank was used to impose forward velocity on the model. The model was connected to a heave rod through a hinge which enabled the pitching motion of the model. The heave rod was connected to the carriage through a linear bearing allowing the ship to have a free heave motion while limiting roll, surge, and sway. The yaw motion was restricted with a limiter mechanism, resulting in only 2 degrees of freedom, pitch, and heave. The setup of the model can be seen in figure 3.1 and 3.3.

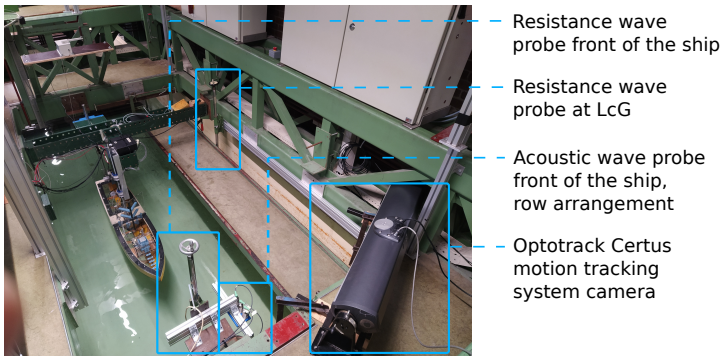

Figure 3.1: Measurement instrument arrangement on the carriage: two resistance wave probes, in front of the ship and at its the LCG, and the camera of the Optotrack Certus motion tracking system.

The sensors were set up to give information about the vessel's motions, including the carriage movement, the loads on the model, and the incoming waves. The instrumentation setup resulted in both the model and the carriage being equipped with sensors. The following sensors were installed on the carriage and the ship:

- The *motions* were measured optically with the Optotrak Certus system. The camera system was attached to the carriage. It was tracking the motions of a reference plate with LED markers attached to the model.
- The *velocity and position* of the model were measured on the carriage with a measurement wheel.
- Vertical *accelerations* of the ship were measured at the bow and the CoG with accelerometers.
- Two *force* transducers were used. One measured the total surge force on the model, and one measured

the axial forces on the superstructure. Both transducers were in-house analog transducers with a measuring range of ±400 N.

- *Pressures* were measured with GE PDCR 42 transducers. The sensors have a circular sensing area with a diameter of $d = 6$ mm, which results in point-like pressure measurement. The sensors are aerated from the back through a metal tube. Thus, they measure the relative pressure, the pressure change with respect to the atmospheric pressure. The layout of the pressure sensors can be found in figure 3.2. The pressures were measured on the deck at 5 locations and on the vertical face of the superstructure at 3 locations.

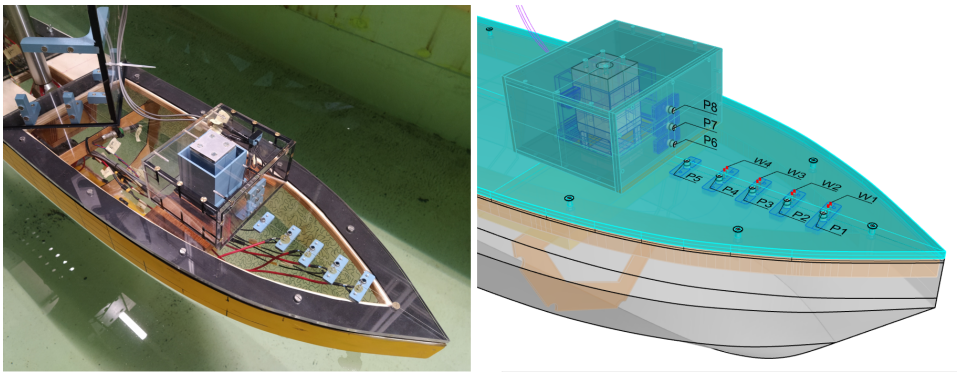

Figure 3.2: Arrangement of pressure sensors on the deck and superstructure of the model. Five sensors are placed on the deck (P1 to P5) while 3 sensors are placed on the superstructure (P6 to P8)

- *Wetness* sensors aiming to check for the presence of water were installed at 4 locations on the deck, mirroring the location of the four foremost pressure sensors along the centerline of the model. Assuming a symmetrical flow on the deck, the absence of the water indicates that the pressures come from air or entrapped air pockets.
- *Wave probes* were installed at two locations. Resistance-based probes at the ship's side measure the free surface elevation at the LCG of the ship and in front of the ship at its centerline, measuring the incoming waves. Acoustics wave probes were installed in front of the ship, next to the resistance wave probe. The acoustic sensors had a three-in-a-row arrangement, with the foremost one being the master sensor. With such an arrangement, steep waves could be measured under speed. The reflected signal cannot be picked up by the master sensor but is received by the following two transducers. The signal is corrected for the reflection abnormalities by the sensor's computer, and a processed, filtered signal is forwarded to the acquisition system

The pressure-, force transducers and accelerometer were calibrated before installation, while the Certus system was calibrated after the model was already in place. The resistance wave probes were calibrated daily. The acoustic wave probe was pre-calibrated. With the use of a reference measurement, the changes in the speed of sound were compensated. The wetness sensors did not need calibration as the voltage passing through was measured directly.

The recorded signals were both analog and digital and varied in sampling frequency. The motion signals were received digitally with a sampling frequency of 100 Hz. The position and velocity signals of the carriage were also received digitally with a sampling frequency of 50 Hz. All other signals were analog and had to be converted to a digital signal through an acquisition system. The acquisition system sampled the analog signals with a 1000 Hz frequency through an analog low-pass filter with a cutoff frequency at 100 Hz. The measured signals were synchronized between the three sources and saved for post-processing.

3.2.4. Timing of carriage startup

For the experiments, the objective was to control the position of the LCG of the ship in space and time with respect to the stage of breaking of the focused wave. The timing of the ship's movement with the wavemaker is an essential aspect of the conducted experiments. Accurate timing between repeated runs leads to sounder quantification of repeatability and statistical data.

The timing between the wavemaker signal and the carriage startup was not available by default. Two PCs were

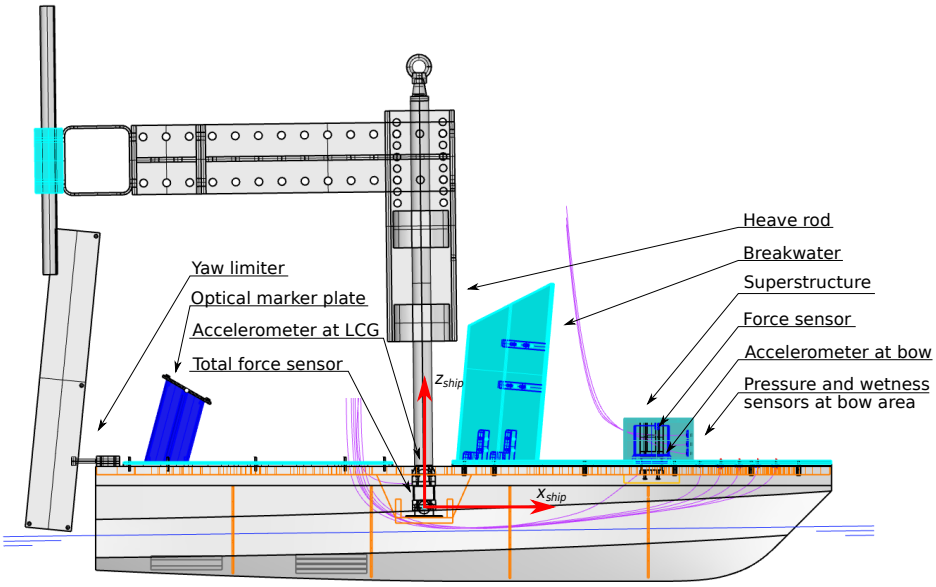

Figure 3.3: Side view of the DSDS model no. 523 setup including placement of the mechanisms such as heave rod and yaw limitation, optical tracking system, and instrumentation, such as force and pressure transducers, accelerometers, and wetness sensors.

used during the experiments, one to control the carriage movement and another to control the wavemaker. A stable, wired connection for synchronization between the two control PCs was not present at the used facility. In addition, the carriage could only be started up manually. Because of the manual start of the carriage and the lack of a stable wired connection, a trigger signal, a flashing LED light, was built to indicate when to start the carriage. The carriage was started up at the third flash of the LED. The manual start of the carriage inherently creates errors in the timing between the carriage and the wave, but the error was kept small. The errors are quantified later in chapter 4.1.1.

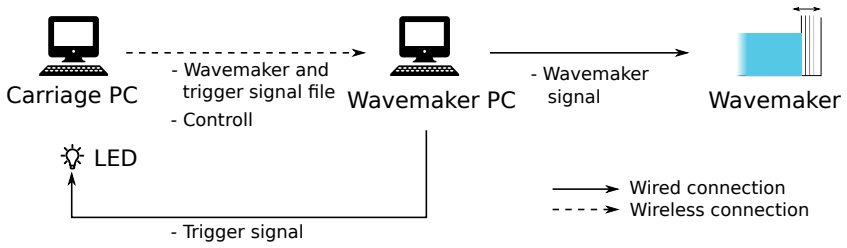

Figure 3.4: Schematic of the data connections between the used computers (wavemaker and carriage PC) and equipment (carriage and wavemaker) during the experiments.

For the timing of the wavemaker and the carriage movement, the following inputs were used. The initial position of the carriage x_{ini} with respect to the wavemaker (see figure 3.7), the position of the model at the theoretical focusing time of the waves $x(t = t_{focus})$, and the position trace of the carriage $s(t)$ which is shown in figure 3.5. The position trace ($s(t)$) was measured for all the different velocities beforehand to be used in the timing method. First, the distance the carriage needs to travel to the prescribed position $x(t = t_{focus})$ is established.

$$\Delta x_{travel} = x_{ini} - x(t = t_{focus}) \tag{3.1}$$

From the measured position trace of the carriage ($s(t)$), which was different for different velocities, the time to travel the distance could be retrieved (Fig. 3.5. Knowing the time of breaking and the needed travel time, the time of the trigger signal with respect to the theoretical focusing time of the wave is calculated as:

$$t_{trig} = t_{focus} - \Delta t_{travel} \tag{3.2}$$

After each run, the carriage returned to a slightly different position, changing x_{ini}. As the timing depends on the initial position of the carriage, the timing between the wavemaker and the trigger signal had to be redone for every experiment. The inputs were adjusted between different runs to make sure that the model was at the desired position at the desired time.

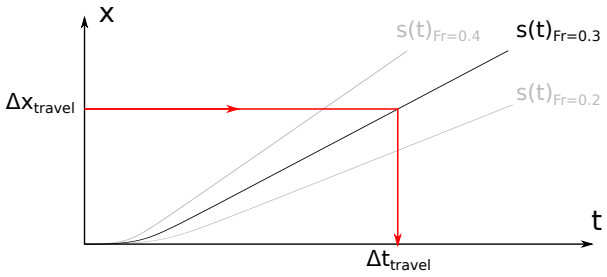

Figure 3.5: Schematic representation of the position time trace of the carriage. The figure shows the relative distance traveled in time from the startup of the carriage for three different ship speeds.

3.3. Conducted experiments

First, some of the model properties were identified through measurements, then the green water loads were investigated using three different ways, where the ship's position was changed to the location of the breaker at the time of breaking, the vessel speed was changed, and three different types of breaking waves caused loads were looked at.

3.3.1. Model properties

Model properties such as calm water resistance and the motion response to waves were identified first. The calm water resistance was realized at three different speeds corresponding to Froude numbers of Fr =0.2, 0.3, and 0.4. The RAO for $Fr = 0.3$ was determined with regular waves, which had a steepness of $H/\lambda = 1/100$, and their length range can be seen in table 3.3. The resonance for a stationary ship is expected to occur at a wave- to ship length ratio of $\lambda/L = 1$. The measured regular waves are chosen so it captures the resonance frequency within their range.

Table 3.3: Response Amplitude Operator test conditions

Fr	L/λ
0.3	0.60, 0.80, 1.00, 1.20, 1.40, 1.60, 1.80, 2.00

Due to the ship having velocity during the RAO measurements, the resonance frequency shifts to higher wave-length ratios. The resonance should happen at an encounter wavelength to ship length ratio, which is beyond the tested waves shown in table 3.3. The encountered wavelength to ship length ratio, which is calculated posthumous, is shown in table 3.4 The results are shown in figure 3.6. It can be seen that resonance is not reached.

Table 3.4: Encounter wavelength under speed

Fr	L/λ_{enc}
0.3	0.15, 0.24, 0.33, 0.42, 0.52, 0.57, 0.75, 0.87

Natural frequencies of the vessel motion were identified through a free oscillation test in both heave and pitch in separate measurements in calm water and without speed. To avoid reflected waves from the tank walls to influence the results, only the first period is taken as the natural period of the motion, and the natural frequency is calculated from that. The results can be found in table 3.5.

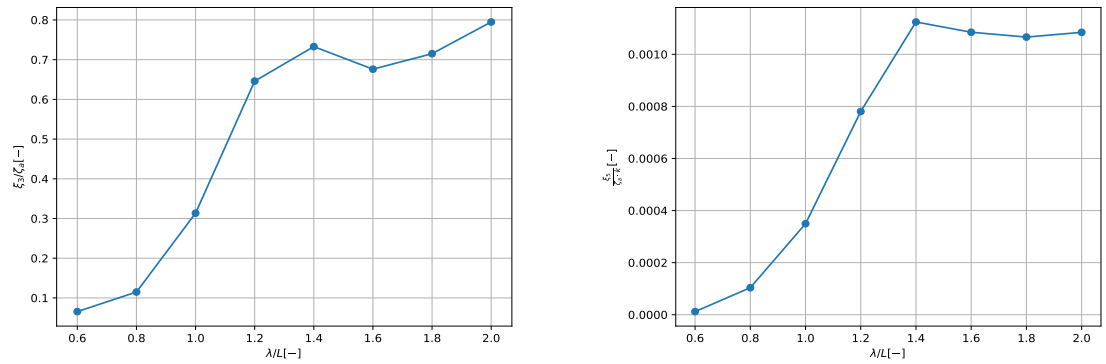

(a) RAO - Heave

(b) RAO - Pitch

Figure 3.6: Response Amplitude Operator (RAO) of DSDS model no. 523 with Fr=0.3

Natural frequencies of the two force sensors are also measured. An impulse-like load was applied on the box, and the ship's stern in the longitudinal direction is a separate measurement. The natural frequencies were identified through the spectral analysis of the measured signals. The results can be found in table 3.5.

Table 3.5: Measured natural frequencies of model motions and force transducers

Heave motion	$f_{eig,\,heave}$	1.36 Hz
Pitch motion	$f_{eig,\,pitch}$	1.31 Hz
Total force transducer	$f_{eig,\,Rtm}$	8.10 Hz
Box force transducer	$f_{eig,\,Fbox}$	107.20 Hz

The attached structure influences the natural frequencies of the force transducers. In the case of the total force sensor (Rtm), the water surrounding the ship also influences the frequency. As both force transducers are nominally identical, the significant change in their natural frequency is a result of having a larger mass attached to the total force sensor. The natural frequency is relatively low and is in the range of important frequencies during the measurements themselves.

3.3.2. Experimental conditions

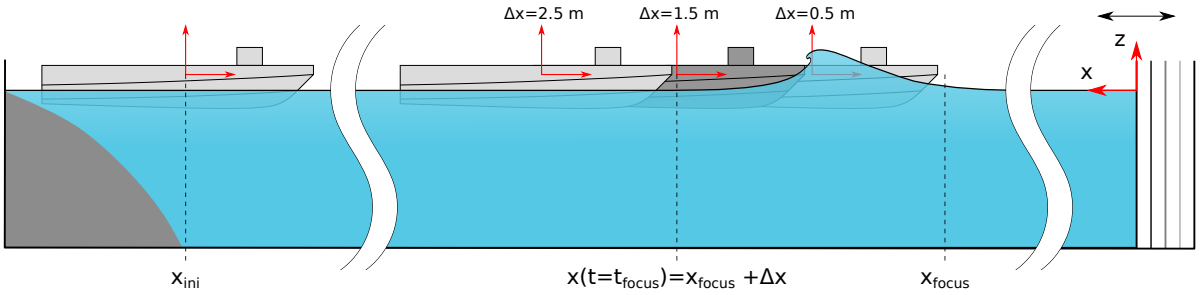

Figure 3.7: Sketch of towing tank setup (not to scale) including the ship and the axis systems of the towing tank. The beach is on the left side, while the wavemaker is on the right. The initial position of the model (connected to the carriage) is shown at the start of the experiment x_{ini}. The other three ship positions for different Δx are illustrated at the focusing time.

In the experiments, the main focus was on the effects of changing the position of the LCG of the ship with respect to the focus point of the breaking wave. Variations of ship speed were also performed, and different focused, breaking waves causing impacts were studied.

Distance variations were done by changing Δx, representing the distance between the LCG of the ship and the theoretical focus point of the wave at the theoretical focusing time. Five different Δx were studied. Wave 1 was used for all five Δx, ensuring the same input energy. In figure 3.7 three positions out of the five Δx are shown. The initial position of the ship before each run is represented as well. At the focusing time t_{focus} the LCG of the ship has a distance of $x(t = t_{focus})$ from the wavemaker. The distance $x(t = t_{focus})$ is calculated as

the sum of the theoretical focusing location and Δx. For $\Delta x = 1.50$ m, the wave breaks on the ship's bow. The other four Δx were used. Two Δx placing the ship closer to the wavemaker ($\Delta x = 1.0$ m and $\Delta x = 0.5$ m), and two placing the ship further from the wavemaker ($\Delta x = 2.0$ m and $\Delta x = 2.5$ m) at the focusing time.

Three different speeds $V_{ship} = 0.771$, 1.156, 1.541 m/s were tested with Wave 1. The three speeds corresponds with Froude number $Fr = V_{ship}/\sqrt{L_{wl} \cdot g} = 0.2$, 0.3, and 0.4. The wave must be in a similar breaking stage during impact for all seeds to compare the loads for different velocities. As the vessel speed is varied, the timing method for different velocities needs to be done in both space and time to achieve an impact with the wave in the same breaking stage. A moment in time was selected when the total force on the ship reached its maximum in series W1_d15_Fr03 (Wave 1, $\Delta x = 1.50$ m, $Fr = 0.3$), and translated to equivalent relative positions of the ship at different velocities. This resulted in $\Delta x = 1.87$ m for Fr = 0.2 and $\Delta x = 1.13$ m for Fr = 0.4.

Three focused waves, Wave 1, Wave 2, and Wave 3, with increasing wave heights, were created for the experiments. All three waves are focused at x_{focus} and result in a plunging breaking wave. However, the distance and time between focusing and breaking depends on the wave height and is different for all three. In chapter 2.3.1 the method of creating the focused waves was described. The green water events of the three different focused waves were studied. Δx was tuned for the wave to break on the bow of the ship in the same breaking stage in all three cases. The tuning resulted in $\Delta x = 2.01$ m for Wave 2, and $\Delta x = 1.31$ m for Wave 3. Table 3.6 shows the main experiments.

Table 3.6: List experimental test conditions

Series name	Wave	Distance [m]	Froude number [-]
W1_d25_Fr03	Wave 1	$\Delta x = 2.50$	$Fr = 0.3$
W1_d20_Fr03	Wave 1	$\Delta x = 2.00$	$Fr = 0.3$
W1_d15_Fr03	Wave 1	$\Delta x = 1.50$	$Fr = 0.3$
W1_d10_Fr03	Wave 1	$\Delta x = 1.00$	$Fr = 0.3$
W1_d05_Fr03	Wave 1	$\Delta x = 0.50$	$Fr = 0.3$
W1_d19_Fr02	Wave 1	$\Delta x = 1.87$	$Fr = 0.2$
W1_d11_Fr04	Wave 1	$\Delta x = 1.13$	$Fr = 0.4$
W2_d20_Fr03	Wave 2	$\Delta x = 2.01$	$Fr = 0.3$
W3_d13_Fr03	Wave 3	$\Delta x = 1.31$	$Fr = 0.3$

3.4. Discussion of experimental setup

In this chapter, the experimental setup was presented, which was used to investigate green water loads on deck and deck structure. The setup was designed to measure the incoming waves, motion response of the model, global, and local loads. The most crucial part of the experiment setup was to create a timing procedure between the wavemaker and the carriage. Correct timing is needed to create a controlled interaction between the ship and the focused breaking wave. An LED was used for timing which flashed three times. On the third flesh, the carriage is started up manually. The solution inherently opens the possibility for human error, which could influence the measurement repeatability and reliability.

The conducted experiments are also described in this chapter. The main research goal of the thesis is to *"investigate the effects of breaking waves on the load over the front deck and superstructure of a ship with forward speed"* as presented in chapter 1.3. The goal was investigated by changing three parameters. First, the ship's distance to the breaking wave was changed. The ship was sailed through different focused, breaking waves, and the Froude number was varied for one of the breaking waves. The results of the experiments will be discussed in chapter 4.

4

Results and Discussion

In the previous chapters, the background in green water research was presented, methods were discussed of creating focused waves, and the experimental setup and conducted experiments were described. In the present chapter, the results of the experiments will be discussed. As discussed in chapter 3.2 the timing of the experiments was an important factor.

4.1. Post-processing

Before examining the results of the experiments the signals and data sets are processed. Most of the signals are analog, therefore require filtering to clean them from noise. The different runs for the same set of experiments are combined so they are comparable. Finally, a brief quality assessment of the retrieved data is presented.

4.1.1. Synchronization of runs

The repeated runs for the same conditions needed to be synchronized with each other so they could be compared and the variability of the results could be interpreted. A trigger signal was created that would indicate when to commence the manual startup procedure. Manual startup means that synchronization between the input signal sent to the wave maker and the measured signals from the ship requires attention.

The synchronization process involves a correction in space for the initial position of the ship and in time for the beginning of the measurement. The initial position of the carriage varies slightly for the different runs. The measurement always starts before the carriage start up, but the beginning of the measurement varies for the different runs (see Fig. 4.1a). The initial location x_{ini}, the prescribed location of the ship's LCG at the focusing time $x(t = t_{focus}) = x_{focus} + \Delta x$, and the position trace of the carriage $s(t)$ was used to synchronize the different runs. For each run, the initial position of the ship's LCG was measured from the wavemaker. Based on the carriage position trace, the actual position of the ship's LCG in the coordinate system of the tank is known throughout each run. The focusing time of the wave t_{focus} for each run is when the ship's LCG is at the prescribed location, as shown in figure 4.1a. The runs are synchronized setting the focusing time to t_{focus} = 0.0 s as show in figure 4.1b. After synchronization at t = 0.0 the ships LCG is at the prescribed location for each run. The initial position of the ship's LCG and the focusing time is presented in table 4.1 for four runs in two different series. The synchronization process assumes that the measurement wheel has no slip therefore the measured position has no error, and the initial position measurement of the carriage is accurate. With the synchronization the initial position error and the different beginning of the measurements are corrected for and the runs can be compared with each other allowing statistical analysis of the results.

One (human) error in the synchronization process remains and needs to be quantified. It is the time between trigger and manual startup of the carriage that cannot be guaranteed to always be the same. The (small) timing error leads to an error in the prescribed position of the ship. The position error could influence the characteristic of the impact. To verify that the error is indeed small, the position error will now be quantified.

The timing error will be based on the measured surface elevations, because the nonlinearity in the free surface in the leading waves before breaking is small, the variability between runs is small. Taking the cross

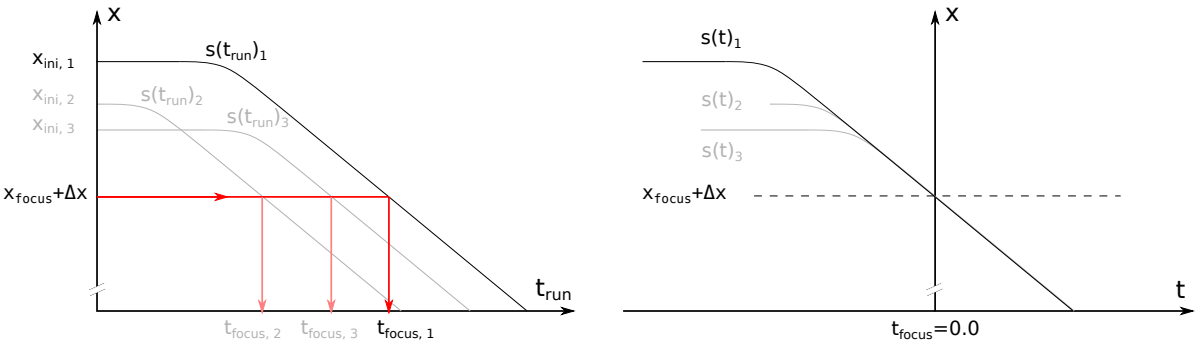

(a) Before synchronization

(b) After synchronization

Figure 4.1: Schematic representation of the synchronization method of the different runs. The position trace of the ship's LCG is shown before ($s(t_{run})$) and after ($s(t)$) synchronization for three runs in the same series. The initial position and the start of the measurement are slightly different for each run. The synchronization is based on the time (t_{focus}) when the ship's LCG is as the focusing location (x_{focus}).

Table 4.1: The focusing time of the wave and initial position of the ship's LCG for different runs. The complete table can be found in appendix E.

Series name	Run Nr.	x_{ini} [m]	t_{focus} [s]
W1_p25_Fr03	709	73.362	75.89
	730	73.328	78.84
	732	73.324	79.12
		⋮	
W3_p13_Fr03	333	73.144	76.24

correlation of each pair of signals in a series of tests, the time delay between said pairs is calculated. The maximum of these time delays for each series is presented in table 4.2. The position error is calculated based on the ships speed and the maximum time delay $x_{err} = t_{err} \cdot V_{ship}$. The position error indicates the error range of the location of the ship's LCG due to the inaccuracy of the manual startup of the carriage.

The error is negligible for smaller ship speeds, but becomes considerable for larger speeds. At the largest ship speed, there is a shift of 14.0 cm in the position of the ship, while a 2.8 cm shift is the smallest. Compared to the length of the ship, that difference is 10%, which is significant and needs to be considered when discussing the results.

Table 4.2: Range of timing differences of repeated runs based on the maximum value of the front wave probe, and calculated travel distance of all runs in each series.

Series name	t_{err} [s]	x_{err} [m]
W1_d25_Fr03	0.024	0.028
W1_d20_Fr03	0.032	0.037
W1_d15_Fr03	0.093	0.108
W1_d10_Fr03	0.052	0.060
W1_d05_Fr03	0.026	0.030
W1_d19_Fr02	0.053	0.041
W1_d11_Fr04	0.090	0.139
W2_d20_Fr03	0.121	0.140
W3_p13_Fr03	0.117	0.135

4.1.2. Data filtering

The analog signals are filtered only as the digital signals are received already after filtering. The filtering process is done by looking at the frequency spectra of the sensor in a situation where the noise is the same as during an impact. Such scenarios are the calm water runs, where the vibrations from the carriage are re-

ceived by the model and the sensors. Such scenarios are present at the beginning of all runs where waves are not yet encountered but the carriage is already running as well as in separate measurements. After observing the frequency spectra of the noise and comparing that with the spectra which involves an impact, the signals are filtered based on where significant noise was found. The filtering is done with a second-order Butterworth filter in all cases.

Resistance wave probes have small noise spectra. In the noise spectra, some energy can be observed above 10 Hz and a clear peak can be seen in several runs above 25Hz. The energy during impact is concentrated in lower frequencies, below 5 Hz. The signals of the resistance wave probes are filtered above 10 Hz.

The noise spectra of the total force sensor show peaks around 8 Hz and above 16 Hz till 110 Hz. The resonance of the model is 8 Hz which explains the peak around that frequency. However looking at the impact of the signal, the spectrum is more widespread around the resonance frequency. During the impact the vetted surface area of the hull changes a lot, therefore its added mass varies significantly which influences the resonance frequency. It is assumed that the energy shown in the spectra around the resonance frequency is a result of this and can be tied to resonance phenomena therefore it should be filtered out. The noise spectra contain energy for higher frequencies while there is insignificant or no energy for higher frequencies during the impact. For the total force sensor, 6.0 Hz and higher frequencies are filtered out. For one series on which the comparison was made can be seen in figure 4.2.

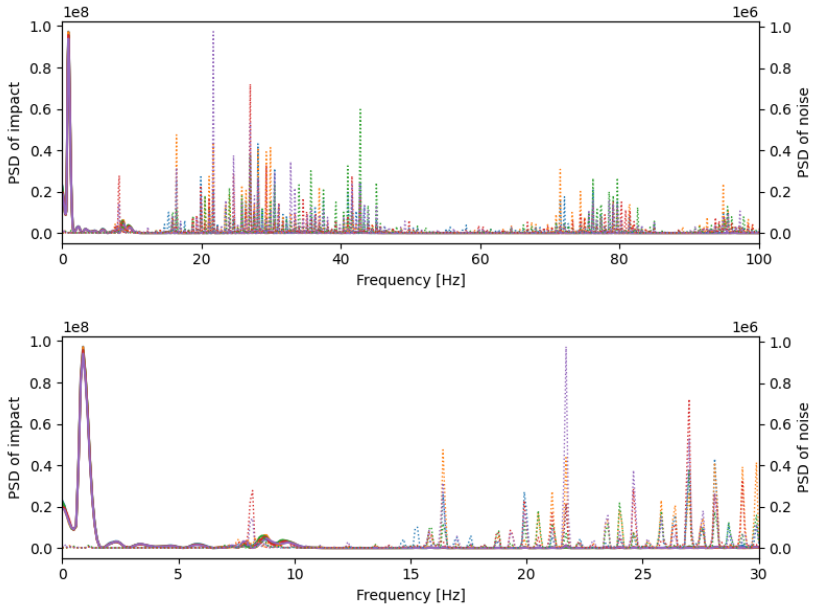

Figure 4.2: Power spectral density (PSD) of total force F_{tot} for all nominally identical repeated experiment in the W1_p20_Fr03 series during and before impact, under calm water condition which is considered as the noise spectra of the sensor. The continuous lines are the impact spectres and the dotted lines are the noise spectres

The force sensor of the box shows similar characteristics to the total force transducer. The noise spectra also show a peak around 8 Hz and a peak around 100 Hz. The latter is close to its eigenfrequency, while the first is a resonance induced from the model itself. Between these frequencies energy still can be found in the noise spectrum. Looking at the spectra of the impacts, energy is spread to higher frequencies as compared to the total force sensor. This is due to the abrupt impact which results in a jump in the force value. As to be able to show such behavior the cut-off frequency is chosen at 15 Hz. With this, the resonance of the total model is still present in the signals, but the resonance of the box itself and other noise is cut out.

Pressure sensors barely show any noise characteristics, but in most cases, a clean spike can be observed at 50 Hz. Looking at the density spectra during the impact the frequency is spread to higher frequencies as compared to other signals which are important to incorporate and cannot be left out of the analysis. The 50 Hz spike is assumed to originate from the electrical network, therefore, it should be excluded. The applied filter for the pressure sensors is a low-pass filter with a cut off frequency at 45 Hz.

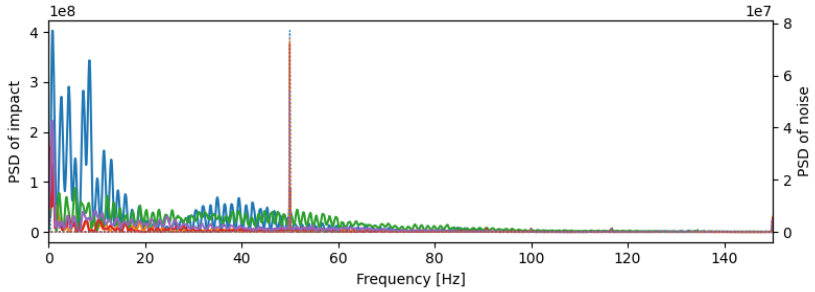

Figure 4.3: Power density spectra of P7 pressure sensor for all nominally identical repeated experiment in the W1_p20_Fr03 series during and before impact, under calm water condition which is considered as the noise spectra of the sensor. The continuous lines are the impact spectres and the dotted lines are the noise spectres

The wetness sensors are only filtered above 49 Hz to avoid interference of the electrical network. Looking at the power spectra there is insignificant energy above 15 Hz. The applied filter for the pressure sensors is a low-pass filter with a cut off frequency at 45 Hz.

The noise spectra of the accelerometers are quite small and only observed in high frequencies. There is some energy in the low-frequency end, however, that is expected while sailing through calm water. The spread of power in the noise spectra does not overlap with the power of the signal during the impact therefore frequencies above 13 Hz are cut from the signal.

Ship motions are recorded through optical means and filtered before the data is retrieved by the computer. Therefore, the motion signals do not require any further filtering. Carriage position trace and velocity are obtained from the measurement wheel which provides pulses. The signals are smooth due to their nature, therefore, they do not need filtering.

4.2. Distance variation

Distance variation was done by changing Δx, representing the distance between the LCG of the ship and the theoretical focus point of the wave at the focusing time. Five different Δx were used in the experiments. The focused wave was the same, containing the same energy, for all different Δx. Changing Δx resulted in impacts, where the wave is in three characteristically different breaking stages: broken, breaking, and unbroken. In figure 4.4, a representation of the impact with three different stages of the wave is shown schematically. Out of the five distance variations, one resulted in impact with the wave in its breaking stage, where the wave is breaking onto the bow ($\Delta x = 1.5$ m), two in unbroken impacts, where the wave is unbroken during the impact ($\Delta x = 1.0$ m and $\Delta x = 0.5$ m), and two with broken stage, where the wave is already broken ($\Delta x = 0.50$ m and $\Delta x = 2.5$ m). The experiments were repeated five times for each Δx.

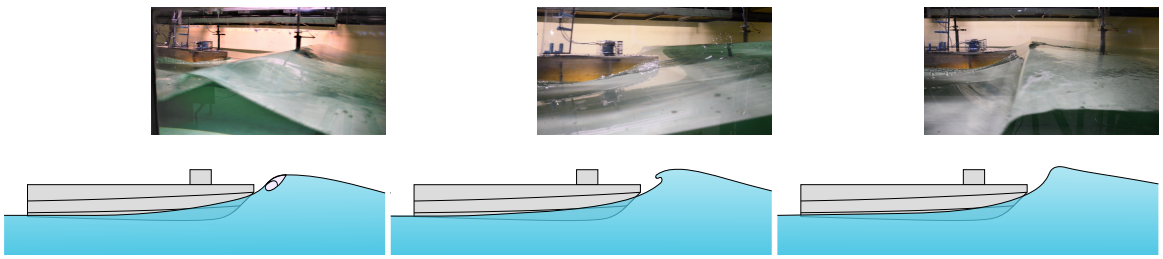

(a) Broken stage, $\Delta x = 2.5$ m (b) Breaking stage, $\Delta x = 1.5$ m (c) Unbroken stage, $\Delta x = 0.5$ m

Figure 4.4: Schematic representation of the focused wave and the ship for three characteristically different breaking stages of the focused wave. Corresponding images from experiments for the three different impact types are also shown.

4.2.1. Forces

In figure 4.5 the forces for the five repetitions are presented for all the different Δx. The forces on the ship as a whole and the forces on only the superstructure are shown. Figure 4.6 shows the peak forces during the green water event for the whole ship and for the superstructure.

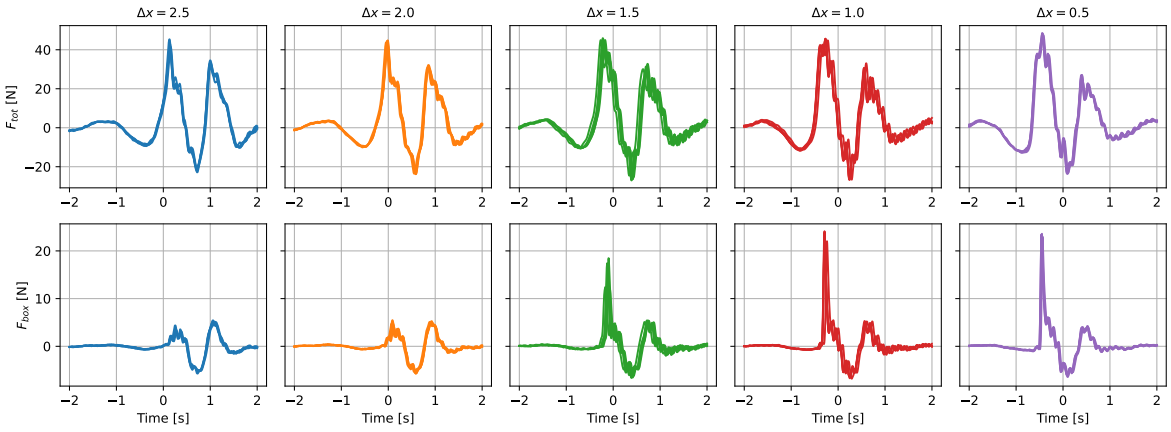

Figure 4.5: Comparison of forces of five green water events caused by the same focused wave in different breaking stage. The different stages are achieved by changing the position of LCG of the ship with respect to the theoretical focal point of the breaking wave with Δx at the theoretical focusing time. In each case the time development of the mean value of the forces is shown for five repeated runs for each different Δx. The minimum and maximum value is also presented. The mean surge force is subtracted from the recorded total force.

The development of the force on the ship as a whole has only small differences between breaking stages. In contrast, the forces on the superstructure vary greatly with the change of Δx. Looking at the forces on the superstructure, impacts of the wave in an initially unbroken stage ($\Delta x = 1.0$ m and $\Delta x = 0.5$ m) result in an initial peak-like force development, while impacts of broken stage ($\Delta x = 2.0$ m and $\Delta x = 2.5$ m) do not display such behavior. The impact of the breaking stage ($\Delta x = 1.5$ m) still displays initial spike-like force development. However, the peak for the breaking impact is less pronounced compared with unbroken impacts. Table 4.3 shows the average of the maximum forces on the ship and the superstructure for all the different Δx. The average of the total impulse on the superstructure is shown as well. Looking at the values, there is a factor of three difference in the impulse on the superstructure between different breaking stages. Looking at the impulse data and the force development on the superstructure, it can be said that the impulse contained in only the peak of the impact with the wave in unbroken stage ($\Delta x = 1.0$ m and $\Delta x = 0.5$ m) is approximately the same or even higher as the impulse contained in the total load of a broken stage impact. The change in Δx appears to have a large influence on the development of the force on the superstructure and, therefore, on the impulse.

Table 4.3: Average of maximum force on the ship as a whole (F_{tot}) and on the superstructure (F_{box}), and the total impulse of the impact on the superstructure (I_{box}). The average values are calculated from the five repeated runs for each different Δx

Δx [m]	2.5	2.0	1.5	1.0	0.5
F_{tot} [N]	42.55	44.37	45.13	45.36	47.91
F_{box} [N]	3.51	4.84	15.06	22.69	23.17
I_{box} [N·s]	0.80	0.95	1.82	2.20	2.33

Comparison of the force peak and impulse on the superstructure between the two impacts with the wave in unbroken stage ($\Delta x = 1.0$ m and $\Delta x = 0.5$ m) shows only a slight change in magnitude (see table 4.3). The force development on the superstructure is similar for both cases. The maximum recorded force is only slightly higher for $\Delta x = 0.5$ m. This maximum force is potentially the maximum force exerted on the superstructure in the sea state which is represented by the focused wave (see 2.3.2). Further investigation needs to confirm that this is indeed the maximum force.

The encounter of the ship with the breaking wave in varying stages of breaking, leads to large variations of impact force and impulse on the superstructure, but not to large variations of force and impulse on the ship as a whole, see figure 4.6. Table 4.3 presents the maximum forces on the ship and the superstructure for all Δx. The coefficient of variation (CV, calculated as the fraction of the standard deviation over the mean value $CV = \frac{\sigma}{\mu}$) is calculated for the maximum force on the ship and the superstructure recorded in the five different Δx shown in table 4.3. The CV of the maximum force on the ship is $CV_{F_{tot}} = 0.04$ while the CV of the maximum force on the superstructure is $CV_{F_{box}} = 0.61$. One order of magnitude difference is found in the

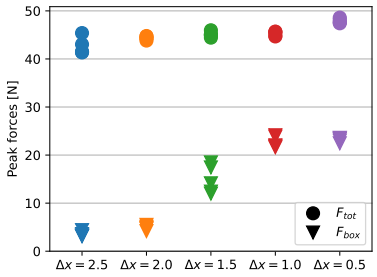

Figure 4.6: Comparison of peak forces of five green water events caused by the same focused, breaking wave in different breaking stages. The peak forces are shown for the ship as a whole (circular markers) and for the superstructure (triangular markers). The different stages are achieved by changing the position of LCG of the ship with respect to the theoretical focal point of the breaking wave with Δx at the theoretical focusing time. In each case, the peak value of the forces is shown for five repeated runs for each different Δx. The mean surge force is subtracted from the total force.

variation of the forces on the entire structure compared to the local structure on deck. A small perturbation in the input, such as the variation of Δx, has a pronounced effect on local forces but not on the global loads on the structure.

It is concluded from figure 4.5 and 4.6 and table 4.3 that the breaking stages of the focused wave have a negligible effect on the total forces. At the same time, the influence on the magnitude and development of forces on the superstructure is considerable. For the same energy input, the impact with a wave in an unbroken stage (Δx = 1.0 m and Δx = 0.5 m) leads to the most severe forces on the superstructure. Even when the wave is in its breaking stage (Δx = 1.5 m), the impact force on the superstructure is not as high as with wave impacts in an unbroken wave stage.

4.2.2. Pressures

Pressures were also recorded on the deck and the vertical wall of the superstructure during impacts. In figure 4.7 a comparison of pressures of three Δx is shown. The three Δx correspond with the three characteristically different wave breaking stages (Fig. 4.4). The figure shows the pressures recorded on pressure sensor P5, which is located on the deck, closest to the superstructure (Fig. 3.2). Each sub-figure shows the impact of a different breaking stage. 4.7a shows the impact of the wave in broken stage (Δx = 2.5 m), 4.7b the impact in the breaking stage (Δx = 0.0 m), and 4.7c the impacts in the unbroken stage (Δx = 0.5 m). Five repetitions were done for each Δx. The figures show the pressures for all five repetitions.

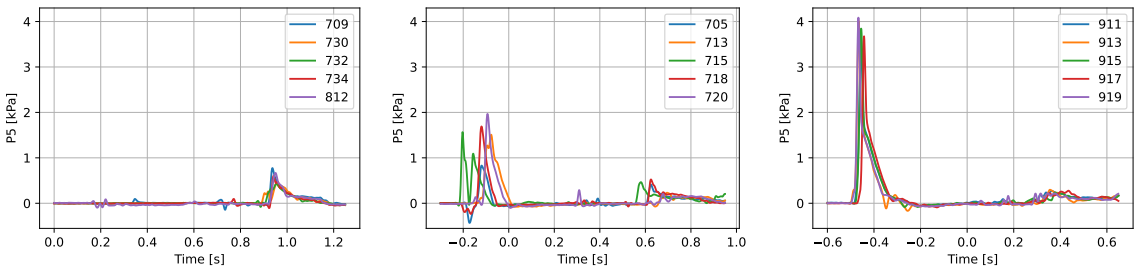

(a) Broken wave stage, $\Delta x = 2.5$

(b) Breaking wave stage, $\Delta x = 1.5$

(c) Unbroken wave stage, $\Delta x = 0.5$

Figure 4.7: Development of the pressure during impact for three characteristically different green water events. The different stages are achieved by changing the position of LCG of the ship with respect to the theoretical focal point of the breaking wave with Δx at the theoretical focusing time. The figure shows the pressure development on pressure sensor P5 (located on the deck close to the superstructure) for all five repetitions of the three breaking stages.

Negative pressures can be observed in all three cases before or after the impact. Such negative pressures are recorded when the sensor is getting wet, or the water is leaving the sensor. These negative pressures are due to the sensors changing temperature. Other explanations such as accelerations are unlikely to cause such pressures. The accelerations were measured on the bow and at the LCG and no significant accelerations were seen at the appearance of the negative pressures.

As can be seen in figure 4.7 the pressures recorded during the broken wave impact ($\Delta x = 2.5$ m) are close to zero. Some degree of disturbance can be observed from 0.1 s due to the presence of water on the sensors. The wave impact causes significant pressures for the other two shown events, where the wave is in its breaking stage ($\Delta x = 1.5$ m) and its unbroken stage ($\Delta x = 0.5$ m). The pressure build-up is steep for $\Delta x = 1.5$ m and $\Delta x = 0.5$ m, but the pressure build-down changes between the two different breaking stages. In the case of impact with the wave in its unbroken stage ($\Delta x = 0.5$ m), the pressure starts with a spike where the build-down is as steep as the pressure build-up. The build-down turns into a more gradual decrease. The pressure development shows that the pressure impulses are more significant for impacts with the wave in an unbroken stage ($\Delta x = 0.5$ m). These observations are in line with the observation done on the force development on the superstructure.

A second green water event happens when the bow submerges again in the water after sailing through the focused breaking wave. For $\Delta x = 2.5$ m, a pressure peak can be discovered around 0.9 s, which corresponds with the second submergence of the bow. The loads caused by the second event can be seen for the other two impacts as well. However, the pressure development for the second event is less pronounced than for the first event. The second green water event has dam-break-like characteristics.

For all five Δx the average maximum peak pressures are shown for each pressure sensor in figure 4.8. The average of the maximum peak pressure is calculated from the five repetitions of the impact for all five Δx. Only a slight change can be seen in the recorded pressures on the deck for different Δx. Pressure sensor P5, which was discussed earlier, is an exception. P5 is located on the deck but close to the bottom of the superstructure. The pressure development and the changes in the maximum peak pressure of P5 resemble the pressures on the superstructure more than the pressures recorded on the rest of the deck. This is important for the design of ships: impacts on the wall of the superstructure facing the wave also cause pressure peaks on the deck.

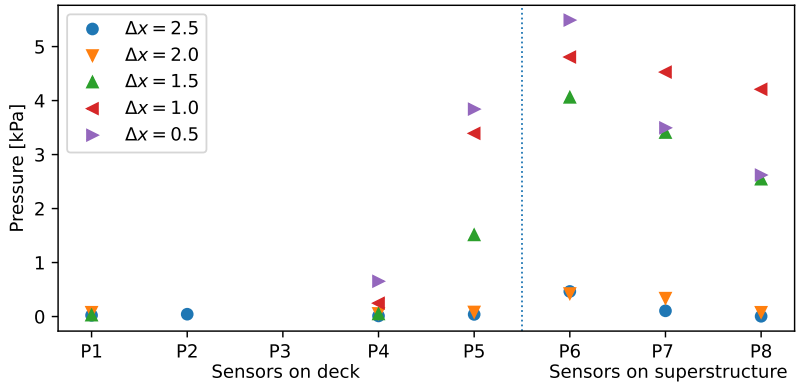

Figure 4.8: Comparison of the average of the maximum peak pressures recorded by pressure sensors during five green water events caused by the same focused, breaking wave in different breaking stages. The different stages are achieved by changing the position of the ship's LCG with respect to the focal point of the breaking wave with Δx. The vertical line separates the pressure sensors located on the deck and the superstructure. Due to sensor failure during the experiments, some data are missing from the figure.

In figure 4.8 a notable difference can be seen in maximum pressures on the superstructure (P6 to P8) and on P5 for different Δx. The difference is between impacts of breaking and unbroken ($\Delta x = 1.5$ m, $\Delta x = 1.0$ m, $\Delta x = 0.5$ m), and broken stages ($\Delta x = 2.0$ m, $\Delta x = 2.5$ m). The wave in broken stage ($\Delta x = 2.0$ m, $\Delta x = 2.5$ m) exerts moderate pressures on the superstructure, approximately twice as large pressures as on deck (excluding P5). Breaking and unbroken stages of the wave ($\Delta x = 1.5$ m, $\Delta x = 1.0$ m, $\Delta x = 0.5$ m) result in pressures that reachpressures 10 times as large as what was recorded on the deck (excluding P5). The pressure peak magnitudes recorded on the vertical wall for impacts with wave in breaking and unbroken stages ($\Delta x = 1.5$ m, $\Delta x = 1.0$ m, $\Delta x = 0.5$ m) can be approximately 5 to 13 times higher than that of the wave in its broken stage ($\Delta x = 2.0$ m, $\Delta x = 2.5$ m).

The pressure distribution on the vertical wall increases from top to bottom. Regardless of the breaking stage, the largest pressures are recorded at the bottom of the superstructure on sensor P6. In the case of $\Delta x = 0.5$ m (impact of a wave in an unbroken stage), the high-pressure area does not reach high elevations on the superstructure. Pressures on higher elevations, P7 and P8, are smaller than recorded for the other two high-impact cases ($\Delta x = 1.5$ m, $\Delta x = 2.0$ m). Buchner [9] described the pressure distribution on the superstructure

of a stationary FPSO during green water events. They observed that the pressures are the largest at the bottom and decrease toward the top. He made these conclusions based on dambreak-like green water events on a stationary FPSO. The present study shows the impacts of a breaking wave on a ship with an inclined bow and forward speed. It can be concluded that these observations of pressure distribution are valid in the present study as well.

A notable distinction in loads between impacts of breaking and unbroken ($\Delta x = 1.5$ m, $\Delta x = 1.0$ m, $\Delta x = 0.5$ m), and broken stages ($\Delta x = 2.0$ m, $\Delta x = 2.5$ m) were presented. The distinction can be seen in both the forces and pressures on the superstructure. It is hypothesized, the difference could be explained by looking at the different kinds of energy contained in the wave. The wave in breaking or unbroken stage still contains its kinetic and potential energy. Upon impact, this energy is transferred to the structure causing large forces and pressures on the superstructure. During wave breaking, energy is transferred to rotational energy, and the wave loses both kinetic and potential energy. Therefore, the wave cannot exert as much load on the superstructure as in its unbroken stage. The kinetics of the wave was not studied in the present experiments. Further research has to be done to verify this theory.

A considerable variation in loads is seen for the same energy input by only a small perturbation of changing the distance of the ship's LCG with respect to the focal point of the wave. Such a variation in the loads poses a challenge in determining the maximum force for a specific sea state.

4.3. Change in speed

Besides the distance variation discussed above, experiments with three different vessel speeds were done. The different velocities are represented with the Froude number (Fr). The synchronization of different speeds needed extra attention as it had to be done in both space and time. The timing between the wave and the ship for different speeds is described in chapter 3.3.2. The aim of the timing was to create impacts with the wave in the same breaking stage for different speeds.

For each Fr, five repetitions were done. In figure 4.9 the forces for all five repetitions are presented for all three Fr. The total force development is similar in all three cases, but the maximum total force on the ship increases with increasing velocity, see figure 4.10. The force build-up on the superstructure for the lowest speed, $Fr = 0.2$, is similar to that of the impact of a wave in its broken stage ($\Delta x = 2.0$ m and $\Delta x = 2.5$ m) as presented in chapter 4.2. The impacts with the higher ship speed, $Fr = 0.4$ resemble more the impact where the wave is breaking on the bow, which is the case for $Fr = 0.3$ (used in all Δx variations).

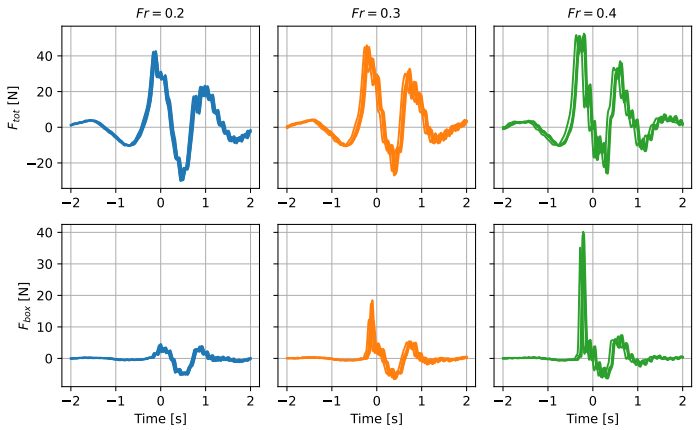

Figure 4.9: Comparison of forces of three green water events caused by the same focused, breaking wave for three different Froude number (Fr) of the ship. For the three different Fr the forces are shown for all five repeated runs. The mean surge force is subtracted from the total force.

From figure 4.10 it can be seen that higher speed results in higher forces on the whole structure, as well as on the superstructure, as we would expect. But it may be a too strong conclusion as the impacts for $Fr = 0.2$ look more like impacts with a wave in a broken stage, leaving mainly the comparison between $Fr = 0.3$ and $Fr = 0.4$.

The effects of the speed variation on the superstructure are more pronounced than on the total forces on the

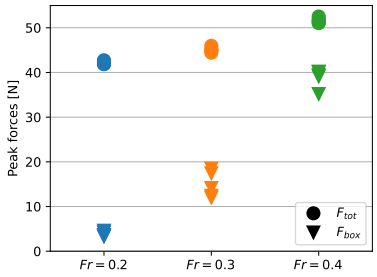

Figure 4.10: Comparison of peak forces of three green water event caused by the same focused wave for three different Froude number (Fr). For the three different Fr the peak value is shown for five repeated runs. The peak forces are displayed for the total ship (circular markers) and for the superstructure (triangular markers).

ship. Table 4.4 presents the average of the maximum forces on the ship and the superstructure for all three velocities. The change in total force from $Fr = 0.3$ to $Fr = 0.4$ is 6.5 N out of 45.13 N, a 14.4% increase. The change in forces on the superstructure is 23.71 N out of 15.06 N, a 157.4% increase. The increase of the force on the superstructure is more than can be explained solely by the different breaking stages. Therefore, the ship's forward velocity appears to have a large influence on the maximum force on a ship sailing through a breaking wave.

Table 4.4: Average of maximum total force on the ship as a whole (F_{tot}) and on the superstructure (F_{box}), and the total impulse of the impact on the superstructure (I_{box}). The average values are calculated from all five repeated runs for each different Fr.

Fr [-]	0.2	0.3	0.4
F_{tot} [N]	42.21	45.13	51.63
F_{box} [N]	3.82	15.06	38.77
I_{box} [N·s]	0.90	1.82	3.04

In conclusion, looking at the results, it is believed that increasing the speed also affects the loads. The speed increase affects the superstructure more than the global forces. Further investigation into the breaking stage of the wave during impact with different velocities is needed to draw compelling conclusions.

4.4. Different waves

As a third and final variation, three different focused, breaking waves were created, all of which resulted in a plunging breaking wave. The wave generation is described in chapter 2.3. To compare the impacts of the three waves, each wave during impact had to be in the same breaking stage. The timing between the wave and the ship was described in chapter 3.3.2. In all cases, the waves break on the bow, i.e., the wave is in a breaking stage.

Five repetitions were done for each wave. Figure 4.11 shows forces for the five repetitions for all three different waves. The total force on the ship and the forces on the superstructure are increasing with increasing wave height, as expected. The increase has a similar tendency for both the force on the ship as a whole and for the force on the superstructure as shown in figure 4.12. A similar initial spike-like force development can be observed in all three cases on the superstructure. This spike magnitude and the impulse contained in the spike are increasing with increasing wave height. The second part of the force build-down after the spike is similar for all three waves. Increasing the wave height only increases the initial spike, but the impulse contained in the rest of the impact remains approximately the same.

In conclusion, with the increase in wave height, the wave energy is increasing in the system. The forces increased with the increase of wave energy on both the ship and the superstructure. The increase in force is similar in both cases.

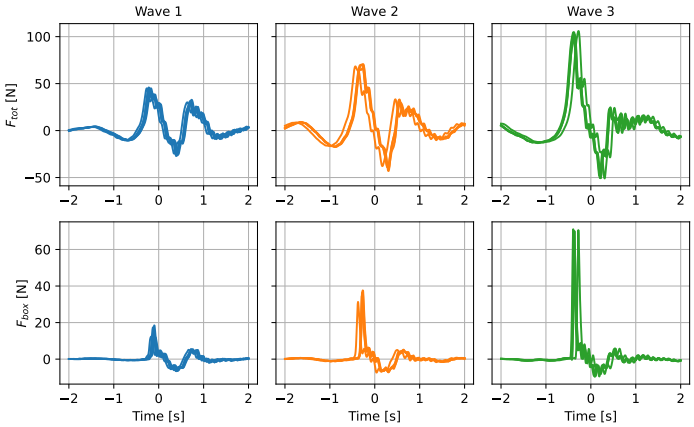

Figure 4.11: Comparison of forces of three green water events caused by three different waves. In all cases the synchronization of the wave and the ship was tuned so the wave is breaking on the bow of the ship. In each case the forces is shown for the five repeated runs. The mean surge force is subtracted from the recorded total force.

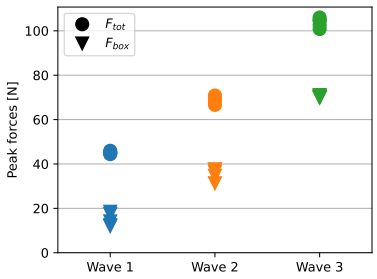

Figure 4.12: Comparison of peak forces of three green water event caused by three different waves. For the three different waves the peak value is shown for five repeated runs. The peak forces are displayed for the total ship (circular markers) and for the superstructure (triangular markers). The mean surge force is subtracted from the recorded total force.

4.5. Variability of results

The variability of the results is an important aspect to address during the experiment series, as breaking wave impacts demonstrate large variability [8, 10]. Bullock et al. [10] reported that the force and pressures have a large variability on nominally identical breaking waves on vertical walls. They found that the forces on the vertical wall vary by up to an order of magnitude, while considering the impulse on the structure smoothens out the variability. In their experiments the variability of the impulse is significantly smaller than the variability of the peak force. Bos and Wellens [8] modelled a maritime structure as a pendulum suspended above the mean free surface of a wave tank. They investigated the motion response of the pendulum under breaking waves. They found that the variability of the global motion, hence the impulse, is always, with approximately one order of magnitude, larger than the variability of the free surface elevation measured in front of the pendulum. That is, the variability of the input is amplified in the output.

In the present study, too, variability in the results is introduced by the physical process, such as the breaking of the wave and the violent flow on deck after impact. Table 4.5 shows the average value and the coefficient of variation (CV) for all different experiment series. The average value and the CV is presented for the maximum free surface elevation at the wave gauge in front of the ship ζ_{frt}, the maximum force on the ship F_{tot}, the maximum force on the superstructure F_{box}, and the impulse on the superstructure I_{box}. The surface elevation at the front wave probe is considered as an input for the wave impact, and the other values in table 4.5 are taken as output. Figure 4.13 shows the relation between the input's CV and the CV of three outputs. The linear relation between input's and output's CV is presented as well.

A general trend can be discovered between the CV for the different values. The variability of the input, the free surface elevation, is amplified by the loads on the superstructure. The highest CV is found for the maximum force on the superstructure. The CV of the impulse on the superstructure is somewhat smaller, while the

Table 4.5: Average (avg) and coefficient of variation (CV) of the maximum of the front wave gauge ζ_{frt}, the maximum force on the total ship F_{tot}, the maximum force on the superstructure F_{box}, and the impulse on the superstructure I_{box}. The data shown was calculated from all five runs in each series.

Series name	ζ_{frt}		F_{tot}		F_{box}		I_{box}	
	avg	CV	avg	CV	avg	CV	avg	CV
W1_d25_Fr03	148.73	0.0227	42.55	0.0364	3.51	0.1314	0.80	0.0625
W1_d20_Fr03	138.14	0.0163	44.38	0.0075	4.84	0.0887	0.95	0.0484
W1_d15_Fr03	118.82	0.0439	45.10	0.0110	14.88	0.1769	1.80	0.0710
W1_d10_Fr03	98.38	0.0159	45.26	0.0093	22.69	0.0469	2.20	0.0136
W1_d05_Fr03	96.10	0.0067	47.92	0.0091	23.17	0.0175	2.33	0.0092
W1_d19_Fr02	130.94	0.0160	42.21	0.0076	3.82	0.1278	0.90	0.0713
W1_d11_Fr04	110.75	0.0373	51.64	0.0102	38.77	0.0477	3.04	0.0295
W2_d20_Fr03	157.91	0.0470	69.19	0.0220	35.49	0.0659	3.38	0.0550
W3_d13_Fr03	223.96	0.0151	103.76	0.0177	70.31	0.0066	5.40	0.0284

lowest CV was found for the maximum force on the ship. The CV of the ship is even smaller than that of the incoming wave.

Looking at the size of the ship with respect to the wave could explain why the smallest CV was found for the forces on the ship as a whole. The ship is a large structure, and as the forces act along the whole length of the ship, the variability in the waves is smoothened out. On the other hand, the forces on the superstructure are a result of an instantaneous impact. The forces are dependent on the volume of water on deck, and the kinematics of the wave [9]. Both the volume of the shipped water and the dynamics of the wave are dependent on the instantaneous free surface elevation. Therefore, the force on the superstructure is dependent on an instantaneous process. The variability of the free surface elevation is amplified, causing a one order of magnitude higher CV for the forces on the superstructure than for the surface elevation. The impulse of the impact reduces the variability somewhat for the peak force on the superstructure. It is, however, still greater than the CV of the input in terms of the free surface elevation.

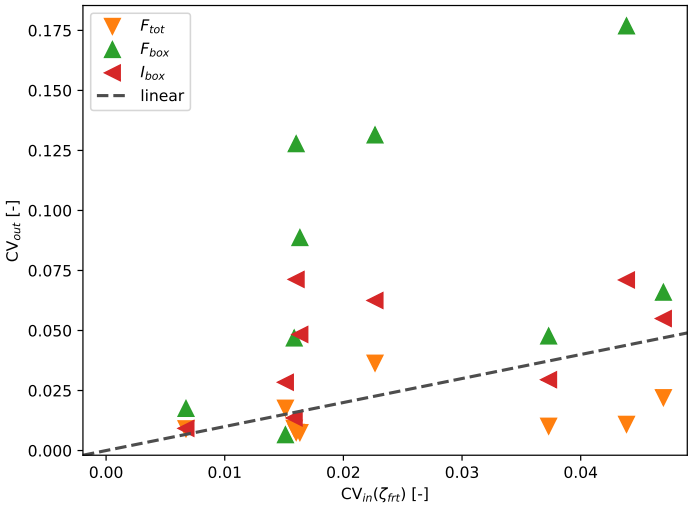

Figure 4.13: Relation between the input coefficient of variation of the front wave gauges $CV_{in}(\zeta_{frt})$, and the CV of multiple outputs. The CV_{out} is shown for the outputs of the maximum force on the total ship F_{tot}, the maximum force on the superstructure F_{box}, and the impulse on the superstructure I_{box}. The linear relation between the input $CV_{in}(\zeta_{frt})$ and the output CV_{out} is plotted with black dashed line. The shown data was calculated from all five runs in each series.

The presented characteristics of the variability are in line with the observations of Bullock et al. [10]. They found that the variance of the total impulse contained in the impact is less variable than the peak force. Bos and Wellens [8] found that the CV of the global response, hence the impulse, is one order of magnitude higher than the CV of the incoming waves. In the present research, the CV of the impulse on the superstructure is

also higher than the CV of the incoming waves. However, an order of magnitude amplification is not found.

Comparing the three articles, we may be able to explain the similarities and dissimilarities in variability. The vertical wall is fixed. The pendulum and the ship both have degrees of freedom. But consider that the ship was also held restrained in surge direction by means of its connection to the towing carriage. Both vertical wall and ship as a whole are fairly large with respect to the height of the breaking wave. These similarities between wall and ship may explain the similarities in variability in impulse, for both lower than the variability of the incoming wave. The size of the pendulum was fairly small compared to the height of the breaking wave, and so was the superstructure on the deck of the ship. The similarity in size between pendulum and superstructure may explain the similarities in variability of the impact force on pendulum and superstructure, being larger than the variability of the free surface elevation.

In conclusion, the global loads are less variable than local loads as the ship acts like a filter that reduces the variability of incoming waves, which is considered as the input. Significant variability was recorded for the peak forces on the superstructure. The integrated force, the impulse on the superstructure, is less variable than the force magnitude itself. The variability of the loads shows similar characteristics to the variability of breaking wave impacts on a fixed vertical wall. The similarity between the two experiments and, to a lesser extent, similarity in experiments with the breaking wave impacts on a pendulum can be explained with comparing the size of the structure to the wave. The ship is large compared to the wave, and the variability of the forces on the ship as a whole is smaller than the variability of the incoming waves. Whereas the superstructure is small and the variability of the forces on the superstructure is larger than the variability of the incoming waves.

4.6. Discussion of experimental results

In the chapters above, the post-processing of the experiments is described, and the results are evaluated. The post-processing was done in two steps. First, the runs for each series are synchronized so the results can be evaluated. Second, the measured signals are filtered. The experiments were conducted systematically, where the position of the ship was varied with respect to the focus point of the breaking wave at the focusing time. Using the same wave input resulted in green water events and loads on deck structure with different characteristics caused by different breaking stages of the focused wave. The effects of different ship velocities and different focused breaking waves were also explored in the experiments.

Five distance variations were done in the experiments. In all five cases, the wave was the same. However, changing the distance, the breaking stage of the wave varied during impact. A considerable variation in loads is seen for the same energy input by only a small perturbation of changing the distance of the ship's LCG with respect to the focal point of the wave. Such a variation in the loads poses a challenge in determining the maximum force for a specific sea state.

It is believed that increasing the speed also affects the loads on the ship and the superstructure. The speed increase affects the forces on the superstructure more than the global forces on the ship. However, due to the timing of the vessel, the wave during impact is in a different stage. Therefore further investigation into the breaking stage of the wave during impact with different velocities is needed to draw compelling conclusions.

Three waves with increasing wave heights were investigated. In all three cases, the wave was in a breaking stage during impact. With the increase in wave height, the wave energy is increasing in the system. The forces increased with the increase of wave energy on both the ship and the superstructure. The increase in force is similar in both cases.

The variability of the impacts was also discussed. It was discovered that the variability of the incoming waves is amplified. The variability of the forces and the impulse on the superstructure are greater than the variability of the incoming waves. However, the variability of the maximum total force on the ship was negligible. The characteristics of variability are similar to what was observed in breaking wave impacts on a fixed vertical wall but differ from breaking wave impacts on a pendulum.

5

Conclusions

Conventional green water events can lead to severe consequences on ship structure and safety. At the same time, to date, the severity of breaking wave impacts was only mentioned but not studied systematically. The present research discussed green water loads caused by breaking waves on a ship at forward speed. The goal of the research was to establish the *effects of breaking waves on the load over the front deck and superstructure of a ship at forward speed.* Two research question were formed to investigate the problem, which this thesis answers:

1. *How can the fully nonlinear problem be modeled in experimental and numerical settings?*
2. *How does the loads on the ship react to changes in the settings such as*
   (a) *changing the distance of the ship with respect to the breaking wave,*
   (b) *varying the speed of the vessel, and*
   (c) *using different waves.*

Breaking waves and their propagation are nonlinear processes. Therefore the main focus in answering the first research question was on creating breaking waves. Two methods were implemented. First, a numerical investigation was done on creating focused waves with prescribed characteristics. The goal was to create a focused wave at a predetermined time and location in a 2D numerical wave basin. The nonlinear interaction between the wave components caused the focused wave to shift both in time and location from the prescribed time and location. Corrections with third-order theory and iterative methods with component phase and amplitude corrections were tried. However, no convergence to the target function was found. It was shown that the leading wave reached a higher amplitude in a numerical environment than the focused wave. Therefore, making this method unsuitable for creating breaking waves in a numerical setting.
After concluding that using the first method will not lead to breaking waves, another option was implemented. Breaking waves were recreated from literature and created originally with heuristic methods in a physical wave tank. Three waves were created in this manner. The characteristics of the waves, such as their focusing location and time, were investigated with numerical simulations. The spectrum of each wave and its parameters, such as significant wave height and peak period, were retrieved from the simulations as well.

Novel experiments were conducted investigating focused breaking wave interaction with a ship at forward speed to answer the second research question. Systematic experiments, in which the ship was sailing through the breaking wave, varied the location of the ship's LCG with respect to the focal point of the wave at the focusing time. Variations in ship speed and different focused breaking wave heights were also investigated.
Distance variation — First, the ship was sailed through a breaking wave where the position of the LCG of the ship was changed with respect to the theoretical focus point of the wave at the focusing time. Five positions were investigated, one where the wave brakes on the bow of the ship, two where the wave is already broken, and two where the wave is not yet broken. In all five positions, the wave was the same; therefore, the wavemaker's energy input was identical during all five series. In changing the position of the ship's LCG with respect to the focus point of the wave at the focusing time, significant variations were found in load magnitude and development for the same wave energy input.Loads of wave impacts in a broken stage are

characteristically different from the impacts caused by the wave in its breaking or unbroken stage. Forces on the superstructure are high and spike-like for impacts with the wave in an unbroken stage. The lowest forces were found for impacts of the wave in a broken stage. High, peak-like pressures are recorded on the superstructure when the wave is in its unbroken stage. In contrast, the development of the pressure has a longer duration, and the magnitude is smaller for impacts of the wave in a broken stage. Potentially the maximum force on the superstructure was recorded for impacts with the wave in the unbroken stage. The results of the study are a step towards establishing the highest possible green water loads for a given sea-state. For the same energy input, the magnitude and development of the pressures change with the stage of the breaking wave, which makes the determination of the maximum loads for a particular sea state challenging.
Change in speed — A preliminary conclusion seems to be that the forces on the ship and the superstructure are increasing with the increase of the ship's forward speed. This is as expected, but more investigation is required to quantify the effect. The variation in speed has more significant effects for the load of the local structure on deck than for the global forces on the ship as a whole.
Different waves — The ship's interaction with three different focused, breaking waves with increasing wave height were studied. In all cases, the wave was in a breaking stage during impact. With increasing wave height, the wave energy increases in the system. As expected, more energy leads to increased forces on both the ship and the superstructure. Increasing the wave energy has similar effects on the change of total force on the ship and on the force on the superstructure.

Other aspects were investigated in the research such as the variability of the impacts and compared with literature. The coefficient of variation (CV) of the impact on the superstructure is amplified with respect to the CV of the incoming waves. On the other hand, the variability of the maximum force on the ship as a whole is smaller compared to the incoming wave's variability. Both the CV of the maximum force and impulse on the superstructure are greater than that of the incoming wave. The variability of the impulse is smaller than the CV of the maximum force. These results are similar to breaking wave impacts on a vertical wall and to a lesser extent to the breaking wave impact on a pendulum. The similarity between the present study and the breaking wave impacts on a fixed structure is explained by the size of the structure with respect to the height of the breaking wave.

6

Recommendations

In this chapter, suggestions are made for future work. The recommendations are divided into two parts. First recommended research in a breaking wave caused green water events are proposed, then practical recommendations for experiments are presented.

- One of the difficulties encountered during the experiments was to create an accurate timing procedure between the ship and the wave. This has practical and theoretical roots. There needs to be a clear definition of when the wave is breaking for a good timing procedure. This needs to be defined beforehand for a better timing application, and the timing can be adapted to the definition. This will help in the comparison of different waves and speed variations.
- A better comparison method needs to be created to understand further how the ship's speed and different waves affect the loads. It is suggested that the distance variation of the ship to the wave is to be investigated with different waves as well as with different speeds. This way, the correct impacts, which result from different stages of the wave breaking, can be compared with each other.
- The investigated waves all had a larger wavelength than the ship. During the impact, the ship was climbing up on the wave before the impact, and out-of-phase motions were not covered in this research. The combination of larger ships or shorter waves is recommended in future research so the effects of the out-of-phase motions can be understood.
- An important aspect of the researched phenomena was only mentioned in this research: the probability of occurrence. It is essential to know what are the chances of a ship encountering a breaking wave during its voyage. It is recommended that research is done on the probability of such wave encounters, so ships can be designed accordingly.

Based on the experience during the experiments, recommendations are made for future setups for investigating loads of a breaking wave impact on a ship with forward speed:

- During the experiments, the timing of the carriage startup relied on human involvement, which inherently introduces errors to the experiments. It is recommended for further experiments to automate the timing between the wavemaker motions and the carriage motions. Automation will improve the repeatability of the experiments. It is also recommended to measure the timing signals, which will help in the synchronization of the data sets during post-processing.
- Due to the violent flow, high pressure, and large accelerations during impact, water got into places where it was not expected. The violent flow during impact overshot the protective barrier/breakwater, and water got into the hull of the ship. High pressures pushed water into small gaps, while accelerations and the motion of the ship made water residing in the bottom of the hull reach electrical equipment. Force sensors and pressure sensors became wet, and their signal unreliable.
  It is recommended to take extra care during the design of the setup so no water can get to electrical equipment or to use waterproof transducers.
- When determining the RAO of the ship, it is recommended to include the resonance frequency taking into account the forward speed of the vessel.

- In the force measurements, the natural frequency of the model is visible, which hinders the acquired data. Due to the impact loads during a breaking wave impact, the force sensor's resonance and setup need to be taken into account. There is a trade-off to be made between the accuracy and the resonance of the sensor. This needs careful evaluation before experiment setup.
- A good research facility where further research is done on the topic should provide solutions for the above-listed problems. The facility be able to provide
  - reliable wave generation even with short waves, or
  - ability to run experiments with larger ship model,
  - the (automatic) operation of both the wavemaker and the carriage from the same location, and
  - a synchronized data acquisition system of stationary measurement and measurements on the moving carriage.

A

ComFLOW

For numerical simulations, ComFLOW is used. ComFLOW is a numerical method that is based on the Navier-Stokes equation and can simulate fluid flow with free surface [40]. The solver is based on the finite volume discretization method. To resolve the free surface Volume of Fluids (VOF) method is used. ComFLOW has been successfully implemented to simulate run-up, breaking wave, and green water events [29]. Here only a short introduction will be made to the numerical tool. Full and detailed description can be found in the online documentation [40] and in the thesis of Kleefsman [34].

A.1. Governing equations

ComFLOW solves the three dimensional fluid flow which can be described by the continuity equation and the Navier-Stokes equation. For water, which is an incompressible Newtonian fluid, the equations are written in general form as

$$\nabla \cdot \mathbf{u} = 0 \tag{A.1}$$

$$\frac{\partial \mathbf{u}}{\partial t} + \mathbf{u} \cdot \nabla \mathbf{u} = -\frac{1}{\rho} \nabla p + \frac{\mu}{\rho} \nabla \cdot \nabla \mathbf{u} + \mathbf{F} \tag{A.2}$$

where t is time, $\mathbf{u} = (u, v, w)$ is the three dimensional velocity vector in x, y, and z direction, ρ is the density, p is the pressure, μ is the dynamic viscosity, and $\mathbf{F} = (F_x, F_y, F_z)$ is the external body force vector which in the present case reduces to gravity force. The continuity (A.1) and the Navier-Stokes (A.2) equation are describing mass and momentum conservation respectively. The equations are defined and solved in the three-dimensional domain Ω which has the boundary of $\partial\Omega$.

A.2. Boundary conditions and free surface

For solving the Navier-Stokes equations boundary conditions are needed. At solid boundaries, no fluid can go through the boundary and that the fluid sticks to the wall because of viscous effects. Therefore the velocity at solid boundaries is $\mathbf{u} = \mathbf{u}_w$, where $\mathbf{u}_w$ is the velocity of the solid boundary.

The evolution of the free surface is determined with the following equation:

$$\frac{Ds}{Dt} = \frac{\partial s}{\partial t} + (\mathbf{u} \cdot \nabla) s = 0 \tag{A.3}$$

where the free surface position is given as $s(\mathbf{x}, t) = 0$. Boundary conditions at the free surface are also defined for pressures and velocities. The continuity of the normal and tangential stresses are defined with the following equations:

$$-p + 2\mu \frac{\partial u_n}{\partial n} = -p_0 + \sigma\kappa \tag{A.4}$$

$$\mu \left(\frac{\partial u_n}{\partial t} + \frac{\partial u_t}{\partial n} \right) = 0 \tag{A.5}$$

Here u_n and u_t are the normal- and tangential component of the velocity at the free surface, p_0 is the atmospheric pressure, σ is the surface tension, and $2H$ represents the total curvature.

A.3. Numerical model

To solve the mathematical model the equations are discretized in space and time. The simulation domain σ is covered with a Cartesian staggered grid where the equations are solved. The variables and pressures are defined in the cell centers while the velocities on the cell boundaries.

Complex geometries can be represented in the Cartesian grid, therefore, cells can assume different character. To represent the different characters edge and volume apertures are introduced which are responsible for tracking which part of a cell is open to fluid flow. Moreover, the Volume of Fluid (VOF) function is introduced, which represents the fraction of the cell which is filled with fluid. Depending of the values of the VOF function and the apertures, each cell is categorized as boundary (B), empty (E), surface (S), and fluid (F) cells. In figure A.1 an example is given which shows how the ComFLOW labeling works based on the VOF function.

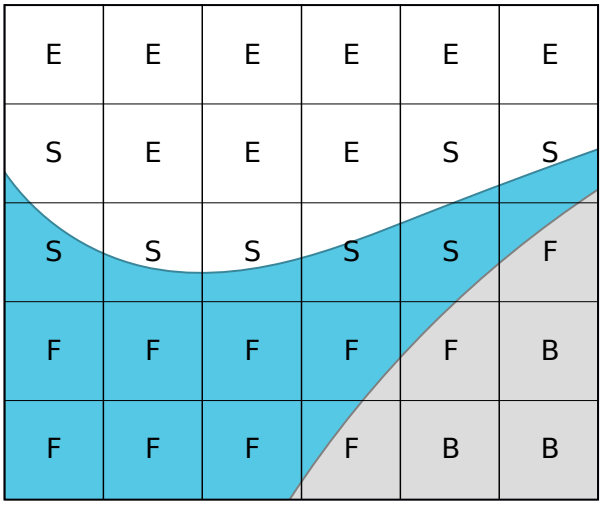

Figure A.1: Illustration of the labeling system of the Cartesian staggered grid in ComFLOW to distinguish different cell categories. The boundary B cells define solid wall, E cells are empty, F cells are occupied with fluid and S cells contain the free surface.

The nonlinear convection term can be modelled using different discretization. The solver can implement first and second order upwind, and second order central discretized. Using central discretization scheme a mod-min flux limiter can be used as well. Central discretization is more accurate than first order upwind scheme, and introduces less artificial diffusion in the simulation [34]. On the other hand, central discretization is less stable compared with upwind schemes. However, applying flux limiter increases stability but also introduces artificial diffusion.

A.3.1. Time step control

The discretization in time is done with a forward Adams-Bashforth method, leading to second-order accuracy. The time step is controlled by the CourantFriedrichsLewy (CFL) condition. The CFL number is calculated as

$$CFL = \max_{i,j,k}\left(\frac{|u_{ijk}|\delta t}{h_{x,i}} + \frac{|v_{ijk}|\delta t}{h_{y,j}} + \frac{|w_{ijk}|\delta t}{h_{z,k}}\right) \tag{A.6}$$

where u, v, w are the velocity components, and h_x, h_y, h_z are the mesh size in the corresponding direction. The CFL condition is set to $0.4 < CFL < 0.85$ which ensures that information in a cell can only travel to a neighbouring cell in a time step.

B

Lines plane of the DSDS model nr. 523

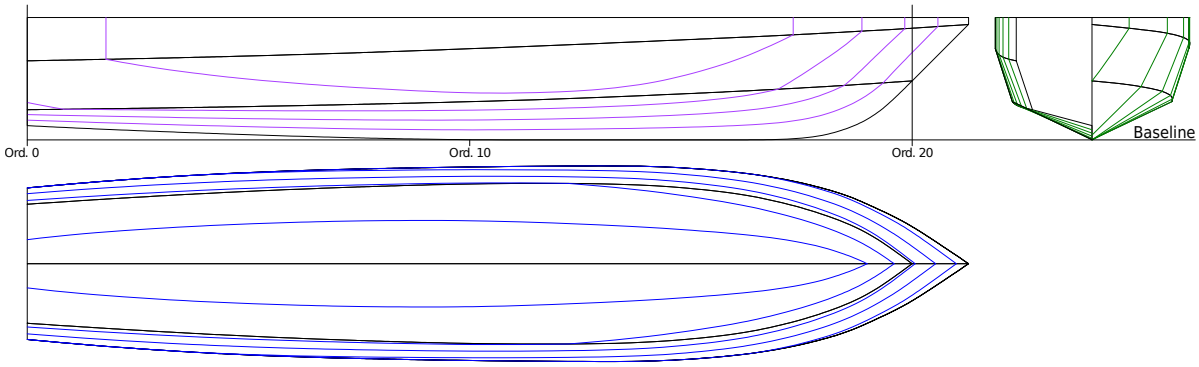

Model nr. 523		
Beta:	25.00	[deg]
Lp:	1.50	[m]
Cap:	47.5	[%Lp]
Lp/Bpx:	5.50	[-]

Figure B.1: Lines plane of the DSDS model nr. 523. The lines plan is retreived from the open access database of the DSDS series http://dsds.tudelft.nl [30]

C

Dimensions of experimental setup

The experimental setup was described in chapter 3.2. The lines plane of the model is shown in appendix B. In this appendix, the dimensions of the built superstructure and the placement of the sensors are shown. Figure C.1 shows the relative position of the wave probes with respect to the ship. The dimensions of the superstructure and its placement on the ship are shown in C.2. The arrangement of the pressure sensors on the bow is shown in figure C.3. The figure shows the placement of the wetness sensors as well.

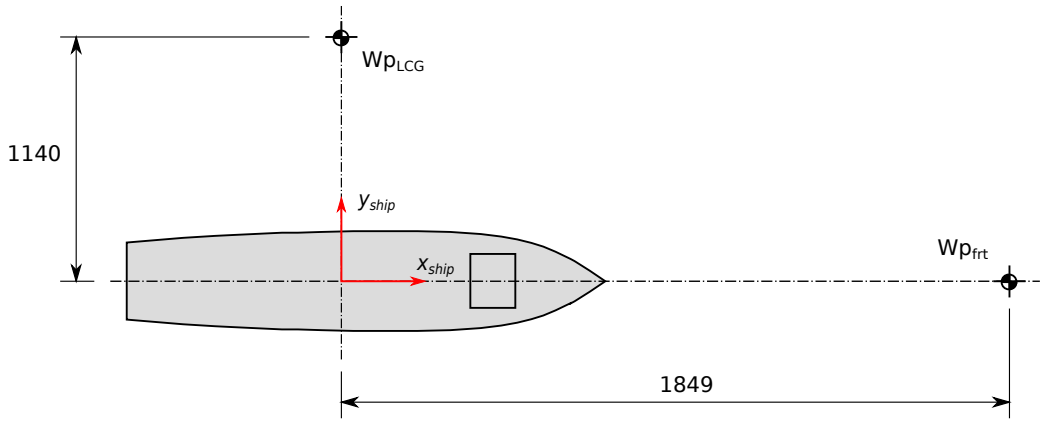

Figure C.1: Placement of the wave probes at the side (Wp_{LCG}) and in front (Wp_{frt}) of the ship. All dimensions are in mm (not to scale).

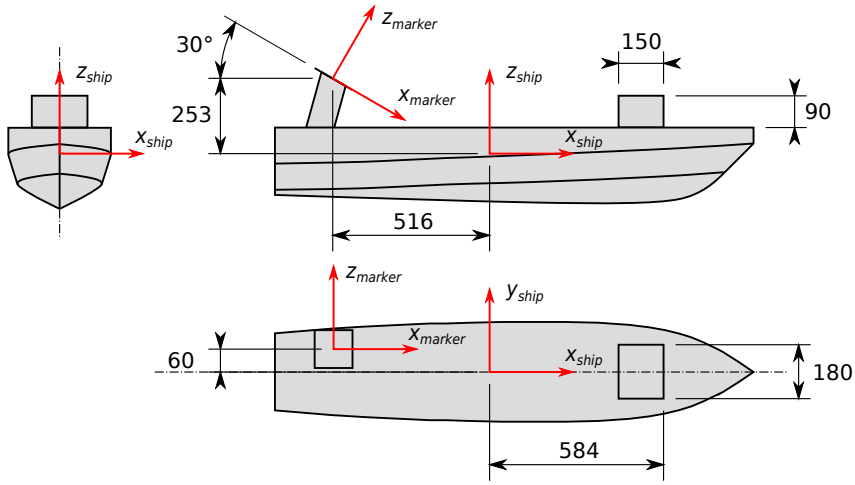

Figure C.2: Dimensions of the built superstructure and the position of the marker plate. All dimensions are in mm (not to scale).

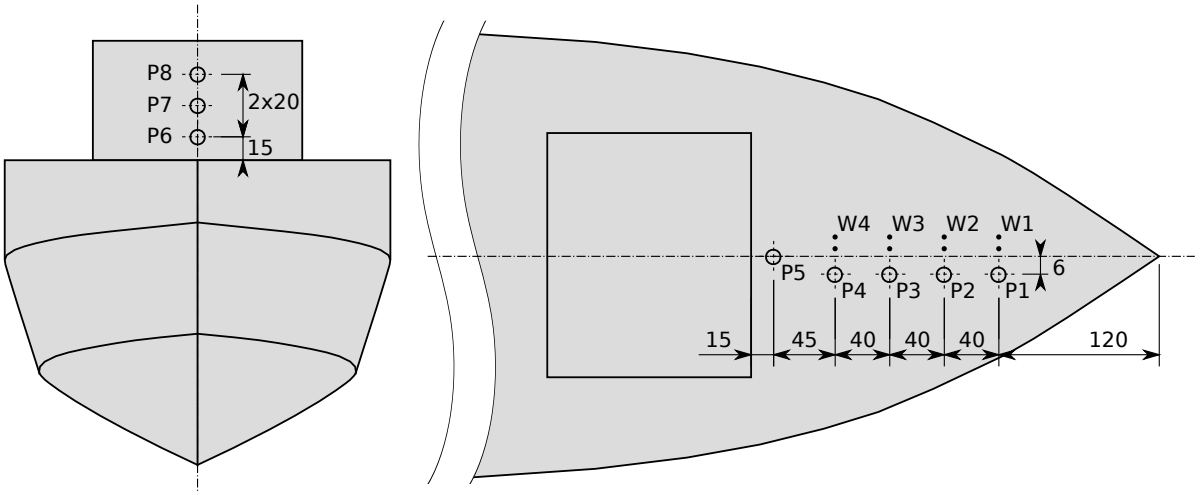

Figure C.3: Placement of the pressure sensors and water probes on the front deck and superstructure. On the left figure, the front view of the ship with the superstructure can be seen. The right figure shows the bow section of the ship in top view. All dimensions are in mm (not to scale).

D

Comments on experiments

D.1. Malfunction of sensors

For each experimental condition, five repetitions were made to have a statistical data set for each scenario. Although care was taken to seal the deck and prevent water from reaching sensors, some sensors did get wet. Wet sensors resulted in sensor malfunction and erroneous results. Such was the case for the force sensors and some pressure sensors. In case of force sensor failure, the run was repeated to have all five repetitions. However, pressure sensor failure could not permanently be fixed due to lack of time. Therefore, some of the pressure signals had to be excluded from further post-processing. A list of the excluded signals is shown in table D.1.

Table D.1: Summary of pressure sensor failure for series or runs in failures. In all cases pressure sensor P3 was faulty, which is not indicated separately for all runs.

Series name	Comments
W1_d25_Fr03	Runs are good
W1_d20_Fr03	P2 pressure signal is unreliable for the series
W1_d15_Fr03	P2 pressure signal is unreliable for the series
W1_d10_Fr03	P1 and P2 pressure signals are unreliable for the series
W1_d05_Fr03	P1 and P2 pressure signals are unreliable for the series
W1_d19_Fr02	Pressures are not reliable for series
W1_d11_Fr04	Pressures are not reliable for series
W2_d20_Fr03	Pressure sensors are good
W3_d13_Fr03	Pressure measurements are not available for Run nr. 331 and 333

D.2. Motion sensor

The motion response was recorded with the Optotrak Certus system as described in chapter 3.2. A stereo camera system was fixed to the carriage, and a marker plate was placed on the ship with LEDs. The camera tracked the motion of the marker plate, reconstructing the motion of the ship.

An error was discovered in the calibration of the tracking system during the post-processing of the data. The Certus motion tracing system was calibrated before experiments. The calibration process involved describing the position of the marker plate with respect to the ship's CoG. During the calibration, the longitudinal position of the marker plate was given with the wrong sign. Therefore the recorded signals were corrected in the post-processing. The corrected heave motion is calculated as

$$\xi_3 = \xi_{3,measured} - 2 \cdot a \cdot \sin(\xi_5) \tag{D.1}$$

where $\xi_{3,measured}$ is the measured heave motion with the wrong calibration, $a = 516$ mm is the longitudinal distance between the ship's CoG and the center of the marker plate (see Fig. C.2), and ξ_5 is the pitch response

of the model.

In some cases, the combination of the spraying water and the ship's motions were unfavorable, and the camera could not detect the marker plate placed on the ship. In these cases, the motion data is only partial and reported only when the signal is complete. A significant part of motion data is missing for the experiments with the two higher waves, Wave 2 (W2_p20_Fr03) and Wave 3 (W3_p13_Fr03), where the motions of the ship are the largest.

E

Synchronization values of runs

The synchronization procedure for the runs is described in chapter 4.1.1. The procedure relies on the initial location x_{ini}, the prescribed location of the ship's LCG at the focusing time $x(t = t_{focus}) = x_{focus} + \Delta x$, and the position trace of the carriage $s(t)$. Based on these the focusing time t_{focus} is calculated. The initial position of the ship's LCG and the focusing time are presented in table 4.1 for all five repetition in the nine series.

Table E.1: The focusing time of the wave and initial position of the ship's LCG for different runs.

Series name	Run Nr.	x_{ini} [m]	t_{focus} [s]
W1_d25_Fr03	709	73.362	75.89
	730	73.328	78.84
	732	73.324	79.12
	734	73.322	79.28
	812	73.312	74.52
W1_d20_Fr03	707	73.364	80.30
	722	73.342	81.14
	724	73.338	75.90
	726	73.334	75.48
	728	73.330	78.72
W1_d15_Fr03	705	73.369	76.10
	713	73.355	75.88
	715	73.352	75.86
	718	73.349	74.02
	720	73.344	75.40
W1_d10_Fr03	711	73.358	75.88
	905	73.274	75.27
	909	73.267	74.16
	921	73.249	73.10
	923	73.246	75.85
W1_d05_Fr03	911	73.264	73.85
	913	73.261	72.01
	915	73.258	72.95
	917	73.256	72.67
	919	73.255	71.50
⋮	⋮	⋮	⋮

Series name	Run Nr.	x_{ini} [m]	t_{focus} [s]
⋮	⋮	⋮	⋮
W1_d19_Fr02	103	73.239	79.41
	105	73.235	75.60
	107	73.231	75.46
	111	73.229	77.89
	113	73.225	77.68
W1_d11_Fr04	115	73.225	70.15
	117	73.221	73.08
	119	73.221	72.50
	121	73.216	73.91
	123	73.214	75.34
W2_d20_Fr03	311	73.163	71.76
	313	73.161	74.34
	315	73.159	75.38
	317	73.157	73.78
	319	73.156	74.89
W3_d13_Fr03	325	73.150	73.86
	327	73.149	75.70
	329	73.148	75.86
	331	73.145	73.46
	333	73.144	76.24

F

Motions

The general development of a green water event is similar in all cases. First, the ship climbs the wave until the wave becomes steep, and the ship cannot follow the slope of the wave, resulting in the bow submerging in the wave. The wave comes on deck resulting in an impact on the superstructure. The first green water event happens. After the first impact, the ship comes out of the wave and plunges back to the wave trough with a forward pitch. Here the bow submerges again, and a more conventional dam-break-like green water event happens as water comes on deck again.

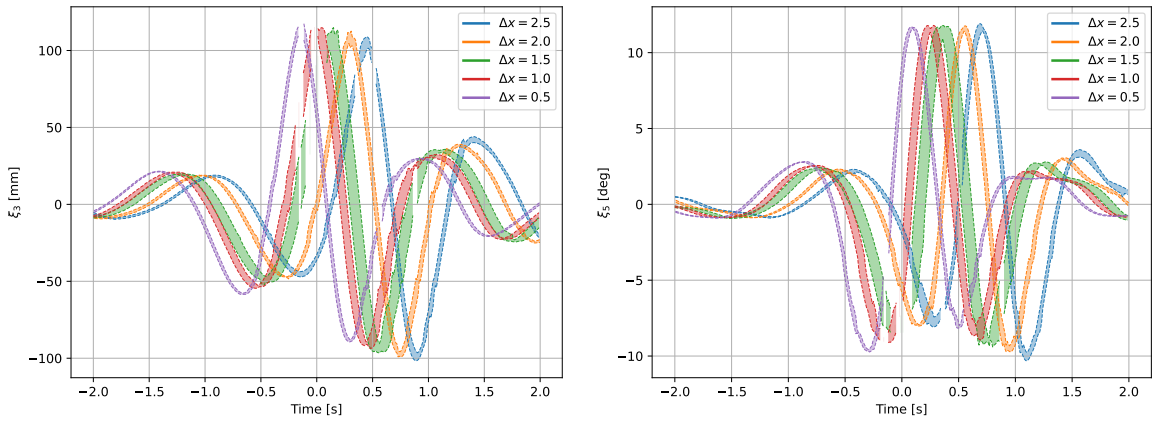

(a) Heave response

(b) Pitch response

Figure F.1: Comparison of heave and pitch motion response of the ship for five different green water events. The breaking wave is the same in all cases (Wave 1), while the ship position is varied with Δx to the breaking wave at the time of breaking. In each case, the time development of the envelope of the maximum and minimum values are shown for the five repetition. In periods when error is registered in the optical motion sensor due to spraying water and large motions, the data is not shown resulting in discontinuous motion representation.

In figure F.1 the comparison of the pitch and heave motions can be seen for cases where Δx was changed. Δx represents the distance of the ships LCG to the focusing location of the focused wave at the focusing time. Looking at the motion response, it can be seen that there is hardly any change in the maximum positive, forward pitch angle. In contrast, the maximum backward pitch varies with the distance (see figure F.1b). The maximum forward pitch happens after the impact when the ship plunges back to the trough. The maximum negative backward pitch angle is the lowest in the case where the wave is already broken, with a position shift of $\Delta x = 2.5$ m (series W1_d25_Fr03). When the ship climbs the wave in its unbroken stage ($\Delta x = 2.5$ m), the backward pitch angle is the highest. On the other hand, when the wave is already broken ($\Delta x = 0.5$ m), the pitch angle is the smallest.

In figure F.2 the comparison of motion response, when the ship velocity is varied, can be seen. Looking at the motions response under different velocities, it can be seen that the maximum forward pitch angle decreases

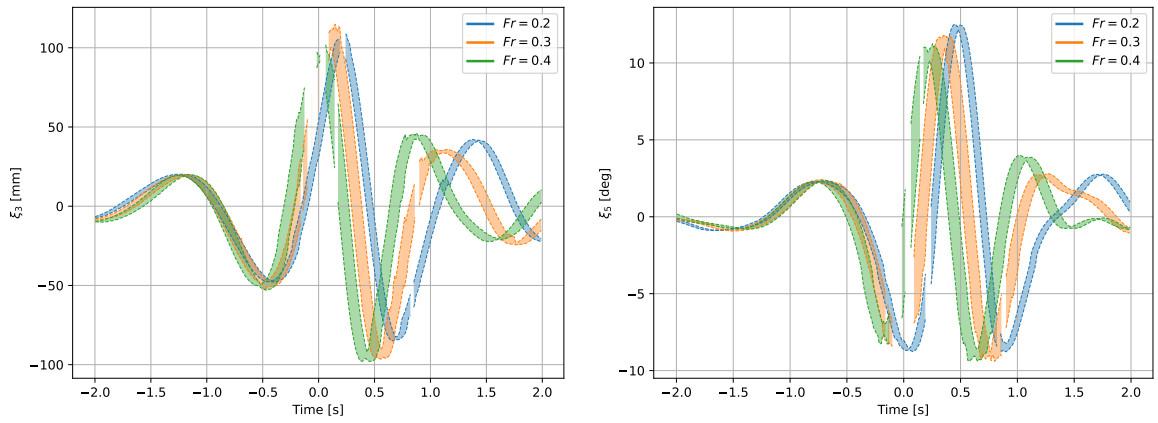

(a) Heave response

(b) Pitch response

Figure F.2: Comparison of heave and pitch motion response of the ship for three different ship velocity. In each case, the time development of the envelope of the maximum and minimum values are shown for the five repetition. In periods when error is registered in the optical motion sensor due to spraying water and large motions, the data is not shown resulting in discontinuous motion representation.

with the increase of ship speed. As discussed in chapter 4.3, due to timing, the comparison is not perfect and the wave is in a slightly different breaking stage during the impacts. The encountered wave is the same, but the maximum heave motion is still smallest in the case of higher speed $Fr = 0.4$. The found behaviour is similar to the "tunneling" phenomenon, which was reported by Bennett et al. [6], as a ship under high-speed sails through a focused wave without having significant pitch motion. They found that the maximum pitch angle decreases with the higher speeds while the heave motion increases. The authors concluded that the amount of water increases with the rise in the velocity of the ship and dampens out the pitch motion. It is theorized that as opposed to the water on deck would influence the pitch motion, there are inertial effects in play in this phenomenon. As the ship speed increases there is smaller time for the ship to respond to the changes in free surface elevation, therefore, leading to a smaller maximum pitch motions.

This change in motions with the change of speed could affects the loads on the ship. With higher speed the pitch is smaller during impact. The smaller pitch motion (and the smaller heave motion) increases the relative wave height which results in higher volume of water on deck.

With the highest wave (Wave 3), there is an additional movement on the motion response at ≈0.75s when compared to the wave probe signal at the LCG. This indicates a nonlinear motion response. This phenomenon can also be observed for impacts with Wave 1 and Wave 2, but it is the most dominant with the highest wave impact, Wave 3. The impact happens earlier than the extra motion, at ≈-0.25s and the wetness sensor only detects water on deck for a short period during impact. The second impact happens after ≈0.25s which can be seen in both the wetness and the pressure signals. However, neither the first nor the second impact explains the nonlinear motion response which is present in the heave, and more dominantly in the pitch motion. This motion can be explained with the rapid change in the wetted surface, and wetted waterplane area while sailing through a breaking wave. As the bow plunges back to the water it changes the waterplane area, therefore the restoring coefficient varies largely for both heave and pitch motion. While the bow falling back to the wave trough the wetted surface increases rapidly, resulting in additional movements as compared to the free surface elevation. The wave elevation at the LCG and the nonlinear motion response of the ship can be seen in figure F.3.

Significant drop can be observed in both Bow and LCG acceleration for all the runs after an acceleration peak. This happens just before the wetness sensors get wet for a second time which indicates it is at the time when the ship falls back to the water after it experiences the first breaking wave event. This phenomenon is the most significant with the highest wave (W3_d15_Fr03 series) which can be seen in figure F.3

Nonlinear behavior in the motions was observed in all cases. Most significant is the reduction in pitch motion with the increasing ship's velocity. The reduction in motion is assumed to be from inertial effects and affects the green water loads. Nonlinear motion behavior is identified after the wave impact when the ship comes out of the wave crest and plunges back to the trough. The behavior is caused by the large change in wetted area of the ship but does not affect the green water loads.

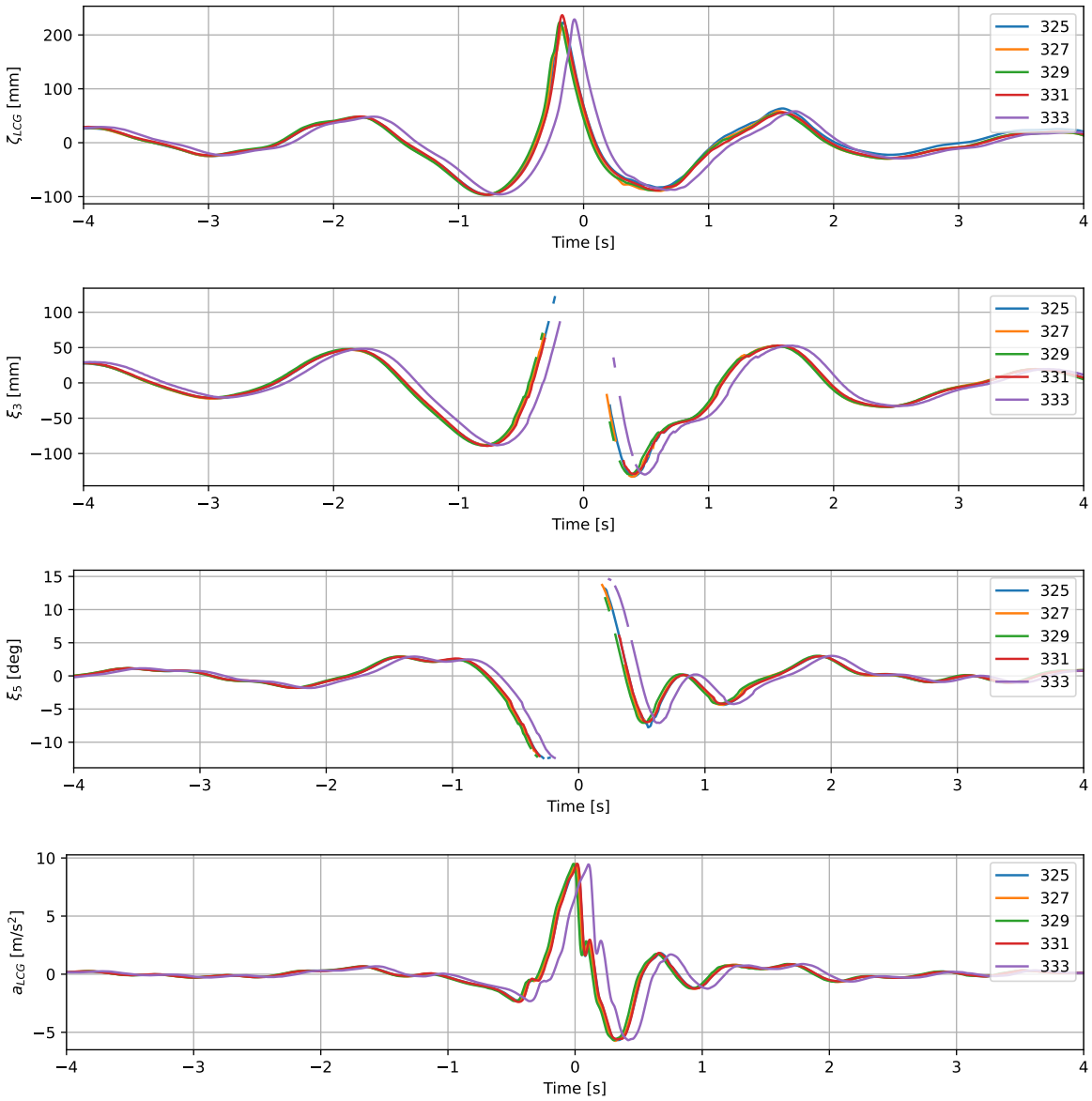

Figure F.3: Free surface elevation at LCG (ζ_{LCG}), heave (ξ_3) and pitch (ξ_5) motion response, and vertical acceleration at the LCG (a_{LCG}) of the ship for impact with the highest wave, Wave 3 (W3_p00_Fr03 series). All five repetition of the nominally identical event is presented. In periods when error is registered in the optical motion sensor due to spraying water and large motions, the data is not shown resulting in discontinuous motion representation of heave (ξ_3) and pitch (ξ_5)

Bibliography

[1] Mayilvahanan Alagan Chella, Hans Bihs, and Dag Myrhaug. Wave impact pressure and kinematics due to breaking wave impingement on a monopile. *Journal of Fluids and Structures*, 86:94–123, 2019. ISSN 10958622. doi: 10.1016/j.jfluidstructs.2019.01.016. URL https://doi.org/10.1016/j.jfluidstructs.2019.01.016.

[2] Omar S. Areu-Rangel, Jassiel V. Hernández-Fontes, Rodolfo Silva, Paulo T.T. Esperança, and Jaime Klapp. Green water loads using the wet dam-break method and SPH. *Ocean Engineering*, 219(November 2020), 2021. ISSN 00298018. doi: 10.1016/j.oceaneng.2020.108392.

[3] Kudupudi Ravindra Babu, Sri Vinay Krishna Rayudu Nelli, Anirban Bhattacharyya, and Ranadev Datta. Experimental and Numerical Investigation of Green Water Occurrence for KRISO Container Ship. *Journal of Ship Research*, 00(0):1–19, 2020. ISSN 0022-4502. doi: 10.5957/josr.08200049.

[4] Henry Bandringa, Joop A. Helder, and Sanne van Essen. On the validity of CFD for simulating extreme green water loads on ocean-going vessels. *Proceedings of the International Conference on Offshore Mechanics and Arctic Engineering - OMAE*, 1, 2020. doi: 10.1115/OMAE2020-18290.

[5] Marco Barcellona, Maurizio Landrini, Marilena Greco, and O. M. Faltinsen. An experimental investigation on bow water shipping. *Journal of Ship Research*, 47(4):327–346, 2003. ISSN 00224502. doi: 10.5957/jsr.2003.47.4.327.

[6] S. S. Bennett, D. A. Hudson, and P. Temarel. The influence of forward speed on ship motions in abnormal waves: Experimental measurements and numerical predictions. *Journal of Fluids and Structures*, 39: 154–172, 2013. ISSN 10958622. doi: 10.1016/j.jfluidstructs.2013.01.006.

[7] E.M. Bitner-Gregersen and O. Gramstad. Rogue waves. Impact on ship and offshore structures. *DNV GL R&I Position Paper*, pages 1–60, 2016.

[8] R W Bos and P R Wellens. Fluid structure interaction between a pendulum and focused breaking waves Fluid structure interaction between a pendulum and focused breaking waves. *Physics Fluids 33*, 062118 (April), 2021. doi: 10.1063/5.0054426.

[9] B Buchner. Green Water on Ship-type Offshore Structures. *PhD Thesis, Faculty of Mechanical Maritime and Materials Engineering, Delft University of Technology*, 2002. URL http://resolver.tudelft.nl/uuid:f0c0bd67-d52a-4b79-8451-1279629a5b80.

[10] G. N. Bullock, C. Obhrai, D. H. Peregrine, and H. Bredmose. Violent breaking wave impacts. Part 1: Results from large-scale regular wave tests on vertical and sloping walls. *Coastal Engineering*, 54(8):602–617, 2007. ISSN 03783839. doi: 10.1016/j.coastaleng.2006.12.002.

[11] A. Chabchoub, N. P. Hoffmann, and N. Akhmediev. Rogue wave observation in a water wave tank. *Physical Review Letters*, 106(20):2–5, 2011. ISSN 00319007. doi: 10.1103/PhysRevLett.106.204502.

[12] Lifen Chen, Paul H. Taylor, Scott Draper, and Hugh Wolgamot. 3-D numerical modelling of greenwater loading on fixed ship-shaped FPSOs. *Journal of Fluids and Structures*, 84:283–301, 2019. ISSN 10958622. doi: 10.1016/j.jfluidstructs.2018.11.003. URL https://doi.org/10.1016/j.jfluidstructs.2018.11.003.

[13] Linfeng Chen, Yitao Wang, Xueliang Wang, and Xueshen Cao. 3D numerical simulations of greenwater impact on forward-speed wigley hull using open source codes. *Journal of Marine Science and Engineering*, 8(5), 2020. ISSN 20771312. doi: 10.3390/JMSE8050327.

[14] G. F. Clauss and M. Klein. The New Year Wave in a seakeeping basin: Generation, propagation, kinematics and dynamics. *Ocean Engineering*, 38(14-15):1624–1639, 2011. ISSN 00298018. doi: 10.1016/j.oceaneng.2011.07.022.

[15] G F Clauss, F Stempinski, and M Klein. Experimental and numerical analysis of steep wave groups. In *Maritime Industry, Ocean Engineering and Coastal Resources - Proceedings of the 12th International Congress of the International Maritime Association of the Mediterranean, IMAM 2007*, volume 2, pages 693–700, 2008.

[16] Guenther F. Clauss and Ulrich Steinhagen. Optimization of transient design waves in random sea. *Proceedings of the International Offshore and Polar Engineering Conference*, 3:229–236, 2000.

[17] Günther F. Clauss, Christian E. Schmittner, and Marco Klein. Generation of rogue waves with predefined steepness. *Proceedings of the International Conference on Offshore Mechanics and Arctic Engineering - OMAE*, 2006(March 2015), 2006. doi: 10.1115/OMAE2006-92272.

[18] E. Cumberbatch. The impact of a water wedge on a wall. *Journal of Fluid Mechanics*, 7(3):353–374, 1960. ISSN 14697645. doi: 10.1017/S002211206000013X.

[19] Kristian Dysthe, Harald E. Krogstad, and Peter Müller. Oceanic rogue waves. *Annual Review of Fluid Mechanics*, 40(January):287–310, 2008. ISSN 00664189. doi: 10.1146/annurev.fluid.40.111406.102203.

[20] H. Fernández, V. Sriram, S. Schimmels, and H. Oumeraci. Extreme wave generation using self correcting method - revisited. *Coastal Engineering*, 93:15–31, 2014. ISSN 03783839. doi: 10.1016/j.coastaleng.2014.07.003. URL http://dx.doi.org/10.1016/j.coastaleng.2014.07.003.

[21] Inno Gatin, Vuko Vukčević, Hrvoje Jasak, Jeonghwa Seo, and Shin Hyung Rhee. CFD verification and validation of green sea loads. *Ocean Engineering*, 148(August 2017):500–515, 2018. ISSN 00298018. doi: 10.1016/j.oceaneng.2017.10.026.

[22] M. Greco, O. M. Faltinsen, and M. Landrini. Shipping of water on a two-dimensional structure. *Journal of Fluid Mechanics*, 525(June 2003):309–332, 2005. ISSN 00221120. doi: 10.1017/S0022112004002691.

[23] M. Greco, G. Colicchio, and O. M. Faltinsen. Shipping of water on a two-dimensional structure. Part 2. *Journal of Fluid Mechanics*, 581:371–399, 2007. ISSN 00221120. doi: 10.1017/S002211200700568X.

[24] M. Greco, B. Bouscasse, and C. Lugni. 3-D seakeeping analysis with water on deck and slamming. Part 2: Experiments and physical investigation. *Journal of Fluids and Structures*, 33:148–179, 2012. ISSN 08899746. doi: 10.1016/j.jfluidstructs.2012.05.009. URL http://dx.doi.org/10.1016/j.jfluidstructs.2012.05.009.

[25] Marilena Greco. A Two-dimensional Study of Green-Water Loading. *PhD Thesis, Department of Marine Hydrodynamics, Norwegian University of Science and Technology*, 2001.

[26] Jassiel V. Hernández-Fontes, Paulo de Tarso T. Esperança, Juan F.Bárcenas Graniel, Sergio H. Sphaier, and R. Silva. Green water on a fixed structure due to incident bores: Guidelines and database for model validations regarding flow evolution. *Water (Switzerland)*, 11(12), 2019. ISSN 20734441. doi: 10.3390/w11122584.

[27] Leo H. Holthuijsen. *Waves in oceanic and coastal waters*, volume 9780521860. Cambridge University Press, 1 2007. ISBN 9780511618536. doi: 10.1017/CBO9780511618536. URL https://www.cambridge.org/core/books/waves-in-oceanic-and-coastal-waters/F6BF070B00266943B0ABAFEAE6F54465.

[28] Zheng Zheng Hu, Tri Mai, Deborah Greaves, and Alison Raby. Investigations of offshore breaking wave impacts on a large offshore structure. *Journal of Fluids and Structures*, 75:99–116, 2017. ISSN 10958622. doi: 10.1016/j.jfluidstructs.2017.08.005.

[29] J. Helder and P. van der Plas. Comflow user group. https://www.marin.nl/en/jips/networks/comflow-user-group, 2019.

[30] L ; Keuning and W Hillege. The results of the Delft Systematic Deadrise Series. *Proceedings of 14th International Conference on Fast Sea Transportation (FAST 2017)*, pages 97–106, 2017.

[31] Sungeun Kim and Hyun Ho Lee. Fully nonlinear seakeeping analysis based on CFD simulations. *Proceedings of the International Offshore and Polar Engineering Conference*, 8:970–974, 2011. ISSN 10986189.

[32] K. M.Theresa Kleefsman, Geert Fekken, Arthur E.P. Veldman, Tim H.J. Bunnik, Bas Buchner, and Bogdan Iwanowski. Prediction of green water and wave loading using a Navier-Stokes based simulation tool. In *Proceedings of the International Conference on Offshore Mechanics and Arctic Engineering - OMAE*, volume 1, pages 745–752, 2002. doi: 10.1115/OMAE2002-28480.

[33] K. M.Theresa Kleefsman, G. Erwin Loots, Arthur E.P. Veldman, Bas Buchner, Tim Bunnik, and Erik Falkenberg. The numerical simulation of green water loading including vessel motions and the incoming wave field. *Proceedings of the International Conference on Offshore Mechanics and Arctic Engineering - OMAE*, 3(August 2014):981–992, 2005. doi: 10.1115/OMAE2005-67448.

[34] T. Kleefsman. *Water Impact Loading on Offshore Structures*. 2005. ISBN 903672385X. URL http://irs.ub.rug.nl/ppn/288227360.

[35] Gang Nam Lee, Kwang Hyo Jung, Sime Malenica, Yun Suk Chung, Sung Bu Suh, Mun Sung Kim, and Yong Ho Choi. Experimental study on flow kinematics and pressure distribution of green water on a rectangular structure. *Ocean Engineering*, 195(May 2019):106649, 2020. ISSN 00298018. doi: 10.1016/j.oceaneng.2019.106649. URL https://doi.org/10.1016/j.oceaneng.2019.106649.

[36] Hyun Ho Lee, Ho Jeong Lim, and Shin Hyung Rhee. Experimental investigation of green water on deck for a CFD validation database. *Ocean Engineering*, 42:47–60, 2012. ISSN 00298018. doi: 10.1016/j.oceaneng.2011.12.026. URL http://dx.doi.org/10.1016/j.oceaneng.2011.12.026.

[37] Hui Li, Bao-Li Deng, Shu-Zheng Sun, Wen-Lei Du, and Hao-Dong Zhao. Experimental Investigation of the Green Water Loads on a Wave-Piercing Tumblehoeeme Ship. In *Proceedings of the ASME 2017 36th International Conference on Ocean, Offshore and Arctic Engineering*, pages 1–9, 2017. doi: 10.1115/omae2017-61338.

[38] W. D.M. Morris, J. Millar, and I. B. Buchner. Green water susceptibility of North Sea FPSO/FSUs. In *Journal of Offshore Technology*, volume 9, page 38, 2001.

[39] M.W. Dingemans. Water wave propagation over uneven bottoms, 1998. ISSN 0733950X.

[40] P. van der Plas. Comflow documentation. http://poseidon.housing.rug.nl/. Accessed: 2021.10.13.

[41] Csaba Pakozdi, Daniel Fonseca De Carvalho E Silva, Anders Östman, and Carl Trygve Stansberg. Green water on FPSO analyzed by a coupled potential-flow - NS-VOF method. In *Proceedings of the International Conference on Offshore Mechanics and Arctic Engineering - OMAE*, volume 8B, pages 1–10, 2014. ISBN 9780791845516. doi: 10.1115/OMAE2014-23913.

[42] Csaba Pákozdi, Anders Östeman, Carl T. Stansberg, Milovan Peric, Haidong Lu, and Rolf Baarholm. Estimation of wave in deck load using CFD validated against model test data. *Proceedings of the International Offshore and Polar Engineering Conference*, 2015-Janua(January):1046–1054, 2015. ISSN 15551792.

[43] X. P. Pham and K. S. Varyani. Evaluation of green water loads on high-speed containership using CFD. *Ocean Engineering*, 32(5-6):571–585, 2005. ISSN 00298018. doi: 10.1016/j.oceaneng.2004.10.009.

[44] Edward Ransley, Shiqiang Yan, Scottandrew Brown, Tri Mai, David Graham, Qingwei Ma, Pierre Henri Musiedlak, Allanpeter Engsig-Karup, Claes Eskilsson, Qian Li, Jinghua Wang, Zhihua Xie, Sriram Venkatachalam, Thorsten Stoesser, Yuan Zhuang, Qi Li, Decheng Wan, Gang Chen, Hao Chen, Ling Qian, Zhihua Ma, Clive Mingham, Derek Causon, Inno Gatin, Hrvoje Jasak, Vuko Vukcevit'C, Steven Downie, Pablo Higuera, Eugeny Buldakov, Dimitris Stagonas, Qiang Chen, Jun Zang, and Deborah Greaves. A blind comparative study of focused wave interactions with a fixed FPSO-like structure (CCP-WSI blind test series 1). *International Journal of Offshore and Polar Engineering*, 29(2):113–127, 2019. ISSN 10535381. doi: 10.17736/ijope.2019.jc748.

[45] Edward J. Ransley, Scott A. Brown, Martyn Hann, Deborah M. Greaves, Christian Windt, John Ringwood, Josh Davidson, Pal Schmitt, Shiqiang Yan, Junxian X. Wang, Jinghua H. Wang, Qingwei Ma, Zhihua Xie, Giuseppe Giorgi, Jack Hughes, Alison Williams, Ian Masters, Zaibin Lin, Hao Chen, Ling Qian, Zhihua Ma, Qiang Chen, Haoyu DIng, Jun Zang, Jennifer Van Rij, Yi Hsiang Yu, Zhaobin Li, Benjamin Bouscasse, Guillaume Ducrozet, and Harry Bingham. Focused wave interactions with floating structures: A blind

comparative study. *Proceedings of the Institution of Civil Engineers: Engineering and Computational Mechanics*, 174(1):46–61, 2021. ISSN 17550785. doi: 10.1680/jencm.20.00006.

[46] K. Ravindra Babu, R. Datta, and A. Bhattacharyya. Numerical Investigation of Heave and Pitch Motion Effects on Green Water Loading for a Floating Body. *Journal of Marine Science and Application*, 18(4): 457–471, 2019. ISSN 19935048. doi: 10.1007/s11804-019-00118-1.

[47] Yonguk Ryu, Kuang An Chang, and Richard Mercier. Runup and green water velocities due to breaking wave impinging and overtopping. *Experiments in Fluids*, 43(4):555–567, 2007. ISSN 07234864. doi: 10.1007/s00348-007-0332-0.

[48] J. Sanchez-Mondragon, J. V. Hernández-Fontes, A. O. Vázquez-Hernández, and P. T.T. Esperança. Wet dam-break simulation using the SPS-LES turbulent contribution on the WCMPS method to evaluate green water events. *Computational Particle Mechanics*, 7(4):705–724, 2020. ISSN 21964386. doi: 10.1007/s40571-019-00302-8. URL https://doi.org/10.1007/s40571-019-00302-8.

[49] V. Sriram, T. Schlurmann, and S. Schimmels. Focused wave evolution using linear and second order wavemaker theory. *Applied Ocean Research*, 53:279–296, 2015. ISSN 01411187. doi: 10.1016/j.apor.2015.09.007. URL http://dx.doi.org/10.1016/j.apor.2015.09.007.

[50] Peter S. Tromans, A. H.R. Anatruk, and Paul Hagemeijer. New model for the kinematics of large ocean waves application as a design wave. *Proceedings of the First International Offshore and Polar Engineering Conference*, (February):64–71, 1991.

[51] TU Delft, 3mE, MTT. Towing tank no. 2. https://www.tudelft.nl/3me/over/afdelingen/maritime-and-transport-technology/research/ship-hydromechanics/facilities/towing-tank-no-2. Accessed: 2021.10.11.

[52] Xizeng Zhao, Zhouteng Ye, and Yingnan Fu. Green water loading on a floating structure with degree of freedom effects. *Journal of Marine Science and Technology (Japan)*, 19(3):302–313, 2014. ISSN 09484280. doi: 10.1007/s00773-013-0249-7.